



8-2015

# NANOSCALED CELLULOSE AND ITS CARBONACEOUS MATERIAL: APPLICATION AND LOCAL STRUCTURE INVESTIGATION

Yujie Meng

*University of Tennessee - Knoxville, ymeng2@vols.utk.edu*

---

## Recommended Citation

Meng, Yujie, "NANOSCALED CELLULOSE AND ITS CARBONACEOUS MATERIAL: APPLICATION AND LOCAL STRUCTURE INVESTIGATION." PhD diss., University of Tennessee, 2015.  
[https://trace.tennessee.edu/utk\\_graddiss/3449](https://trace.tennessee.edu/utk_graddiss/3449)

This Dissertation is brought to you for free and open access by the Graduate School at Trace: Tennessee Research and Creative Exchange. It has been accepted for inclusion in Doctoral Dissertations by an authorized administrator of Trace: Tennessee Research and Creative Exchange. For more information, please contact [trace@utk.edu](mailto:trace@utk.edu).

To the Graduate Council:

I am submitting herewith a dissertation written by Yujie Meng entitled "NANOSCALED CELLULOSE AND ITS CARBONACEOUS MATERIAL: APPLICATION AND LOCAL STRUCTURE INVESTIGATION." I have examined the final electronic copy of this dissertation for form and content and recommend that it be accepted in partial fulfillment of the requirements for the degree of Doctor of Philosophy, with a major in Natural Resources.

Siqun Wang, Timothy M. Young, Major Professor

We have read this dissertation and recommend its acceptance:

Frank M. Guess, Seung-Hwan Lee

Accepted for the Council:

Dixie L. Thompson

Vice Provost and Dean of the Graduate School

(Original signatures are on file with official student records.)

---

**NANOSCALED CELLULOSE AND ITS CARBONACEOUS  
MATERIAL: APPLICATION AND LOCAL STRUCTURE  
INVESTIGATION**

**A Dissertation Presented for the  
Doctor of Philosophy  
Degree  
The University of Tennessee, Knoxville**

**Yujie Meng  
August 2015**

Copyright © 2015 by Yujie Meng  
All rights reserved.

# **DEDICATION**

*To My Parents*

*Jianping Meng and Jingping Guo*

## ACKNOWLEDGEMENTS

I would like to express my deeply gratitude to my co-advisor, Dr. Siqun Wang, who shaped me into what I am today, by his guidance and advice throughout my PhD study. Special thank goes to my other co-advisor, Dr. Timothy M. Young who is encouraging and supportive to me, as always. I would also like to thank my committee members, Dr. Frank M. Guess and Dr. Seung-Hwan Lee for their time and valuable advise for this work.

This research is financial supported by the UTIA 2013/2014 Innovation Grant, the U.S.305 Forest Service Southern Research Station under contract agreement 07-CR-11330115-087, Southeastern 306 Sun Grant Center, USDA Special Wood Utilization Grants R11-0515-041 and R11-2219-510, the University of Tennessee, Department of Forestry, Wildlife and Fisheries and the Agricultural Experiment Station McIntire-Stennis Grant TENOOMS-101.

Many scientists and researchers offered their generous help throughout the pursuing of my PhD. I am grateful to Dr. Cristian I. Contescu, who provides valuable suggestions on my research papers. I also thank all other co-authors on my journal papers for their informative suggestions, involvements and efforts. I thank all my colleagues in Center for Renewable Carbon, by whom I am fortunate to be encouraged and helped. I had a good time working with them. I thank Dr. Caijun Su for his encouragement, support and taking care of me. I appreciate the friendship and inspiration all my trustworthy best friends give to me to make my PhD life easier and joyful.

I am blessed by my wonderful parents, all other family members for their endless love, support and believe. They have all my love, respect and admiration and I hope I make them proud.

## ABSTRACT

In this dissertation, cellulose nanocrystals three-dimensional morphology, size distribution, and the crystal structure were statistically and quantitatively investigated. Lognormal distribution was identified as the most likely for cellulose nanocrystals' size distribution. Height and width dimensions were shown to decrease toward the ends from the midpoint of individual CNCs, implying a spindle-like shape. XRD analysis of crystallite size accompanied with TEM and AFM measurements revealed that the cross-sectional dimensions of individual switchgrass CNC were either rectangular or elliptical shape, with an approximately 3~5 nm [nanometer] lateral element length range. A sponge-like carbon aerogel from microfibril cellulose with high porosity, ultra-low density, hydrophobic properties, and reusability was synthesized. Carbon aerogels heat-treated at 700 and 900 °C [Celsius] were examined and compared. Sample C-700 (521 m<sup>2</sup> /g [square meter/gram]) exhibits significantly higher BET surface area than Sample C-950 (149 m<sup>2</sup> /g [square meter/gram]). It also achieved highest normalized sorption capacity (86 g/g [gram/gram]) for paraffin oil. The removal of hydrophilic function groups of carbon aerogel proved by FTIR results to its highly hydrophobic properties. The Oil absorption ability is favored by its highly porous 3D network structure with interconnected cellulose nanofibrils. Simultaneous effects of processing parameters (peak temperature, heating rate) for carbon aerogel processing were investigated using response surface methodology (RSM). Results indicated that the optimum conditions were: 300 °C [Celsius] of the peak temperature and 8.0 °C/min [Celsius/minute] of the heating rate with approximately 90.1 g/g [gram/gram] of the normalized oil absorption capacity. An electron microscopy investigation was performed to link the micro-structure and properties of carbonized cellulose and lignin with the structure of original biomass components. Structure details at micro and molecular levels have been investigated by scanning transmission electron microscopy (STEM). Atomic resolution images revealed the presence of random, fractured graphene fragments in carbonized cellulose (C-CNC) and of large domains of parallel stacked graphene in carbonized lignin (C-Lignin). The randomly arranged small graphene fragments in C-CNC create a network of interconnected micropores and mesopores and contribute to the increased BET surface area. Formation of parallel stacks of graphene structures is favored by the pre-existence of aromatic components in lignin.

# TABLE OF CONTENT

INTRODUCTION .....	1
CHAPTER I ANALYZING THREE-DIMENSIONAL STRUCTURE AND GEOMETRICAL SHAPE OF INDIVIDUAL CELLULOSE NANOCRYSTAL FROM SWITCHGRASS.....	5
Abstract.....	7
1. Introduction.....	8
2. Materials and methods .....	10
2.1 Materials and chemicals .....	10
2.2 Pretreatment of switchgrass.....	11
2.3 Sulfuric acid hydrolysis.....	11
2.4 Characterization.....	12
2.4.1 Fourier transform infrared spectroscopy (FTIR).....	12
2.4.2 Transmission electron microscopy (TEM).....	12
2.4.3 Wide angle X-ray diffraction (WXR)D .....	12
2.4.4 Atomic force microscope measurement (AFM).....	13
3. Results and discussion .....	14
3.1 Isolation of cellulose from switchgrass.....	14
3.2 Morphology of switchgrass CNC .....	15
3.2.1 Length, width, height, and roughness measurement .....	15
3.3 Size distribution.....	16
3.3.1 Data imputation.....	16
3.3.2 Information criterion and distribution selection.....	17
3.4 Estimation of surface morphology and crystallite structure of CNC .....	18
4. Conclusions.....	19
Appendix I .....	21



CHAPTER II ULTRALIGHT CARBON AEROGEL FROM NANOCELLULOSE AS A HIGHLY SELECTIVE OIL ABSORPTION MATERIAL .....	31
Abstract.....	34
1. Introduction.....	35
2. Materials and experimental section .....	36
2.1 Materials .....	36
2.2 Preparation of MFC aerogel and carbon aerogel .....	36
2.3 Characterization of MFC aerogel and carbon aerogel .....	37
2.4 Oil sorption experiments.....	38
3. Results and discussion .....	39
3.1 Thermal decomposition kinetics .....	39
3.2 Structure of MFC aerogel and carbon aerogel.....	40
3.3 Surface area and porosity of carbon aerogels .....	41
3.4 Hydrophobic properties of carbon aerogel surface.....	43
3.5 Oil absorption.....	43
4. Conclusions.....	45
Appendix II.....	47
CHAPTER III OPTIMIZATION OF CELLULOSE NANOFIBRILS CARBON AEROGEL FABRICATION USING RESPONSE SURFACE METHODOLOGY .....	59
Abstract.....	61
1. Introduction.....	62
2. Material and methods.....	63
2.1 Material.....	63
2.2 Preparation of NFC aerogel and carbon aerogel.....	64
2.3 Oil sorption experiments.....	64
2.4 Characterization of NFC aerogel and carbon aerogel.....	64
2.5 Experimental design.....	65

2.6 Statistical analysis.....	65
3. Results and discussion .....	66
3.1 Observation of structure and physical properties.....	66
3.2 Factor optimization by response surface methodology .....	67
3.3 The statistical analysis results of the optimization experimentation for two variables .....	67
3.4 Optimization of normalized oil absorption capacity and weight reduction of carbon aerogel .....	69
3.5 Thermal stability analysis .....	71
4. Conclusion .....	72
Appendix III.....	73
CHAPTER IV LOCAL STRUCTURE INVESTIGATION OF DISORDERED CARBONS FROM CELLULOSE AND LIGNIN BY SCANNING TRANSMISSION ELECTRON MICROSCOPE (STEM).....	
	84
Abstract: .....	87
1. Introduction:.....	88
2. Experimental procedure .....	90
2.1 Materials .....	90
2.2 Preparation of cellulose nanocrystal and lignin .....	90
2.3 Carbonization of cellulose nanocrystal and lignin.....	91
2.4 Nitrogen adsorption .....	91
2.5 Electron microscopy .....	91
2.6 Thermal gravimetric analysis.....	92
2.7 Wide-angle X-ray diffraction.....	92
2.8 Fourier transform infrared spectroscopy (FTIR) .....	93
3. Results and discussion .....	93
3.1 Porosity information from nitrogen gas adsorption .....	93
3.2 Observation of cellulose nanocrystal and lattice structure .....	94
3.3 Observation of graphene in carbonized cellulose nanocrystal and carbonized lignin .....	94

3.3 Thermogravimetric analysis.....	96
3.4 X-ray Diffraction (XRD) analysis .....	97
4. Discussion.....	97
5. Conclusion: .....	98
Appendix IV.....	100
CONCLUSION.....	113
FUTURE WORK.....	115
REFERENCE.....	116
VITA.....	126

## LIST OF TABLES

Table I- 1 Crystallinity index (CrI) and crystallite size of raw switchgrass, dewaxed switchgrass, delignified switchgrass, switchgrass cellulose, and cellulose nanocrystals (CNCs), estimated by Scherrer's expression .....	28
Table I- 2 Summary of geometrical shapes of cellulose nanocrystals from different sources .....	29
Table II- 1 Onset temperature, degradation temperature and weight loss of MFC aerogel under different heating rates .....	56
Table II- 2 Carbon aerogel's properties and fitting parameters of the sorption kinetics .....	57
Table II- 3 Elemental percentage of MFC aerogel as an average of 2 runs before and after carbonization.....	58
Table III- 1 Independent variables and their values for oil absorption capacity .....	80
Table III- 2 Second-order central composite on face design, experimental data for three-level-two factors response surface analysis .....	81
Table III- 3 Analysis of Variance (ANOVA) for response surface quadratic model .....	82
Table III- 4 Estimated regression coefficients for normalized oil absorption capacity and weight reduction .....	83
Table IV- 1 Pore surface area and pore volumes of as-prepared C-CNC and C-Lignin .....	111
Table IV- 2 Onset temperature, degradation temperature, maximum weight-loss rates and weight loss of CNC and lignin.....	112

## LIST OF FIGURES

Figure I- 1 FTIR spectrum of switchgrass powder, de-waxed powder, delignified powder, hemicellulose extracted powder, and cellulose nanocrystals.....	22
Figure I- 2 (a) X-ray diffraction patterns of a) switchgrass, b) de-waxed switchgrass, c) delignified switchgrass, d) switchgrass cellulose, e) cellulose nanocrystals .....	23
Figure I- 3 Atomic force microscopic image and line profile of individual switchgrass CNC fiber. (a) CNC topography image; (b) CNC line profiles; (c) Transmission electron micrographs of switchgrass CNCs; (d) Intensity profile scanned across individual CNC on two locations .....	24
Figure I- 4 Length, roughness, height and width distribution histograms of switchgrass CNCs, where height and length were measured from the AFM image and width was measured from the TEM image. The continuous curves correspond to fitting of the data using a log-normal function. ....	25
Figure I- 5 Plots of switchgrass CNC samples' (a) height and (b) width along their longitudinal axis (A) Left end (B) Quarter position (C) Middle point (D) Three-quarter position (E) Right end.....	26
Figure I- 6 Schematic representation of individual switchgrass CNCs. (a) Cellulose microfibrils (b) removal of disordered/amorphous region during acid hydrolysis(c) individual CNC (d) Cross-section of CNCs; (e) cellulose chain repeat unit. ....	27
Figure II- 1 Thermogravimetric analysis (TGA) curves showing the effect of heating rate during the temperature rising from 230°C to 320 °C on carbon residual yield at 800°C (a) TGA curves, (b) DTG curves.....	48
Figure II- 2 Photographs of (a) microfibril cellulose aerogel, and (b) carbon aerogel (C-950); SEM images of (c) microfibril cellulose aerogel, and (d) carbon aerogel (C-950); TEM images of (e) graphitic domains in the structure of carbon aerogel C-950 and (f) diffraction pattern from the same carbon aerogel.....	49
Figure II- 3 The formation of ester bond between Kymene <sup>TM</sup> crosslinker and cellulose carboxyl groups.....	50
Figure II- 4 FTIR spectra of MFC aerogel and carbon aerogels.....	51

Figure II- 5 (a) Adsorption isotherms of nitrogen on carbon aerogel heat-treated at 700°C and 950°C; (b) cumulative surface distribution of carbon aerogels and (c), (d) differential and cumulative pore size distributions determined by NLDFT method for Samples C-700 (c) C-950 (d).....	52
Figure II- 6 Carbon aerogel wetting characterization by static contact angle analysis. ....	53
Figure II- 7 (a), (b) and (c) Removal of engine oil from the water surface using nanocellulose carbon aerogel (d) Ultralight carbon aerogel sitting on a flower.....	54
Figure II- 8 Sorption kinetics of different oils absorbed by carbonized MFC aerogel: (a) canola oil, (b) pump oil, (c) diesel oil, (d) paraffin oil, (e) normalized saturated sorption capacities of different oils by oil density, (f) absorption reusability of carbon aerogel. ....	55
Figure III- 1 Graphic representation of two-factor face-centered central composite designs .....	74
Figure III- 2 SEM images of (a) NFC aerogel, (b) carbon aerogel heat treated at 1000 °C, (c) TEM images of graphite domain in the structure of carbon aerogel heat treated at 1000°C, (d) line profile of graphite domain from the same sample, (e) NFC aerogel sitting on the flower and (f) carbon aerogel holding a water droplet on the surface .....	75
Figure III- 3 (a) Goodness-of fit between predicted values obtained via partial least squares fitting and experimentally measured oil absorption capacity values and (b) between predicted values obtained and experimentally measured weight reduction.....	76
Figure III- 4 (a) response surface plot and (b) contour profile representing the interaction between the variables affecting the normalized oil absorption capacity by oil density; (c) response surface plot and (d) contour profile representing the interaction between the variables affecting carbon yield after carbonization. ....	77
Figure III- 5 (a) Prediction profiler shows optimization prediction plots and (b) overlaid contour plot for normalized oil absorption capacity (g/g) and weight reduction (%).....	78
Figure III- 6 Thermogravimetric analysis (TGA) showing the effect of heating rate during temperature rising from 230 to 320 °C on carbon residual yield at 1000 °C (a) TGA curve and (b) DTG curve .....	79

Figure IV- 1 Adsorption-desorption isotherms of nitrogen on (a) C-CNC and (b) C-Lignin: blue and red lines are adsorption and desorption data, respectively. Pore size distributions determined by QSDFT method for (c) C-CNC and (d) C-Lignin. ....	101
Figure IV- 2 HRTEM image of individual CNCs (a) and annular dark-field (ADF) image of its lattice structure (b). The inset in the right upper corner is a Fast Fourier Transform (FFT) pattern. ....	102
Figure IV- 3 Annular dark-field (ADF) image of CNCs before (a) and after (b) beam irradiation. The inset in the right upper corner is a Fast Fourier Transform (FFT) pattern .....	103
Figure IV- 4 Micrographs of CNC carbon and lignin carbon following heat treatment at 950°C: Bright field STEM images of (a) C-CNC, (b) C-Lignin,(c) and (d) C-Lignin under low magnification, The Inset in the right upper corner of (d) is the diffraction pattern. ....	104
Figure IV- 5 ADF images obtained from thin edge area of carbonized cellulose nanocrystals (a) low magnification (b) high magnification. ....	105
Figure IV- 6 Typical TG-DTG curves in N <sub>2</sub> for cellulose nanocrystals and lignin (a) Percentage weight loss as a function of temperature and (b) Weight loss rate as a function of temperature. ....	106
Figure IV- 7 FTIR spectra of (a) cellulose nanocrystals and C-CNC (b), Lignin and C-lignin.	107
Figure IV- 8 Wide-angle X-ray diffraction curves of CNC, C-CNC, Lignin and C-Lignin. ....	108
Figure IV- 9 Schematic of lignin structure (adopted from Ball(Ball, 1992) ) evolution during carbonization.....	109
Figure IV- 10 Scheme of cellulose structure and cellulose carbonization (adopt from Losty (Davidson and Losty, 1963)). ....	110

## INTRODUCTION

This dissertation consists of four journal articles: 1) “Analyzing three-dimensional structure and geometrical shape of individual cellulose nanocrystal from switchgrass (*Panicumvirgatum L*)”; 2) “Ultralight carbon aerogel from nanocellulose as a highly selective oil absorption material”; 3) “Optimization of cellulose nanofibrils carbon aerogel fabrication using response surface methodology (RSM)”; 4) “Local structure investigation of disordered carbons from cellulose and lignin by scanning transmission electron microscope (STEM)”. The first article was submitted to the *Polymer Composites* on June 27<sup>th</sup>, 2015; the second article was published in *Cellulose* in 2014 (Meng et al., 2014); the third article was submitted to the *European Polymer Journal* on June 17<sup>th</sup>, 2015 ; and the fourth article was submitted to *Biomacromolecules* on July 06<sup>th</sup> ,2015. Each paper is listed as an individual chapter within the dissertation.

As a nanomaterial extracted from natural polymers, cellulose nanocrystals not only take the advantage of biocompatible, environmentally friendly, renewable nature and variant resources, but also possess high specific strength and high modulus. Basically, there are two categories of nanosized cellulosic particles separated by processing methods in spite of their variant terminologies (Siqueira et al., 2010). Cellulose nanocrystals are mainly isolated by acid hydrolysis method while microfibril cellulose is extracted through mechanical treatments, such as grinding, high-pressure homogenization and ball milling (Kelsey and Shafizadeh, 1980). Among various factors that influence the nanocomposite mechanics, the intrinsic properties of cellulose nanocrystals, including dimensions, crystallinity, morphology, surface roughness, and their interfacial interactions with the polymer matrix, are of great important (Siqueira et al., 2009). In general, cellulosic nanocrystal morphology can be described by their length (100-500 nm), diameter (5-20 nm), and aspect ratio (10-70) (Siqueira et al., 2009, Han et al., 2012, Bondeson et al., 2006). The structure of cellulose can be described as an aggregate of linear chain of  $\beta$  (1,4) glucose molecules, which are parallel stacked by van der Waals and hydrogen bonds (Moon et al., 2011). In spite of the fact that importance of nanoparticles size and morphology has been noticed by modeling simulation, experimentally, the description of the



individual nanoparticle is of less accurate. To the author's best knowledge, none of these studies mention width and thickness evolution in CNCs' longitudinal direction in order to gain deep understanding of particle morphology (Mariano et al., 2014, Moon et al., 2011, Habibi et al., 2010, Elazzouzi-Hafraoui et al., 2008).

New applications of nanoscale cellulose are attracting attention. Porous carbon materials derived from woody-biomass have long been used for gas, oil absorption, and separation. As an example of this, oil recovery using absorbent materials is superior to many other industrial methods for oil recovery, such as physical collection, biodegradation, or *in-situ* burning, because of the lower costs, higher efficiency and higher recyclability of most absorbents (Hubbe et al., 2013). Although conventional absorbent materials have been widely used for large-scale oil spill cleanup, their absorption efficiency is greatly impaired by the high water affinity of most natural materials (Peng et al., 2013). In contrast, absorbents from natural precursors with both hydrophobic and oleophilic properties have the potential of being both practically and commercially important. In this dissertation research, I have successfully developed a super-light, hydrophobic carbon aerogel with highly oil absorption properties using microfibril cellulose as the raw material (Meng et al., 2014). I demonstrated a green synthesis approach involves freeze-drying and carbonization process to achieve 3D porous network structure and hydrophobic properties. I also noticed that low heating temperature helped improving the oil absorption capacity. On top of that, in order to achieve maximum oil absorption capacity and increase the final carbon yield, research attention focused on two factors during carbonization: 'peak temperature' and 'heating rate'.

There are some disadvantages of studying the influence of the factor on the response one-factor at a time, e.g., it is time consuming involving many experiments and does not allow for the examination of interaction effects. Design of experiments (DOE) is a tool that allows for parameter optimization, especially in cases where many factors are involved and varied simultaneously. Response surface methodology (RSM) is an effective statistical tool used in studies including biochemical systems, biotechnology, and nanotechnology etc. (Montgomery, 2012). RSM allows for expanded inference; the study of interactions; and parameter optimization.

Basically, RSM is a formal statistical technique that maximizes inference with the minimum number of experimental runs.

Since biomass carries the most abundant natural aromatic polymer in the world, carbon materials from which has attracted extensively interest due to its abundant, renewable, sustainable, biocompatible and biodegradable future (Langan et al., 2014). With the development of the carbon structures from this potential green alternative, numerous promising applications have been exploited, high-value added products ranging from energy, hydrogen storage, catalyst support, drug delivery to super capacitors etc. (Meng et al., 2014, He et al., 2014b, Dobeles et al., 2012, Wang et al., 2013, Zhao et al., 2012). In essence, the formation of these carbonaceous materials all requires the involvement of a complex pyrolysis treatment (oxides reaction). To the best of our knowledge, the discussion regarding to the linkage between precursor structure and its corresponding carbon structure is limited. In fact, there exists certain linkage between the carbon precursor chemistry and the final morphology of carbon material. Attempts have been made to study and compare the oxidative behavior/carbonization kinetics between cellulose and lignin only through spectroscopic analysis. They argued that lignin and cellulose exhibit differential ablation temperature and the ratio of carbon to oxygen drastically influences the resulting carbon microstructure (Cao et al., 2013, Xie et al., 2009, Ishimaru et al., 2007). Nevertheless, understanding the structure property relationship of biomass carbonaceous materials at very local length scales remains a significant research challenge.

The research goal of this dissertation was to investigate the nanocellulose materials in terms of fundamental structure analysis, new applications and the local structure analysis of its carbonaceous material. I performed morphology (particle size distribution) and crystal structure analysis of individual nanocrystals through surface analysis and microscopy technique. Attempts were also made to link nanocellulose to an application. The nanocellulose-based ultralight carbon aerogel for novel oil spill cleanup materials was synthesized. The physical properties, internal morphology, thermal properties, and chemical properties were also examined. Furthermore, the carbon aerogel making process was successfully optimized by adopting a statistical strategy of response surface methodology, in this case, faced centered central composite design (CCF). I demonstrated that there exist the linkage between carbonization

operating process variables (peak temperature and heating temperature) and the carbon aerogel performance (normalized oil absorption capacity, weight reduction). Compared to conventional single factor optimization methods, which are time consuming and expensive with vague and misleading information, Design of Experiment (DOE) methodology performed in this research and the resulting statistical model provided integrated and accurate results to systematically and effectively predict the response through various independent variables. Last, investigation of carbonization behavior of cellulose and lignin was also reported. The influence of biomass component on the structure and properties of its resulting carbonaceous was studied. Structure changes at micro and molecular levels have been investigated by atomic-resolution TEM images and image processing techniques. I proved that carbon cellulose contains randomly orientated small pieces of fringe fragments and carbon lignin exhibit well-ordered stacking graphene sheets.

**CHAPTER I**  
**ANALYZING THREE-DIMENSIONAL STRUCTURE AND**  
**GEOMETRICAL SHAPE OF INDIVIDUAL CELLULOSE**  
**NANOCRYSTAL FROM SWITCHGRASS**

A version of this chapter was submitted to the *Polymer Composites* on June 27th, 2015.

Authors:

Y. Meng, T.M. Young, S. Wang

*Department of Forestry, Wildlife and Fisheries, Center for Renewable Carbon, University of Tennessee, Knoxville, TN, USA*

Q. Wu, Y. Li

*College of Engineering, Zhejiang Agricultural and Forestry University, Hangzhou, 311300, China*

B. Huang.

*College of Engineering, Fujian Agricultural and Forestry University, Fuzhou, China*

Y. Meng's primary contribution to this paper includes identifying the research objective, design and conduct of the experiments, process and interpretation of the data, drafting the paper.

Co-researchers' contributions are listed as follows:

Q. Wu produced cellulose nanocrystals and worked with Yujie to analysis the data.

T. M. Young revised and language polished the paper.

B. Huang worked with Yujie Meng to analyze the experimental data.

S. Wang identified the research objective, provided research guideline, revised the paper and worked with Yujie to analysis the data.

Y. Li provided research guideline.

## **Abstract**

The three-dimensional morphology, size distribution and structure of individual cellulose nanocrystals (CNCs) isolated from switchgrass (*Panicumvirgatum L*), a representative raw biomass material, were investigated in this research. Width and thickness evolutions along the individual CNC longitudinal direction were statistically and quantitatively characterized using transmission electron microscopy (TEM) and atomic force microscopy (AFM). Lognormal distribution was identified as the most likely for cellulose nanocrystals' size distribution. Height and width dimensions were shown to decrease toward the ends from the midpoint of individual CNCs, implying a spindle shape. The observed rough surfaces of CNCs were explainable as the results of acid etching of the subcrystalline and disordered region located at the surface. X-ray diffraction analysis of crystallite size accompanied with TEM and AFM measurements revealed that the cross-sectional dimensions of individual switchgrass CNC were either rectangularly or elliptically shaped, with an approximately 3~5 nm lateral element length range.

## 1. Introduction

The advent of nanotechnology has launched a revolution in the forest-products industry, providing opportunities to generate new, sustainable, renewable, and recyclable materials at nanoscale. Cellulose nanocrystals has recently attracted extensive research interest, owing to its various superior properties such as high mechanical strength, rheological, optical and thermal properties. Switchgrass is a perennial grass native to North America and has been identified as one of major energy crops in US. As one potential source for cellulose among many biomass crops in the world, switchgrass cellulose fibers has been recognized as a potential reinforcing and filling component of polymer composite due to the pronounced mechanical performance of switchgrass fibers produced in a sustainable way (Van den Oever et al., 2003). These advances have spurred tremendous interest in developing various high-performance nanocomposites where hydrophobic polymers are reinforced by CNCs (Eichhorn et al., 2010, Visakh et al., 2012, Rafieian and Simonsen, 2014, Uddin et al., 2011).

Among various factors that influence the nanocomposite mechanics, the intrinsic properties of cellulose nanocrystals, including dimensions, crystallinity, morphology, surface roughness, and their interfacial interactions with the polymer matrix, are of great important (Siqueira et al., 2009). In particular, well-dispersed nanometer-sized CNCs filler in nanocomposite contributes to large surface area and can create large amount of interfacial region, favoring the reinforcement (Moon et al., 2011). In addition, the physical properties of the constituent nanoparticles will greatly influence its flow and mix behavior during the melting process. Hassanabadi et al claimed that higher anisometry and smaller size would dramatically increase the polymer-particle and particle-particle interactions (Hassanabadi and Rodrigue, 2014). Our previous research revealed that the mechanical properties of switchgrass CNC thin films exceed those of cotton CNC thin films due to the higher aspect ratio (Wu et al., 2013b).

Recently, effects of nanoparticle size and morphology on the self-organization properties, dispersion quality, rheological and mechanical properties of nanocomposite have been extensively studied by means of theoretical simulations in a nanoscale context (Khoshkava and Kamal, 2014, Peng et al., 2012, Wu et al., 2014, Jonoobi et al., 2014, Mishnaevsky Jr, 2012, Wang et al., 2011, Liu and Brinson, 2008). Knauert et al recognized that rod-like nanoparticles

exhibited the largest increase in the viscosity of nanocomposite compared to tube and sheet-like particles did (Knauert et al., 2007). Li et al argued in their research that nanocomposite with graphene filler has the largest interaction energy and polymer chain packing than other nanoparticles due to the large surface-area-to-volume ratio (Li et al., 2012). Nanoparticle aspect ratio has been proved to have a positive effect on the longitudinal Young's modulus of unidirectional aligned composites (Tandon and Weng, 1984). In brief, information about cellulose nanocrystal morphology is especially important for designing fibril-reinforced nanocomposites (Moigne et al., 2011).

Despite varying descriptions of cellulose nanocrystals, such as “rod-like” (Herrera et al., 2012), or “ribbon-like” or “needle-shaped” (Brito et al., 2012), they have usually been considered to be cylindrical (Favier et al., 1997) with uniform geometry and isotropic properties in model predictions. Clearly, this idealized approximation leads to a discrepancy between model predictions and experimental results, causing numerous issues Liu and Brinson (2008) such as inappropriate extrapolation and unexplainable phenomena relating to material performance. These problems have spurred intensive efforts to precisely determine the geometrical features of reinforcing particles.

Aqueous suspension of cellulose nanocrystals can be derived by sulfuric acid hydrolysis from various natural resources (Teixeira et al., 2010, Rosa et al., 2010, Lu and Hsieh, 2012, Kargarzadeh et al., 2012, Cherian et al., 2008, Lu et al., 2014, Brito et al., 2012). In general, cellulosic nanocrystal morphology can be described by their length (100-500 nm), diameter (5-20 nm), and aspect ratio (10-70) (Siqueira et al., 2009, Han et al., 2012, Bondeson et al., 2006). The structure of cellulose can be described as an aggregate of linear chain of  $\beta$  (1,4) glucose molecules, which are parallel stacked by van der Waals and hydrogen bonds (Moon et al., 2011). In essence, the formation of CNCs is attributed to harsh acid reaction and sonication treatment, which are able to overcome the lateral adhesion among elementary crystallites in cellulose. The measurement and characterization of nanocellulose involves particle size, distribution, shape, degree of branching, specific surface area, agglomeration etc. Currently available methods include light microscopy, SEM, TEM, and AFM, resulting in various conclusions because of the intrinsically different limitations of the measuring method (Kvien et al., 2005); an example is the “fat tip” effect on width measurement conducted by AFM (Allen et al., 1992). In spite of the



fact that importance of nanoparticles size and morphology has been noticed by modeling simulation, experimentally, the description of the individual nanoparticle is of less accurate. To the author's best knowledge, none of these studies mention width and thickness evolution in CNCs' longitudinal direction in order to gain deep understanding of particle morphology (Mariano et al., 2014, Moon et al., 2011, Habibi et al., 2010, Elazzouzi-Hafraoui et al., 2008).

Different from previous studies, the major purpose of the present research is to prepare cellulose nanocrystals from switchgrass cellulose via the acid hydrolysis method, to investigate their geometrical shape, to characterize their structure, and to quantitatively describe the morphology of the nanocrystals. Instead of providing generalized height and width distributions of cellulose nanocrystals, we focus on five locations along the longitudinal axis of the crystal. This research may provide guidance in precisely characterizing morphology of cellulose nanocrystals as well as offering a basis for further study in the simulation, prediction, and optimal design of nanocomposites with the goal to achieve high-performance.

## **2. Materials and methods**

### **2.1 Materials and chemicals**

Switchgrass was selected as a representative material for this research because its low lignin content makes it a promising raw material for the production of cellulose nanocrystals (Wiselogel et al., 1996). Alamo switchgrass (*Panicumvirgatum L*) was obtained from an East Tennessee 2011 harvest. Toluene ( $C_6H_5CH_3$ , Fisher Scientific), ethanol ( $CH_3CH_2OH$ , 95%, Acros Organics), sodium chlorite ( $NaClO_2$ , 80%, Ricca Chemical Company), acetic acid glacial ( $CH_3COOH$ , 80%, Reagent, Fischer Scientific) and potassium hydroxide (KOH, 90%, Sigma Aldrich) were used to separate cellulose from switchgrass. Sulfuric acid ( $H_2SO_4$ , 95%-98%, A.C.S reagent, Sigma Aldrich) was used for the hydrolysis and distilled water was used throughout the research.

## 2.2 Pretreatment of switchgrass

The pretreatment for isolating cellulose from switchgrass was similar to procedures that have been described for varying resource materials (Lu and Hsieh, 2012). Switchgrass was prewashed using tap water to remove dirt and water-soluble substances. The air-dried switchgrass was chopped up in a Wiley mill (Thomas Wiley® Mini-Mill, Thomas Scientific) and sieved through a 40-mesh sieve. The resulting switchgrass powder (100 g) was first de-waxed with 2:1, v/v toluene/ethanol (1500 ml) mixture for 24 h, and washed with distilled water. The powder was oven-dried at 50 °C for 24 h after suction filtration. Delignification was conducted by immersing the powder in 1.4% acidified NaClO<sub>2</sub> (1500 ml), with pH adjusted to 3.0-4.0 by CH<sub>3</sub>COOH. The mixture was stirred at 800 rpm in a water bath at 70 °C for 24 h to dissolve the lignin and then cooled in an ice bath to quench the reaction, followed by suction filtration with cold distilled water until the filtrate became neutral. Hemicellulose was extracted by adding delignified powder into 2000 ml 5% KOH and stirring at 90 °C for 2 h. These procedures were repeated at least twice to ensure a thorough removal of unwanted material. The resulting white cellulose powder was washed until it reached a neutral pH, and it was then oven-dried and milled to pass through a 40-mesh screen and stored under vacuum for the following processes.

## 2.3 Sulfuric acid hydrolysis

Cellulose separated from switchgrass was hydrolyzed using 60 wt% sulfuric acid at a 15 mL/g acid-to-cellulose ratio at 45 °C for 60 min under constant stirring. Cold distilled water was added (five times the amount of the hydrolyzed cellulose) to end the acid hydrolysis reaction. The hydrolyzed cellulose was washed and nanocrystals were separated from the solution by centrifuging (4,000 rpm, 20 min). The precipitate was then dialyzed against water for 4 days using membranes with a molecular weight cutoff of 12,000–14,000 (Fisher brand, Pittsburgh, PA) until a constant neutral pH was achieved. The cellulose nanocrystals were dispersed in water, ready for subsequent characterization.

## 2.4 Characterization

### 2.4.1 Fourier transform infrared spectroscopy (FTIR)

FTIR was performed using a Perkin Elmer FTIR-ATR spectrometer (Spectrum One, Perkin Elmer, USA). Samples were placed on a diamond crystal of an attenuated total reflectance (ATR) accessory. All spectra were collected over a range of 4000 to 600  $\text{cm}^{-1}$  at 4  $\text{cm}^{-1}$  resolution with 16 scans. Samples were recorded after each bleaching, and freeze-dried cellulose nanocrystals were measured after acid hydrolysis.

### 2.4.2 Transmission electron microscopy (TEM)

Individual droplets of (0.001 wt%) of switchgrass cellulose nanocrystal suspension were deposited on amorphous carbon-coated electron microscope grids and mixed with 2% uranyl acetate for 1 min, negative-stained, and allowed to dry. The grids were placed into a Cs-STEM aberration-corrected transmission electron microscope (Libra 200 MC, Zeiss), which was operated at a 200 kV accelerating voltage.

### 2.4.3 Wide angle X-ray diffraction (WXR)

X-ray diffraction analysis was carried out using a Scintag DMC 008 X-ray diffractometer and Ni-Filtered Cu  $K\alpha$  radiation ( $\lambda=1.5406 \text{ \AA}$ ). Powder samples were pressed into flat disks and attached to the slide using double-sided adhesive tape. A long fine-focus X-ray tube was prepared with tube voltage set to 40 kV and amperage set to 40 mA (Thygesen et al., 2005). Diffraction intensity as a function of  $2\theta$  was recorded over scattering ranges from  $5^\circ$  to  $40^\circ$  (step size= $0.02^\circ$ , scanning rate= $2 \text{ s/step}$ ). Crystalline structures, including the degree of crystallinity and the crystal size, were examined.

The crystallinity index (CrI) was calculated from diffraction patterns by using the following equation (Segal et al., 1959):

$$\text{CrI} = \frac{(I_{200} - I_{\text{am}})}{I_{200}} \times 100 \quad (1)$$

$I_{200}$  is the peak intensity at plane (200) ( $2\theta=22.4^\circ$ ), and  $I_{\text{am}}$  is the minimum intensity at the valley between plane (200) and (110) ( $2\theta=18^\circ$ ).

The dimension of the crystal with  $hkl$  Miller indices,  $D_{hkl}$ , was described by Scherrer's expression:

$$D_{hkl} = K\lambda / (\beta_{\frac{1}{2}} \times \cos\theta) \quad (2)$$

where  $K=0.94$ ,  $\theta$  is the diffraction angle,  $\lambda=0.154$  is the X-ray wavelength and  $\beta_{\frac{1}{2}}$  is the peak width at half maximum intensity of [002] peak.

#### **2.4.4 Atomic force microscope measurement (AFM)**

The cellulose nanocrystals' morphology was studied using the atomic force microscope (AFM, Park Systems Corporation). Measurements were performed under ambient conditions (70°F, 30% RH). The non-contact mode was used for this study. Aluminum-coated silicon cantilevers with a spring constant of 40 N/m and resonant frequency of 300 kHz (Nano-science Instruments) were selected, with a conical tip whose radius of curvature was around 8 nm. XEI software was used for the image processing. Samples were prepared by depositing one drop of switchgrass CNC suspension (0.001 wt%) on the freshly cleaved mica substrate, and then air-dried. Images were scanned at low voltage mode under 0.8 Hz scan rate and 512-by-512-pixel resolution for the purpose of detecting the fine structures. The length and height values of the switchgrass CNCs were selected to describe the shape based on consideration of the possibly axisymmetric structure of the CNC fibers. A measurement of the width by AFM was not attempted due to the artifacts caused by sample-tip convolution (Allen et al., 1992). Over 90 CNCs were scanned and measured. To better understand the morphology of switchgrass CNC, the heights of the five locations of particular interest along the individual CNC were measured and recorded.

### 3. Results and discussion

#### 3.1 Isolation of cellulose from switchgrass

Cellulose was separated from switchgrass powders by means of de-waxing, delignification and hemicellulose-removing processes. FTIR spectra of switchgrass fibers after each treatment confirmed that the white product obtained following the isolating process was nearly pure cellulose (Figure I-1). The spectra also verified the removal of lignin in the delignification step based on the absorption peaks of  $1609\text{ cm}^{-1}$  (aromatic skeletal vibrations),  $1510\text{ cm}^{-1}$  (aromatic skeletal vibrations) and  $852\text{ cm}^{-1}$  (C-L out-of-plane deformation). Hemicellulose was proven to be absent in terms of the absorption peak of  $1736\text{ cm}^{-1}$  (carbonyl stretching) and  $1267\text{ cm}^{-1}$  (C-O stretching). The total yield of cellulose from switchgrass reached 32%, agreeing with other studies (Sladden et al., 1991).

The crystalline behaviors of raw switchgrass and the intermediates during the non-cellulose substance removal process were analyzed by wide-angle XRD (Figure I-2). A crystalline intensive peak at  $2\theta = 22.4^\circ$ , corresponding to (200) lattice plane, and a shoulder peak in the region of  $2\theta = 13-17^\circ$ , corresponding to (110) and (1-10) lattice plane, were observed. The high peak intensity of switchgrass CNCs indicated that crystallinity was dramatically increased by the elimination of non-cellulose components and amorphous materials such as lignin and hemicellulose. The crystallinity of raw switchgrass chemically extracted intermediates, and synthesized cellulose nanocrystals were calculated from WXR and are summarized in Table I-1. The switchgrass raw material exhibited the smallest crystallinity, 32%, due to the presence of hemicellulose and lignin. The crystalline index was found to increase with the series of chemical treatments on switchgrass fiber. The sulfuric acid hydrolyzed cellulose nanocrystal had a crystallinity index (CrI) of 81%, in the same range as many other reports (Lin and Dufresne, 2014).

## 3.2 Morphology of switchgrass CNC

### 3.2.1 Length, width, height, and roughness measurement

The cellulose solution changed from yellow to an opalescent color during acid hydrolysis, visibly indicating the formation of nanoparticles. The lengths and heights of switchgrass cellulose nanocrystals were measured from AFM images by drawing line profiles (Figure I-3a, b). The typical line profile along the CNC' longitudinal direction indicated that the height of individual CNC in the center is taller than at either end. The width of the switchgrass CNCs was measured from TEM images (Figure I-3c,d). Intensity profiles drawn across individual CNC reveal that overfocus during imaging presents a “mountain” shape that shows the width of CNCs.

Five locations on individual CNC (at the ends, the midpoint, and at the quarter and three-quarter points) were investigated. The size distribution (Figure I-4) of the switchgrass CNCs ranged from 50 nm to 450 nm in length, with an average length of 163.7 nm. The midpoint height of the switchgrass CNC fibers ranged from 1.36 nm to 10.6 nm with an average height of 4.1 nm, while the width ranged from 2.6 nm to 7.85 nm with an average width of 5.07 nm and an average aspect ratio of 48.7. As a point of comparison, the morphologies of CNCs isolated from various resources are summarized in Table I-2 (Rosa et al., 2010, Teixeira et al., 2010, Flauzino Neto et al., 2013, Santos et al., 2013). Compared to other resources derived CNCs, switchgrass CNCs yields higher aspect ratio except for pineapple leaf CNCs. This exceptionally high aspect ratio makes it come into contact with other CNC rods easier, as a result, has great potential to improve reinforcement when making nanocomposite (Hajji et al., 1996). Note that the height measured at the midpoint of switchgrass CNCs lies in the same range as do those from coconut-husk fibers, bamboo fiber, eucalyptus, and sisal, but that it is lower than the heights of CNCs obtained from other resources. The switchgrass CNCs' heights at five locations along the fibers' longitudinal axes were measured from an AFM image by drawing a profile line (Figure I-3).

Statistical analysis shows that the right end is similar to the left end in height ( $p=0.7232$ ), as is the height measured between quarter and three-quarter locations ( $p=0.8895$ ). However, the heights are significantly different among measurements taken at the midpoints, two ends, and two quarter locations. The midpoint width of switchgrass CNC fiber ranges from 2.6 nm to 7.9 nm, with an average number of 5.1 nm. A whisker box plot (Figure I-5) shows a width

comparison measured along switchgrass CNCs' longitudinal axis from TEM images. No statistical difference was observed between the two ends ( $p=0.4124$ ) or between the quarter and three-quarter locations ( $p=0.5755$ ). Statistical analysis shows that the height and width values were largest at the midpoint of each individual nanocrystal and exhibited a step-wise decrease toward the ends (Figure I-5). A similar trend has been observed and mentioned elsewhere (Moon et al., 2011), suggesting an imperfect exfoliation or incomplete reaction during acid hydrolysis. This observation is consistent with literature data, which showed the erosion of CNCs ends. The two sharp ends are probably the angular places where eroding took place during acid hydrolysis, since it is favored in these region, owing to the high accessibility and lower crystallinity.

The negative stain treatment on the CNC for TEM measurement may make defining the contour challenging and may possibly lead to a biased measurement of width. Roughness measurements were performed on the nanocrystals by drawing a profile line on the surface along the longitudinal axis. One-dimensional average roughness was calculated using Gwyddion software. The corresponding roughness profiles reveal large amplitudes between peaks and valleys, indicating an uneven surface. The roughness of the nanocrystal surface was found to have an average value of [0.4, 0.43, 0.45] nm, a finding that is consistent with previous research on Valona microcrystals (Baker et al., 1997). Roughness values follow a normal distribution (Figure I-4). The rough surface is attributed to imperfect exfoliation during hydrolysis (Figure I-3). Rough surfaces on cellulose nanocrystals increase the radial clamping forces between the fiber and polymer when cellulose serves as a reinforcing material in composite (Chawla et al., 1995).

### **3.3 Size distribution**

#### **3.3.1 Data imputation**

Collecting width and height measurements data from all five locations of interest on each individual nanocrystal was quite challenging. CNCs have a tendency to aggregate during sample preparation. There are many missing data, and Little's Missing Completely at Random (MCAR) test shows that data are missing in a complete random way ( $p=0.4$ ). Expectation maximization

was therefore selected as an appropriate method of imputing data. Detailed information is not listed in this paper but is available in other places (Zeng, 2011).

### 3.3.2 Information criterion and distribution selection

We fitted the data from each of the five groups to the normal, lognormal, LEV, log-logistic, and logistic for the purpose of determining the underlying distribution of the data. Akaike's Information Criterion (AIC) was used to determine the distribution of best fit (Table I-3). The distribution with the smallest AIC was considered the best fit for each data set, and the switchgrass CNCs lengths were found to be best fitted by a lognormal distribution. The result was in good agreement with the research of Elazzouzi-Hafraoui and many others (Epstein, 1947, Elazzouzi-Hafraoui et al., 2008). The heights measured were lognormal-distributed at the three-quarter position, LEV-distributed on the midpoint, normally distributed on the two end positions and log-logistic-distributed at the quarter position. It has been shown by other researchers that lognormal functions are classically found to describe the particle size distribution (Epstein, 1947, Elazzouzi-Hafraoui et al., 2008). It is important to note that lognormal distribution ranks high in all height distributions, but not in width distributions. The width measured is logistic-distributed at the midpoint and three-quarter locations, normal-distributed on the left end and quarter positions, and log-logistic-distributed on the right end position. This phenomenon can be ascribed to measurement aberration from TEM images affected by negative staining.

Lognormal distribution, used to fit the aspect ratio histogram and the property density function, is given by

$$f(x) = \frac{\exp\left(-\frac{1}{2}\left(\frac{\ln(x) - \mu}{\sigma}\right)^2\right)}{x\sigma\sqrt{2\pi}} \quad (3)$$

where  $x$  is the aspect ratio with normal distribution;  $\mu$  and  $\sigma$  are location and scale parameters, respectively. Fitting the raw data using Eq. 3, we obtain  $\mu=3.8$  and  $\sigma=0.4$ .

The aspect ratio distribution is described by



$$f(x) = \frac{\exp\left(-\frac{1}{2}\left(\frac{\ln(x)-3.8}{0.4}\right)^2\right)}{x \times 0.4 \times \sqrt{2\pi}} \quad (4)$$

The expectation function is the average aspect ratio:

$$l/d = e^{\mu+\sigma^2} = 48.7 \quad (5)$$

where  $l$  is the length and  $d$  is the diameter of CNC. The calculated result from lognormal distribution is 48.7, which achieves the same value as the measured average aspect ratio. This demonstrates that the aspect ratio data fit very well with a lognormal distribution (Ten et al., 2012).

### 3.4 Estimation of surface morphology and crystallite structure of CNC

As was found previously, naturally produced organisms hold cellulose I structure, which has two polymorphs, I $\alpha$  and I $\beta$ . The cellulose I $\beta$  with two-chain monoclinic crystal structure is dominant in most of the higher plants. The observation of (1-10), (110), (200) peaks in WXR D results shown in Figure I-2 confirmed that switchgrass CNCs were cellulose I $\beta$  (Sugiyama et al., 1991). Many hypothetical models of CNC's cross-section shape have been recently reported. However, there is still considerable controversy about it and no strong validation on the proposed model due to the limited techniques of high-resolution observation and complex data analysis (Gu et al., 2013). On the basis of the microscopy, spectroscopic methods and supramolecular structure of the cellulose I $\beta$ , the 36 and 24 chain models were proposed with the cross-section in hexagonal, diagonal, rectangular and squared shape (Sugiyama et al., 1991, Ding and Himmel, 2006, Fernandes et al., 2011, Matthews et al., 2006). The widely accepted cross-section model for higher plant cellulose crystal has been described as a 36-chain model with square cross-section. The crystallite widths (in angstroms) of raw switchgrass, the chemically extracted intermediates, and the switchgrass CNC calculated using Scherrer's expression from the half-width at half height of the peaks obtained from the diffraction profiles are summarized in Table I-1. The result is very similar to the crystalline size reported for bamboo, corn stover, norway spruce, sugarcane bagasse and avicel (Brito et al., 2012, Elazzouzi-Hafraoui et al., 2008, Thygesen et al., 2005). According to XRD results, the cross-sectional [when the (110) and (1-10)

plane surface is exposed] dimensions of switchgrass nanocrystalline are proposed to be a square with dimensions  $3.3 \times 3.3 \text{ nm}^2$ , which is smaller than the height and width measured from AFM and TEM. In addition, the AFM measurement of height and TEM measurement of width on five specific locations were compared along the fiber's longitudinal direction. The average data of measured width are significantly larger than the measured height. There are some reasons to explain the difference. First, there may be some disordered molecular chains exiting at the surface of individual CNC because the crystallinity of switchgrass CNCs under harsh acid treatment is only 81% from XRD. Secondly, the artifacts caused by beam damage, negative stain treatment on the sample during TEM measurement, the blunt-tip effect during AFM measurement, and the complicated peak deconvolution for analyzing WXR data could introduce variations (Gu et al., 2013). These potential effects should not be conclusively excluded. Based on these observations and previous literature, a cross-sectional shape for switchgrass CNC would be proposed with the caveat that that it may be closer to either an elliptical or rectangular shape than a square (Lin and Dufresne, 2014, Majoinen et al., 2013). A schematic illustration of the proposed cross-section in terms of glucan chains is shown in Figure I-6. It could be described as a crystalline core covered by some layers of subcrystalline. Both the amorphous region and the glucan chains along the external surfaces of the fibrils are susceptible to acid exposure, causing the acid cleavage initiated from these localized regions to occur before it does in the crystalline regions. Accordingly, the acid hydrolysis starts from the amorphous cellulose; it then erodes and exposes the fibrils' unstable ends, resulting in the peeling off of individual CNC and the formation of a rough surface induced by surface erosion (Guo and Catchmark, 2012). Additionally, there will be more acid reaction on the fibril ends and sharp edges than at other positions along the fibrils' lengths because of the larger reaction areas.

#### **4. Conclusions**

In summary, cellulose nanocrystals were extracted from switchgrass using sulfuric acid. The FTIR spectra confirmed the removal of lignin and hemicellulose during the cellulose-isolating process. The quantitative and statistical measurement of individual CNC morphology by AFM, TEM and XRD were compared. Particle size distributions on five target locations along individual CNC fibril axis were statistically reported and found to fit very well with a lognormal

distribution. We demonstrated on individual CNC that both thickness and width measured by AFM and TEM separately give the greatest value at the midpoint along the fibril axis, but that they showed a step-wise decrease proceeding to the two sharp ends. The estimated cross-section of individual CNC derived from switchgrass seems to be a rectangle or elliptical shape with an approximately 3~5 nm lateral element length. The high aspect ratio and roughness of switchgrass CNCs makes it ideal potential filler for making high-strength nanocomposite. The description of the shape of individual nanocrystals presented herein will not only benefit the model selection, prediction, and design of nanocomposite with regard to the reinforcing effect, but will also facilitate further research on the complex cellulose nanocrystalline structure and interactions among nanocrystals.

## Appendix I

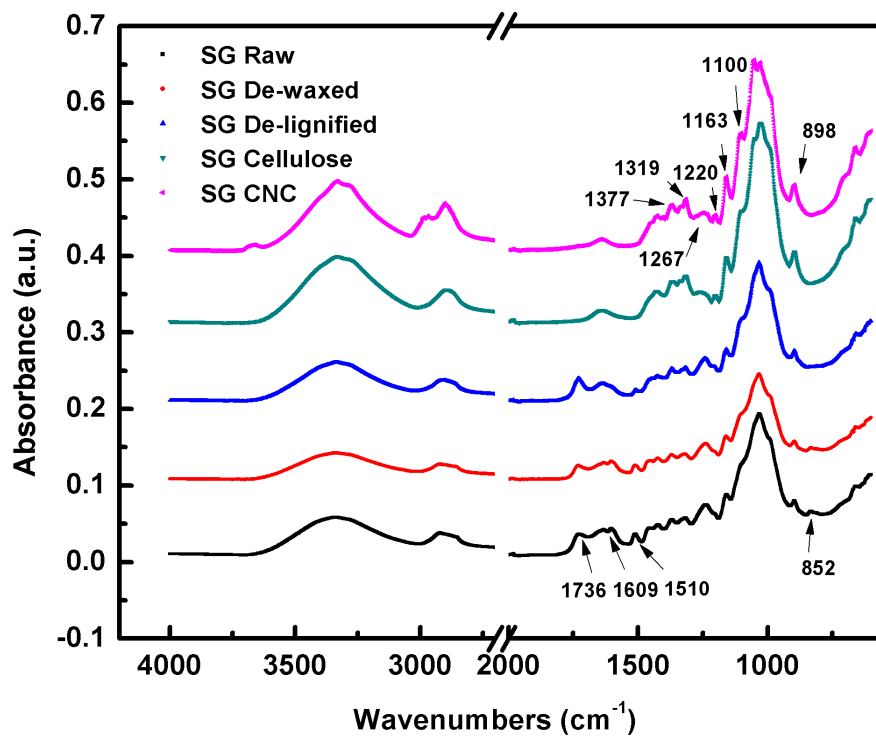


**Figure I- 1** FTIR spectrum of switchgrass powder, de-waxed powder, delignified powder, hemicellulose extracted powder, and cellulose nanocrystals

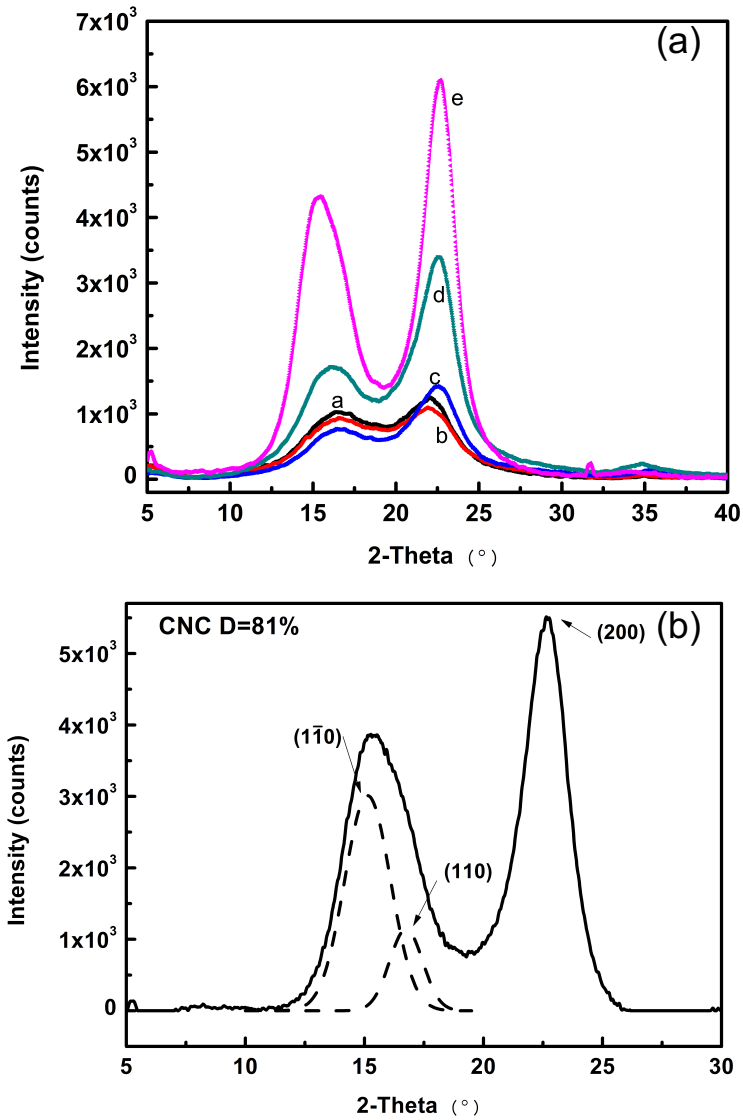


**Figure I- 2** (a) X-ray diffraction patterns of a) switchgrass, b) de-waxed switchgrass, c) delignified switchgrass, d) switchgrass cellulose, e) cellulose nanocrystals (b) peak deconvolution of cellulose nanocrystal

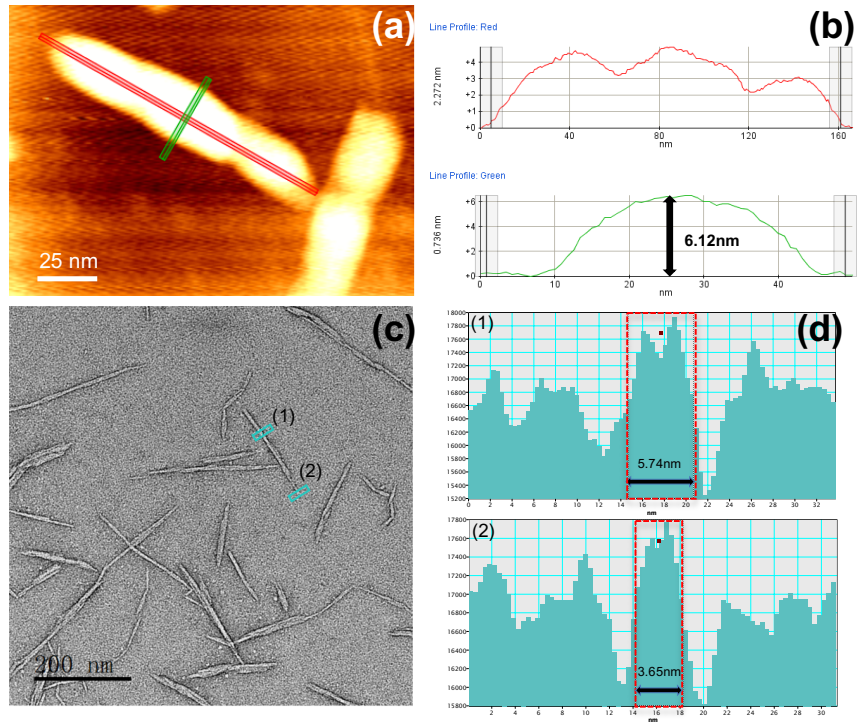


**Figure I- 3** Atomic force microscopic image and line profile of individual switchgrass CNC fiber. (a) CNC topography image; (b) CNC line profiles; (c) Transmission electron micrographs of switchgrass CNCs; (d) Intensity profile scanned across individual CNC on two locations

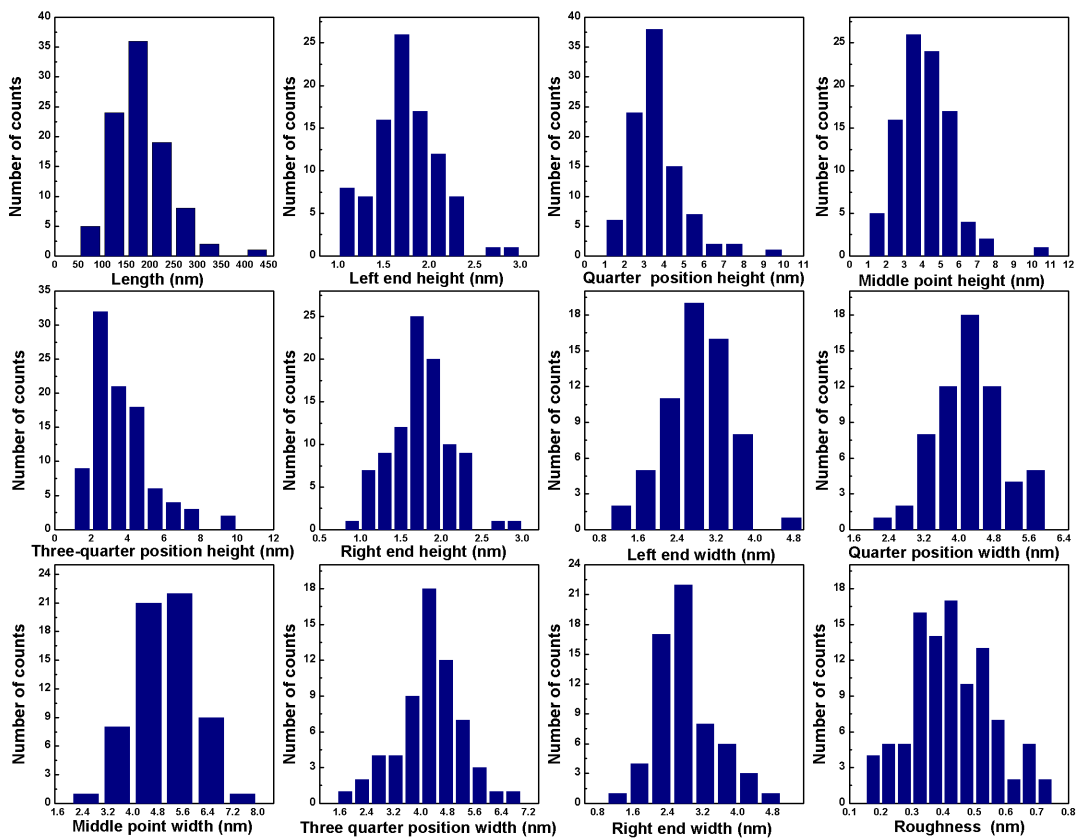


**Figure I- 4** Length, roughness, height and width distribution histograms of switchgrass CNCs, where height and length were measured from the AFM image and width was measured from the TEM image. The continuous curves correspond to fitting of the data using a log-normal function.



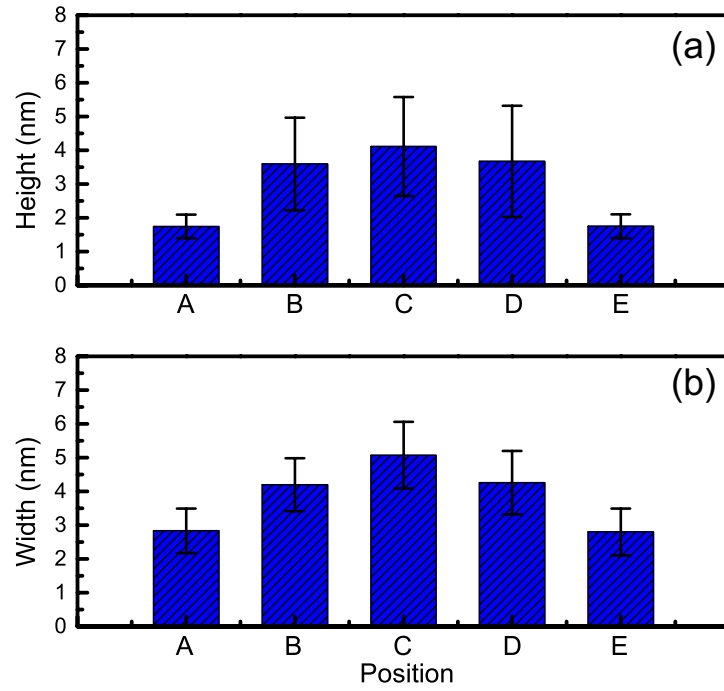


**Figure I- 5** Plots of switchgrass CNC samples' (a) height and (b) width along their longitudinal axis (A) Left end (B) Quarter position (C) Middle point (D) Three-quarter position (E) Right end

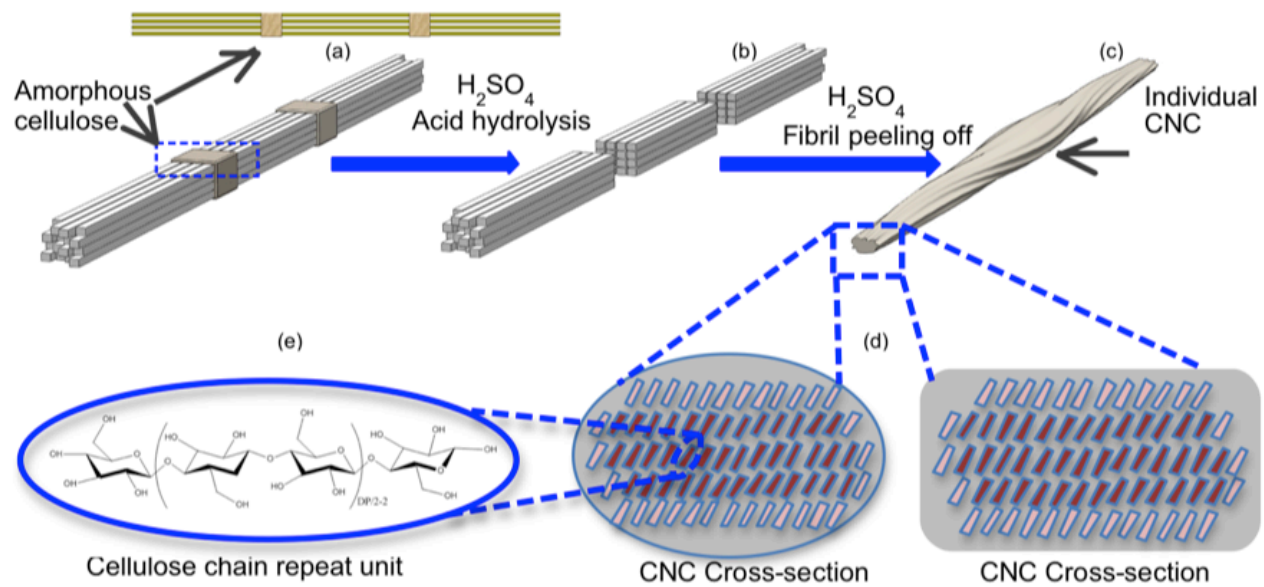


**Figure I- 6** Schematic representation of individual switchgrass CNCs. (a) Cellulose microfibrils (b) removal of disordered/amorphous region during acid hydrolysis(c) individual CNC (d) Cross-section of CNCs; (e) cellulose chain repeat unit.

**Table I- 1** Crystallinity index (CrI) and crystallite size of raw switchgrass, dewaxed switchgrass, delignified switchgrass, switchgrass cellulose, and cellulose nanocrystals (CNCs), estimated by Scherrer's expression

	<b>SG Raw</b>	<b>De- Waxed</b>	<b>De- Lignified</b>	<b>SG Cellulose</b>	<b>SG CNC</b>
Crystalline Index (CrI) (%)	32	27	59	62	81
Crystallite size (Å) with respect to [200] peak	21(1)	22(2)	26(1)	31(1)	34(1)
Crystallite size (Å) with respect to [110] peak	21(1)	21(2)	18(3)	15(2)	33(1)
Crystallite size (Å) with respect to [1-10] peak	21(1)	21(3)	35(10)	35(8)	33(1)

*Note: the numbers in parenthesis are standard deviations.*

**Table I- 2** Summary of geometrical shapes of cellulose nanocrystals from different sources

<b>Source</b>	<b>Length (nm)</b>	<b>Diameter/ Thickness (nm)</b>	<b>Width (nm)</b>	<b>Aspect Ratio l/d</b>	<b>Experimenta l Techniques</b>	<b>Reference</b>
<b>Switchgrass</b>	163.7 ± 59	4.11 ± 1.47	5.07 ± 1	48.7 ± 21.7	AFM and TEM	This research
<b>Coconut husk</b>	194 ± 70	5.5 ± 1.5	5.5 ± 1.5	39 ± 14	TEM	(Rosa et al., 2010)
<b>Bamboo</b>	100 ± 28	4.5 ± 0.9	8 ± 3	22	AFM & TEM	(Brito et al., 2012)
<b>Eucalyptus</b>	100 ± 33	4.5 ± 1	7 ± 1	22	AFM & TEM	(Brito et al., 2012)
<b>Sisal</b>	119 ± 45	3.3 ± 1	6 ± 1	36	AFM & TEM	(Brito et al., 2012)
<b>Rice straw</b>	119 ± 39	5.06 ± 1.73	11.2 ± 3.6	10.5	AFM & TEM	(Lu and Hsieh, 2012)
<b>Kenaf bast</b>	158.4 ± 63.6	12.0 ± 3.4	-	13.2	TEM	(Kargarzadeh et al., 2012)
<b>Cotton</b>	135 ± 50	19 ± 10	-	7.1	AFM & TEM	(Teixeira et al., 2010)
<b>Soy hulls</b>	122.7±39.4	-	4.43±1.2	29.41±5 3	TEM	(Flauzino Neto et al., 2013)
<b>Pineapple leaf</b>	249.7±51.5	4.45±1.41	-	60.1±19 .5	AFM	(Santos et al., 2013)

**Table I- 3** AICc summary table for cellulose nanocrystal height and width distribution

	AICc	Normal	Lognormal	LEV	Logistic	Loglogistic
Height	Length	1047.9	1039.4*	1039.9	1046.2	1041.0
	Middle point	345.4	334.8	334.8*	341.2	336.4
	Left end	71.1*	72.6	79.1	71.3	73.4
	Right end	75.1*	78.1	85.2	75.3	78.0
	Quarter position	332.7	311.9	310.9	320.8	309.1*
	Three-quarter position	367.1	336.5*	339.1	360.1	340.1
Width	Middle point	177.2	178.6	183.8	176.0*	176.3
	Left end	127.6*	134.1	137.9	128.6	132.6
	Right end	133.5	131.5	133.3	132.3	128.9*
	Quarter position	148.9*	154.3	161.4	149.7	151.8
	Three-quarter position	171.2	174.9	185.8	169.4*	174.9

*Note: \*The corresponding distribution has the minimum AIC value, indicating the best fit.*

## **CHAPTER II**

# **ULTRALIGHT CARBON AEROGEL FROM NANOCELLULOSE AS A HIGHLY SELECTIVE OIL ABSORPTION MATERIAL**

A version of this chapter was originally published by Y. Meng, T.M. Young, P. Liu, C. I. Contescu, B. Huang, and S. Wang.

Y. Meng, T.M. Young, P. Liu, C. I. Contescu, B. Huang, and S. Wang. “Ultralight carbon aerogel from nanocellulose as a highly selective oil absorption material.” *Cellulose* (2015) 22: 435-447.

Authors:

Y. Meng, T. M. Young, B. Huang, S. Wang

*Department of Forestry, Wildlife and Fisheries, Center for Renewable Carbon, University of Tennessee, Knoxville, TN, USA*

P. Liu

*Department of Materials Science and Engineering, University of Tennessee, Knoxville, TN, USA*

C. I. Contescu

*Oak Ridge National Laboratory, Oak Ridge, TN, USA*

B. Huang

*College of Engineering, Fujian Agriculture and Forestry University, Fuzhou, China*

Y. Meng’s primary contribution to this paper includes identifying the research objective, design and conduct of the experiments, process and interpretation of the data, drafting the paper.

Co-researchers’ contributions are listed as follows:

T. M. Young revised and language polished the paper

P. Liu performed TEM and SEM observation and worked with Yujie to analysis the data.

C. I. Contescu revised the paper and performed the Nitrogen adsorption-desorption experiment.

B. Huang worked with Yujie Meng to analyze the experimental data.

S. Wang identified the research objective, provided research guideline and revised the paper.



## Abstract

The synthesis of a sponge-like carbon aerogel from microfibril cellulose (MFC), with high porosity (99%), ultra-low density ( $0.01 \text{ g/cm}^3$ ), hydrophobic properties ( $149^\circ$  static contact angle) and reusability is reported in this paper. The physical properties, internal morphology, thermal properties, and chemical properties of carbon aerogels heat-treated at 700 and 900 °C (Samples C-700 and C-900) were examined. Stabilization and carbonization parameters were optimized in terms of residual carbon yield. The BET surface area of Sample C-700 ( $521 \text{ m}^2/\text{g}$ ) was significantly higher than of Sample C-950 ( $149 \text{ m}^2/\text{g}$ ). Graphitic-like domains were observed in C-950. The highest normalized sorption capacity ( $86 \text{ g/g}$ ) for paraffin oil was observed in sample C-700. The removal of hydrophilic function groups during carbonization causes carbon aerogel to present highly hydrophobic properties. Carbon aerogel's ability to absorb oil is enhanced by its highly porous 3D network structure with interconnected cellulose nanofibrils.

## 1. Introduction

Oil spills and oily industrial wastewater are of environmental concern and have economic consequences, driving oil-related industries to look for new and more effective technologies for cleaning up and reclaiming the oil spills. Oil recovery using absorbent materials is superior to many other industrial methods for oil recovery, such as physical collection, biodegradation, or in situ burning, because of the lower costs, higher efficiency and higher recyclability of most absorbents (Hubbe et al., 2013). Although conventional absorbent materials have been widely used for large-scale oil spill cleanup, their absorption efficiency is greatly impaired by the high water affinity of most natural materials (Peng et al., 2013). In contrast, absorbents from natural precursors with both hydrophobic and oleophilic properties have the potential of being both practically and commercially important.

Nanocellulose has attracted scientific and practical interest relatively recently not only because of its bio-based, sustainable, nontoxic, abundant, and renewable nature, but because of its unique intrinsic properties (Dong et al., 2013). In particular, microfibril cellulose (MFC) consists of long, flexible fibers cleaved from the hierarchy of plant or wood cellulose by mechanical processes (Moon et al., 2011, Wang and Cheng, 2009, Cheng et al., 2007). The high surface area and high aspect ratio of MFC are beneficial for the formation of an ultrafine three-dimensional network structures in an aqueous environment. As a consequence, attention has turned towards converting natural cellulose nanofibrils into cellulose aerogels with low density, high porosity, and low thermal conductivity, as needed for various applications (Li et al., 2011, Chen et al., 2011, Hoepfner et al., 2008, Jin et al., 2011, Cervin et al., 2012). The hydrophilic property of nanocellulose aerogel resulting from its molecular structure is an obvious limitation on its capacity for water-oil separation. Surface functionalization and conversion by pyrolysis into carbon aerogel provide ways to overcome this difficulty (Jin et al., 2011, Korhonen et al., 2011, Liu et al., 2013, Dong et al., 2013). It has been reported that graphene aerogel, carbon nanotube aerogel, carbon fiber aerogel, and carbon microbelts aerogel are capable of separating water and oil (Li et al., 2014, Wu et al., 2013c, Hu et al., 2013, Gui et al., 2011, Li et al., 2010, Upadhyayula et al., 2009). However, these materials are not necessarily environmentally or

economically desirable because they are obtained either by means of complex syntheses that require large amounts of chemical reagents, or through high-energy input processes.

This paper reports on the synthesis and properties of sponge-like bulk materials made from nanocellulose and their potential to effectively absorb oil. The main point is that, using a nanoscale material as a precursor allows thermal treatment temperatures to be reduced while retaining important properties (porous structure, surface area, hydrophobic properties) that are similar to those of other carbon absorbent materials synthesized from conventional cellulose-based precursors. This study uses a “green” synthesis approach that involves 1) freeze-drying a mixture of microfibril cellulose and applying wet resin to create a 3D porous aerogel, and 2) thermal treatment to achieve both hydrophobic and oleophilic properties.

In this study, the oil absorption properties of this product are characterized, and the effects of porosity and density differences on the resulting hydrophobic and oleophilic capabilities are investigated. The advantages of this new product are its low cost, its use of renewable and sustainable raw materials, its non-toxicity, and its biodegradability. This ultralight and extremely hydrophobic carbon aerogel can selectively separate and remove large-scale oil spills from water surfaces and can be used potentially for absorbing of a variety of other organic solvents.

## **2. Materials and experimental section**

### **2.1 Materials**

Cellulose microfibrils with a solid content of 10% were obtained from commercial sources (Celish KY-100G, Daicel Corporation, Japan). Cross-linker Kymene™ resin (Ashland Hercules Inc., USA) was purchased and added into the microfibril cellulose suspension.

### **2.2 Preparation of MFC aerogel and carbon aerogel**

A mixture of 2 wt % aqueous suspension of cellulose microfibril and cross linker resin (5 wt % of dry MFC) was poured into open-ended copper pipes (1.5 inch in length and 0.81 inch in diameter) and sealed with aluminum foil. The samples were then placed into liquid nitrogen for

one minute for rapidly freezing, following which the aluminum foil was removed and the samples were freeze-dried in a vacuum lyophilizer (Labconco, Inc., Kansas City, MO) at -51 °C for three days. Ultra-light sponge-like aerogel was obtained. Samples were oven-heated at 120 °C for 3 hours to promote cross-linking in order to form a three-dimensional network. The aerogel samples were stabilized in air (20 mL/min) and carbonized in nitrogen (20 mL/min) using a Lindberg /blue M Mini-Mite tube furnace (Thermo Scientific). The stabilization stage included (1) heating the sample from room temperature to 180 °C at a rate of 10 °C/min in air; (2) increasing the temperature from 180 to 230 °C at a rate of 5 °C/min in air; and (3) increasing the temperature from 230 to 320 °C in air. Different heating rates ranging from 0.2 to 5 °C/min were used in the latter step. The carbonization stage included (4) increasing the temperature from 320 °C to peak temperatures of 700 °C or 950 °C at a rate of 5 °C/min in nitrogen and holding for 15 min. Samples were then cooled to room temperature. The carbon aerogels were labeled C-700 and C-950, according to their carbonization temperature.

### 2.3 Characterization of MFC aerogel and carbon aerogel

The bulk density  $\rho$  of MFC aerogel and carbon aerogel was calculated using Equation (1):

$$\rho = m / V \quad (1)$$

where  $m$  is the weight and  $V$  is the bulk volume. The porosity  $P$  of cellulose microfibril aerogel and carbon aerogel were calculated using Equation (2):

$$P(\%) = (1 - \rho_a / \rho_m) \times 100\% \quad (2)$$

where  $\rho_a$  is the bulk density and  $\rho_m$  is the skeletal density of microfibril cellulose and carbon fibers, respectively. The skeletal density was measured by helium ultrapycnometry (Quantachrome Corp). The inner structures of MFC aerogel and carbon aerogel were observed by means of scanning electron microscopy (SEM, Zeiss Auriga SEM/FIB crossbeam workstation). The MFC aerogel was coated with a thin layer of gold to provide conductivity and to protect the sample from electron beam damage. An ultrastructure of the carbon aerogel was characterized by transmission electron microscopy (TEM, Zeiss Libra 200 MC). The carbonized aerogel was ground into powder and dispersed into distilled water. TEM samples were prepared by depositing suspension drops (0.001 % w/v in water) on amorphous lacey carbon-coated

electron microscope grids and were then allowed to dry. The TEM was operated at a 200 kV accelerating voltage. Thermal stability and carbonization yield were determined using thermogravimetric analyzers (TGA; Perkin–Elmer 7 series; Perkin–Elmer Cetus Instruments, Norwalk, CT.). The heating program was set up to mimic the stabilization/carbonization process. The TGA program for the MFC aerogel sample without stabilization was set at 5 °C/min heating rate from room temperature to peak temperature. Fourier transform infrared spectroscopy (FTIR) was performed on the MFC aerogel and the carbon aerogel using a Perkin Elmer FTIR-ATR spectrometer (Spectrum One, Perkin Elmer, USA). Samples were placed on the diamond crystal of an attenuated total reflectance (ATR) accessory. All spectra were collected over the range of 4000 to 600  $\text{cm}^{-1}$  at 4  $\text{cm}^{-1}$  resolutions with 16 scans. The static contact angle was measured on the carbonized aerogels at room temperature using the sessile drop method. Changes of contacted angle were measured and recorded by using a JC2000A contact angle meter (Shanghai Zhongchen Digital Technology and Equipment Co., Shanghai, China). A droplet of deionized water was deposited by a syringe, which pointed vertically down onto the surface of the carbon aerogels. A high-resolution camera sequentially recorded the droplet images on the surface as a function of time. The contacted angle was measured by goniometer. Nitrogen adsorption-desorption analysis of the carbon aerogels was carried out on an Autosorb 1C instrument (Quantachrome Instruments). The Brunauer-Emmett-Teller (BET) surface area ( $\text{m}^2/\text{g}$ ) was calculated from the nitrogen adsorption data at 77 K in a relative pressure range from 0.05 to 0.35. The pore size distribution was calculated by the non-local density functional theory (NLDFT) from the adsorption branch of the isotherm. The mass percent of the elements (carbon, hydrogen and nitrogen) in the MFC aerogel and carbon aerogel was determined by a 2400 Series II CHNS/O elemental analyzer (PerkinElmer).

## **2.4 Oil sorption experiments**

Oil sorption experiments were carried out using canola oil (Wesson, ConAgra Foods, Inc.), diesel oil (BP PLC gas station), paraffin oil (BP PLC gas station) and pump oil (motor oil, Castrol North America Inc.). Carbon aerogel sponges that had been heat-treated at two peak temperatures (700 °C and 950 °C) were weighed first and immersed into oil for variable times, totaling 1600 seconds. After each immersion, the sponge was taken out, drained for 30 seconds

to wipe away the excess oil, and immediately transferred to a tarred pan. The process was repeated and thus the weight increase rate of carbon aerogel was measured as a function of time. Sorption kinetics were analyzed and calculated as the ratio of oil absorbed to dry absorbent weight (ASTM F726, standard method of testing sorbent performance of absorbents E1-1993):

$$Q_t = (m_{st} - m_o) / m_o \quad (3)$$

where  $Q_t$  is the oil absorbency,  $m_{st}$  is the weight of carbon aerogel at time  $t$  of oil tests and  $m_o$  is the initial dry weight of carbon aerogel. The oil absorbency ratio by weight was plotted as a function of time. After the carbon aerogels reached sorption saturation, the samples were immersed into ethanol to completely remove the absorbed oil, oven-dried at 60 °C overnight, weighted, and reused for subsequent absorption testing. The reusability of the carbon aerogel on oil absorption was verified over 10 cycles.

### 3. Results and discussion

#### 3.1 Thermal decomposition kinetics

The oxidative stabilization and carbonization behavior of MFC aerogel was studied by TGA. Thermogravimetric (TG) and derivative thermogravimetric (DTG) thermograms are shown in Figure II-1. The carbon yield of MFC aerogel without stabilization (6.2 %) was found to be significantly lower than that of samples with stabilization treatment.

Oxidative stabilization was performed to promote cross-linking and avoid “melting” or shrinkage of MFC aerogel. Three regions of weight loss at different temperature ranges were seen. A barely detectable weight loss occurred between 105 °C and 230 °C. A rapid mass loss process started from 230 °C and terminated at 320 °C, with the sample residual mass between 15% and 20%. During the oxidative stabilization process, it has been found that the splitting of glycosidic bonds in cellulose’s macromolecular chains leads to the formation of a large number of oxygenated compounds (Tang and Bacon, 1964a). Therefore, in order to achieve a high char yield, attention was given to the rapid mass loss processes. It was found that the heating rate has a considerable influence on the mass loss between 230 °C and 320 °C. The onset of degradation temperatures and the weight loss of carbonized aerogel under different heating rates are summarized in Table II-1. The onset and decomposition temperatures of stabilized MFC aerogels

increased with the increase in the heating rate. Because decomposition is triggered by temperature and limited by the diffusion of gases from the microfibril cellulose mass, decomposition started earlier when the samples were subjected to low heating rates than it did at high heating rates. This “thermal inertia” effect is common to TGA experiments when the sample comes slowly into equilibrium with the external furnace temperature. A slow weight loss occurred between 320 °C to 950 °C after the gas was switched to nitrogen. The final carbon yield was 9% to 14% of initial weight. Fifty-five percent of the weight loss was attributed to the removal of hydrogen and oxygen in cellulosic material according to the reaction formula (Wu et al., 2008). However, more weight loss was detected from the TGA analysis and was attributed to carbon loss as CO and CO<sub>2</sub> during depolymerization and scission. It has been shown that the heating rate plays an important role in the char yield during cellulose carbonization (Milosavljevic and Suuberg, 1995).

The effect of the heating rate during the rapid mass loss processes (230 °C to 320 °C) on the char yield at 800 °C was also compared. The char yield increased significantly when the heating rate increased from 0.2 °C/min to 2 °C/min. At this latter heating rate, the char yield was 14 %. When heating rates were set faster than 2 °C/min, a slight trend toward lower char yield was observed. Compared to macroscopic fibers such as cotton, the microfibril cellulose began to decompose at a significantly lower temperature due to the larger surface area that was exposed to heat, dramatically cutting the energy input and allowing a lower heating temperature during carbonization for making the porous material (Gaspar et al., 2014).

### **3.2 Structure of MFC aerogel and carbon aerogel**

The structure of an absorbent material has a strong influence on its oil absorption capacity. In the most favorable conditions for aerogel preparation, the volume of carbon aerogel shrinks to 13% of that of MFC aerogel, while the weight of carbon aerogel drops to 6% of MFC aerogel. The bulk density of MFC aerogel is 0.025 g/cm<sup>3</sup>, decreasing to 0.010 g/cm<sup>3</sup> after carbonization. Skeletal density of MFC aerogel is 1.48 g/cm<sup>3</sup>; 1.4 g/cm<sup>3</sup> for carbon aerogel C-950; and 1.33 g/cm<sup>3</sup> for carbon aerogel C-700. Figure II-2 shows SEM images of MFC aerogel and carbon aerogel C-950. Both types of aerogel consist of a 3D network structure with interconnected microfibrils in which large spaces are present among the entangled fibers. Pore

sizes span a range between tens of nanometers and tens of micrometers. The morphology of MFC aerogel and carbon aerogel differ in that the fiber diameter of MFC aerogel is from 50 nm to 200 nm, and that of carbon aerogel is from 10 nm to 20 nm. Cellulose fibrils shrink considerably during carbonization because of the removal of non-carbon elements. The Kymene<sup>TM</sup> resin (PEA) starts to crosslink in the process of heating and acts on the points where fibers intersect to facilitate the formation of a three-dimensional structure because the amino chlorohydrin and azetidinium chloride (ring) groups existent in PEA resin have the ability to react with carboxyl groups on the cellulose surface, which helps to bonding adjacent fibers (Figure II-3). FTIR spectra of MFC raw material and crosslinked MFC aerogel are presented in Figure II-4. The ratio of peak intensity at 1650 cm<sup>-1</sup> (amide C=O stretch) to the peak intensity at 1043 cm<sup>-1</sup> (C-O stretch) increases dramatically after crosslinking, indicating the reaction between cellulose and the crosslinker (Zhang et al., 2012). TEM images of Sample C-950 show well-developed graphitic-like domains composed of about 20 parallel fringes as well as numerous uncorrelated fragments. The (002) fringes originate from the graphene sheets and extend perpendicularly to the image plane. Figure II-2f shows the electron diffraction pattern of Sample C-950 corresponding to image 2e, which confirms the presence of graphitic stacks. The graphitic structure was barely observed, however, in Sample C-700.

### 3.3 Surface area and porosity of carbon aerogels

According to equation (2), the porosity was calculated at 97.8% for the MFC aerogel and 99% for the two carbon aerogels. Nitrogen adsorption at 77 K detects micropores, comparable with the diameter of N<sub>2</sub> molecules, and mesopores where capillary condensation N<sub>2</sub> occurs. The larger micrometer-size voids in the aerogel structure (Figure II-2d) were not measured by this method, so the porosity information obtained from gas adsorption on these aerogels was limited to micropores (< 20 Å) and mesopores (20 Å to 500 Å). On these very open materials, multilayer adsorption of nitrogen occurs freely on the external surface of fibers and ligaments visible in the SEM images. The BET equation provides a reliable measurement of the total surface area in these materials (Brunauer et al., 1938).

Adsorption isotherms of nitrogen at 77 K on Samples C-700 and C-950 are shown in Figure II-5. Both samples yielded IUPAC Type II isotherms at 77 K, indicating that a mixture of



micropores and open surface is present in the carbon aerogel on which unrestricted monolayer-multilayer adsorption occurs (Ryu et al., 1999). Sharp inflection points are present at a low relative pressure of about 0.1, showing the transition from micropore filling to multilayer adsorption. The slow isotherm rise that follows next indicates multilayer adsorption of nitrogen on the exposed surface of the 3D fibrous network in carbon aerogels (Figure II-2d). This exposed surface makes the major contribution to oil absorption, rather than micropores or mesopores.

Sample C-700 showed a higher N<sub>2</sub> uptake than Sample C-950 did. The BET surface area of carbon aerogel C-700 (521 m<sup>2</sup>/g in Table II-2) was in range with other reported results (Kipling et al., 1964). However, the surface area of C-950 was found to be only 145 m<sup>2</sup>/g, lower than the 449 m<sup>2</sup>/g reported for a carbon prepared from pure cellulose at a peak temperature of 1000°C (Xie et al., 2009). This is attributable to the formation of graphite-like domains observed in the HR-TEM images of Sample C-950. It is reasonable to assume that more carbon sheets were tightly stacked in Sample C-950 than in Sample C-700, which would eliminate the voids among the formed graphene sheets and would reduce the total surface area. The difference in BET surface area values explains why Sample C-700 had higher oil absorption capacity compared to Sample C-950 for the same oil type. Figure II-5(b) shows the distribution of internal surface area vs. pore sizes for the two carbon aerogel samples, obtained by the NLDFT method. A majority of the surface area measured by nitrogen adsorption was contained in micropores (< 20 Å) and lower mesopores (20 to 200 Å). The same information was obtained from Figures II-5c and d, where the differential and cumulative pore size distributions were calculated by the NLDFT method. The total pore volume for pores up to 300 Å was larger for Sample C-700 (0.55 cm<sup>3</sup>/g) than for Sample C-950 (0.28 cm<sup>3</sup>/g), in agreement with the values of the BET surface area. Micropores (< 2 nm) were seen to represent a small fraction of the pore volume measured by gas adsorption (30 % in C-700; 9 % in C-950). Supermicropores (0.7 nm to 2 nm) were present on both samples, although in an extremely low amount, on Sample C-950 and in larger proportions on Sample C-700. More significant was the fraction of lower mesopores (up to about 20 nm) on both samples. The slope of isotherms at P/P<sub>0</sub> > 0.1 (Figure II-5a) represents the filling of mesopores.

### 3.4 Hydrophobic properties of carbon aerogel surface

The wetting properties of MFC aerogel and carbon aerogel were further investigated by static contact angle measurement. When water droplets were dropped on the MFC aerogel surface, the droplets spread out and were taken up immediately by the porous sponge, indicating a low contact angle. This hydrophilic character is associated with the presence of hydrophilic surface groups on the MFC aerogel surface. FTIR spectra of MFC aerogel showed dominant peaks at 1043, 3392, 1640, and 1160  $\text{cm}^{-1}$ , which were identified as C-O, -OH, C=O, C-O-C, respectively (Figure II-4). Pyrolysis changed the water behavior uptake of the carbonized aerogels significantly, making them strongly hydrophobic. Figure II-6 shows the behavior of water droplets on the surface of carbonized aerogel C-950 and the evolution of the contact angle. Despite a slight decrease with time (from 149° to 144°), the contact angle at the water/carbonized aerogel boundary remained very high, indicating a strong hydrophobic character. FTIR analysis confirmed the absence of hydrophilic groups; the remaining FTIR bands still visibly (Figure II-4) correspond to aromatic carbon bonds, which cause the hydrophobic characteristic. Interestingly, the FTIR spectrum of Sample C-700 shows peaks at 1600 and 1100  $\text{cm}^{-1}$  corresponding to the C=C and C-N stretch. Nitrogen was seen to be present in large amounts in the PEA resin as indicated by the elemental analysis, amounting to about 2 wt % in MFC aerogel and increasing to about 3.3% in both carbonized aerogel samples. Carbonization causes a strong increase in carbon content and a drop in hydrogen content (Table II-3). The experimental characterization reported above demonstrates the water-repellent and oleophilic properties of carbon aerogel. Thus, this ultralight, high porous material is able to effectively clean oil spills by selectively absorbing oil floating on water, a finding that is of great significance for practical applications.

### 3.5 Oil absorption

An oil absorption test using four representative oils was conducted for the purpose of verifying the oil sorption kinetics of carbon aerogels and their oil storage capacity. Figures II-7 (a), (b) and (c), sequential photographs, show that a piece of carbon absorbs blue engine oil in a few seconds. The sorption kinetic action is presented in Figures II-8 (a) - (d), where the oil

absorbency was plotted against sorption time. These results provide two important pieces of information. First, visible observation showed that the carbon aerogel was rapidly wetted at the very beginning of absorption. Data collected at initial absorption times exhibited a very high sorption rate, indicating the capillary rise. The oil then penetrated into the pores by capillary action. Secondly, diffusion was observed later in the sorption curve, as shown by a slow step during the oil absorption process. On all four types of oils, Sample C-700 demonstrated higher oil absorption capacity than did Sample C-950. The absorption capacities, normalized by dividing the weight gain into oil density, are shown in Figure II-8 (e). Sample C-700 had the highest normalized saturated oil absorption capacity (87 times its own weight) for paraffin oil. It takes longer for carbon aerogel to reach one-half the saturated sorption capacity with high viscosity oil. It is evident that the same oil diffused faster on Sample C-700 than on Sample C-950. An important implication of these findings is that lower-temperature pyrolysis of MFC aerogel is to be preferred for preparation of oil absorbent materials with higher absorption capacity.

The sorption kinetics of carbon aerogel was analyzed based on the following pseudo-second order model and equation (Bastani et al., 2006, Gui et al., 2011):

$$\frac{1}{(Q_s - Q_t)} = \frac{1}{Q_s} + kt \quad (4)$$

where  $Q_s$  is saturated oil absorption,  $Q_t$  is the oil absorbed at time  $t$  and  $k$  is the kinetic rate constant. The red lines plotted in Figure II-8 show the fitting results of four different oils, and Table II-2 summarizes the fitting parameters. The predicted results correlated well to the experimental data.

The analysis of porosity and SEM images provides information on the structure of carbon aerogel. Capillary condensation and excess adsorption are believed to dominate the carbon aerogels' properties during absorption. The structure and the volume of carbon aerogel dominate the oil storage amount, while the number of capillaries dominates the absorption rate. Given its ultra-low density and its high open porosity, carbon aerogel has a significantly higher oil absorbency  $Q_s$  when compared to other oil absorbents such as  $\text{TiO}_2$ /nanocellulose aerogel ( $Q_s=27$  for paraffin), winter melon carbon aerogel ( $Q_s=26$  for diesel), cotton towel ( $Q_s=5$  for diesel), cellulase modified corn stalk ( $Q_s=16.65$  for diesel), PU sponge ( $Q_s=42$  for diesel),

graphite/isobutylene-isoprene aerogel ( $Q_s=22$  for diesel) and swellable porous PDMS ( $Q_s=12$  for diesel) etc. (Zhang et al., 2013, Choi et al., 2011, Peng et al., 2013, Li et al., 2014). The time for carbon aerogel to reach one-half of the saturated sorption capacity, denoted as  $t_h$ , was used to characterize the absorption rate. The  $t_h$  value for diesel absorption ( $t_h=0.6$  s) was the smallest among the four different oils, indicating a very fast absorption rate. Because oil density and viscosity play important roles in the absorption capacity of carbon aerogel, the normalized oil absorption capacity of carbon aerogel for paraffin oil ranks the highest among the four kinds of oils. The oil density also contributes to the saturated absorption capacity in carbon aerogels with same pore size distribution and 3D network structure. Despite the fact that sample C-950 has low BET surface area ( $145 \text{ m}^2/\text{g}$ ), it still achieved much higher absorption capacity compared to other absorbents. This indicates that macropores and the open pore structure make the carbon aerogel a very efficient oil absorbent. The large pores created by the 3D network structure should provide better accessibility for oil or organic solvent molecules. On the contrary, on absorbent materials that are mainly dominated by micropores and mesopores, highly viscous oil is potentially retarded by viscous drag, which prevents the oil from permeating when being absorbed. Most organic solvents and oils have small surface free tension, usually in the range of 20 to 30  $\text{mJ}/\text{m}^2$  (pump oil  $28.21 \text{ mJ}/\text{m}^2$ , diesel oil  $24.14 \text{ mJ}/\text{m}^2$ ). However, carbon fibers' surface free energy is 40 to 50  $\text{mJ}/\text{m}^2$ , which is close to that of oil but smaller than the surface free tension of water ( $72.8 \text{ mJ}/\text{m}^2$ ) (Harkins and Brown, 1919). This makes it easy for oil to infiltrate the pores of carbon aerogel. Thus, the water-repelling and oil-wetting properties qualify carbon aerogel as a perfect absorbent candidate for oil-water separation.

To verify the reusability of carbon aerogel for oil removal, the oil sorption experiments were repeated after the oil-soaked samples were thoroughly cleaned in ethanol and dried. As Figure II-8 (f) shows, the carbon aerogel was found to retain the same oil absorption capacity after ten absorption/desorption cycles.

#### 4. Conclusions

This paper reports on the synthesis and properties of a sponge-like nanocellulose-based carbon aerogel. This material is useful as a highly porous oil absorbent (99% porosity) with ultralight density ( $0.01 \text{ g}/\text{cm}^3$ ), hydrophobic properties ( $149^\circ$  static contact angle), fast

absorption rate, and multiple reusability. The carbon aerogel material was obtained through heat treatment of cellulose microfibril aerogel. The heating rate during the rapid mass loss process in the carbonization stage was optimized to 2°C/min to achieve high carbon yield. The structure-adsorption properties relationships of carbon aerogel were demonstrated. Carbon aerogel heat-treated at 700°C was found to possess higher oil absorption capacity of various types of oils, correlating with its higher BET surface area (521 m<sup>2</sup>/g), compared to the carbon aerogel heat-treated at 950 °C (145 m<sup>2</sup>/g). The factor mainly responsible for the high oil-absorption capacity is the 3D network structure formed by the entanglement of carbonized cellulose fibrils and the large surface energy of carbonized fibers, and micropores enhance the absorption capacity to some extent. These unique properties of carbon aerogel, along with the advantages of using a natural, renewable, low-cost, and sustainable material, recommend carbon aerogel treated in this way for a wide range of oil-spill cleanup applications.

## Appendix II

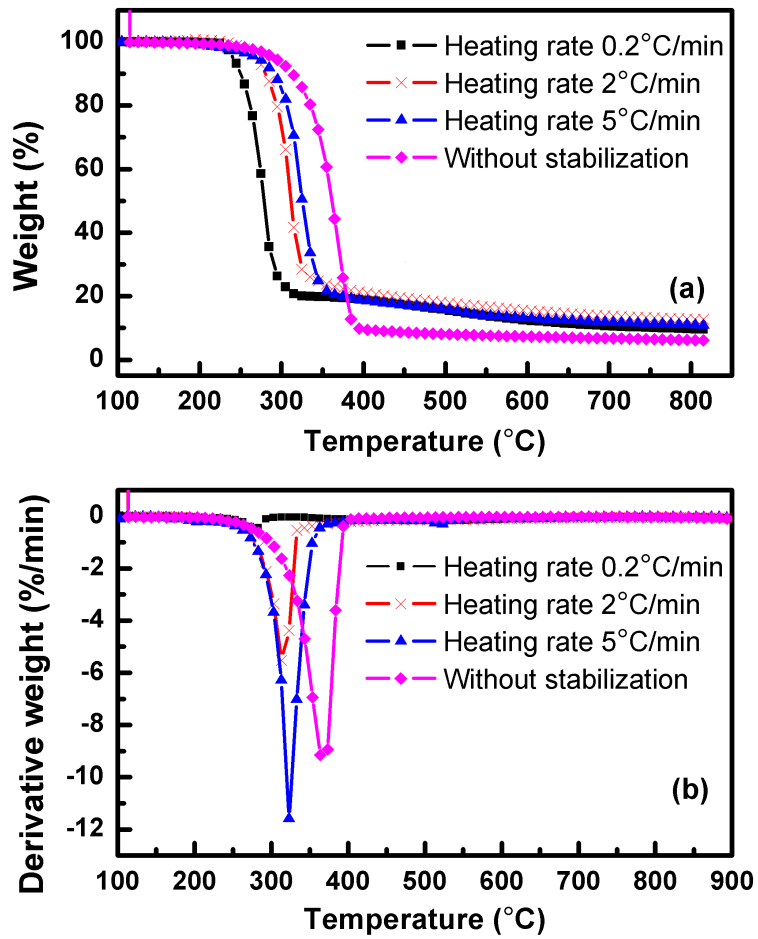


**Figure II- 1** Thermogravimetric analysis (TGA) curves showing the effect of heating rate during the temperature rising from 230°C to 320 °C on carbon residual yield at 800°C (a) TGA curves, (b) DTG curves.

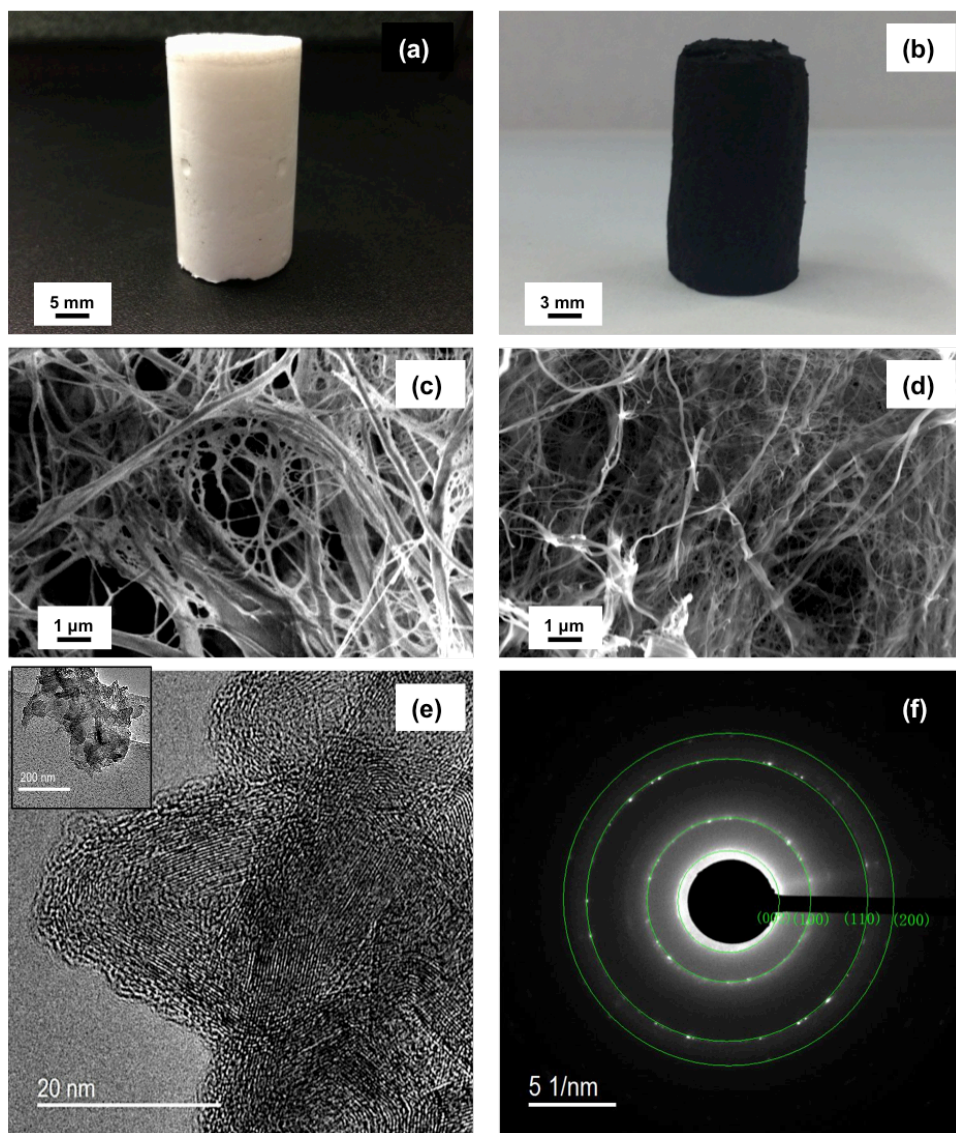


**Figure II- 2** Photographs of (a) microfibril cellulose aerogel, and (b) carbon aerogel (C-950); SEM images of (c) microfibril cellulose aerogel, and (d) carbon aerogel (C-950); TEM images of (e) graphitic domains in the structure of carbon aerogel C-950 and (f) diffraction pattern from the same carbon aerogel.



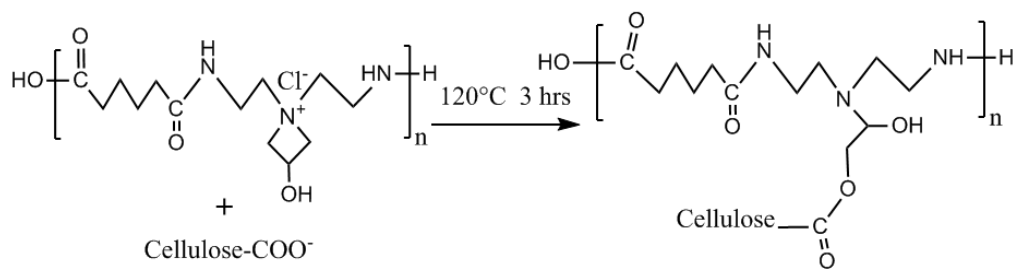


**Figure II- 3** The formation of ester bond between Kymene<sup>TM</sup> crosslinker and cellulose carboxyl groups.

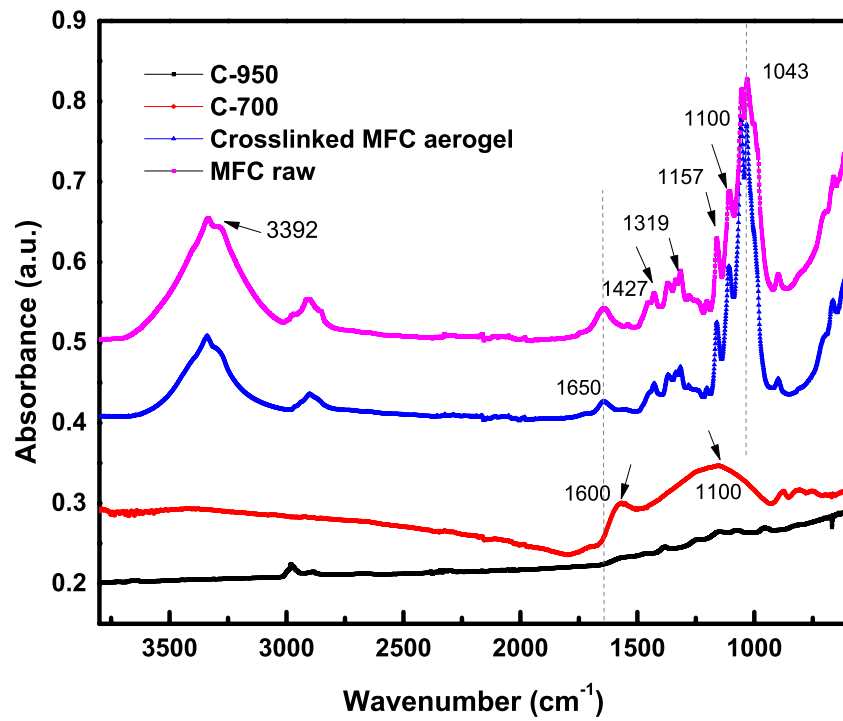
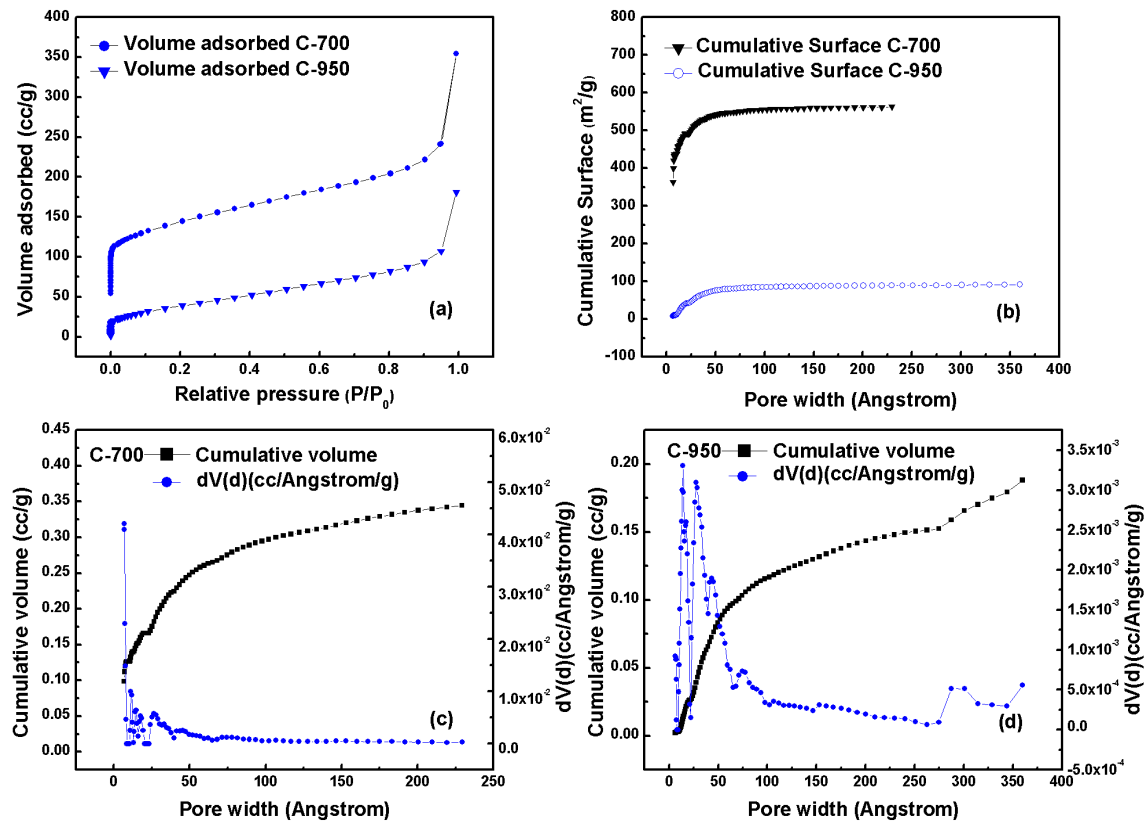


Figure II- 4 FTIR spectra of MFC aerogel and carbon aerogels.



**Figure II- 5** (a) Adsorption isotherms of nitrogen on carbon aerogel heat-treated at 700°C and 950°C; (b) cumulative surface distribution of carbon aerogels and (c), (d) differential and cumulative pore size distributions determined by NLDFT method for Samples C-700 (c) C-950 (d).

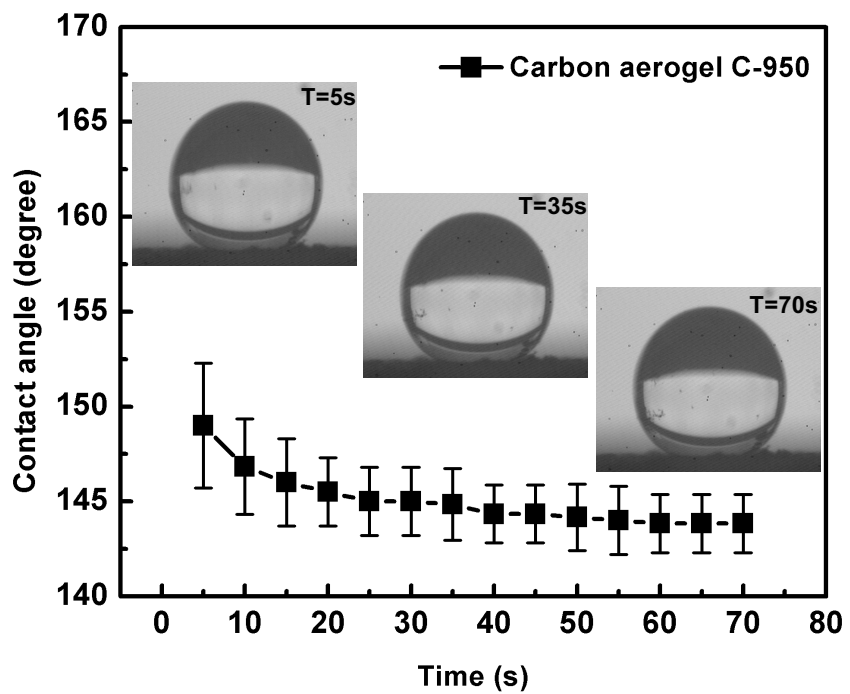
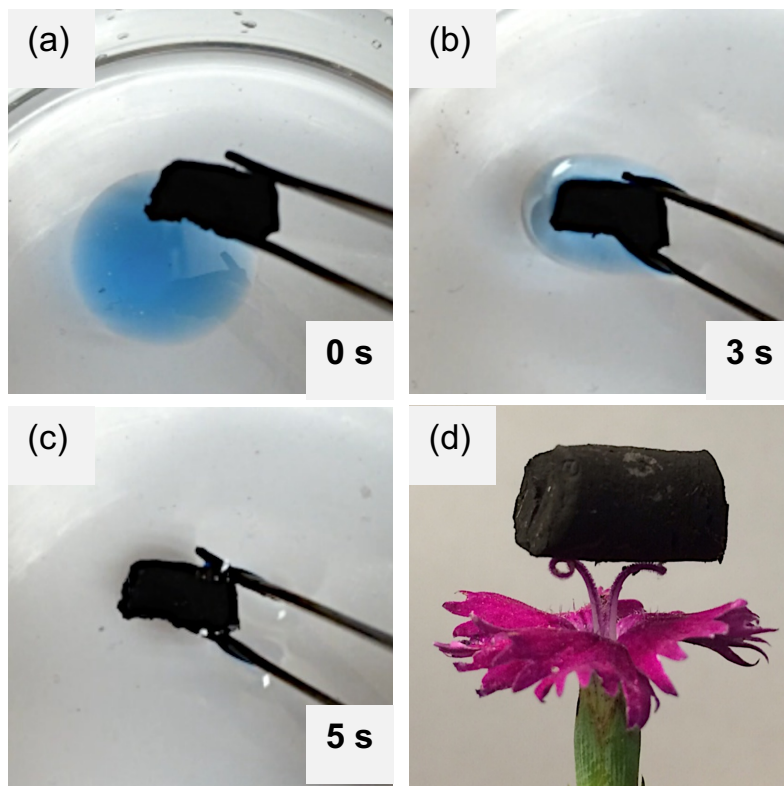
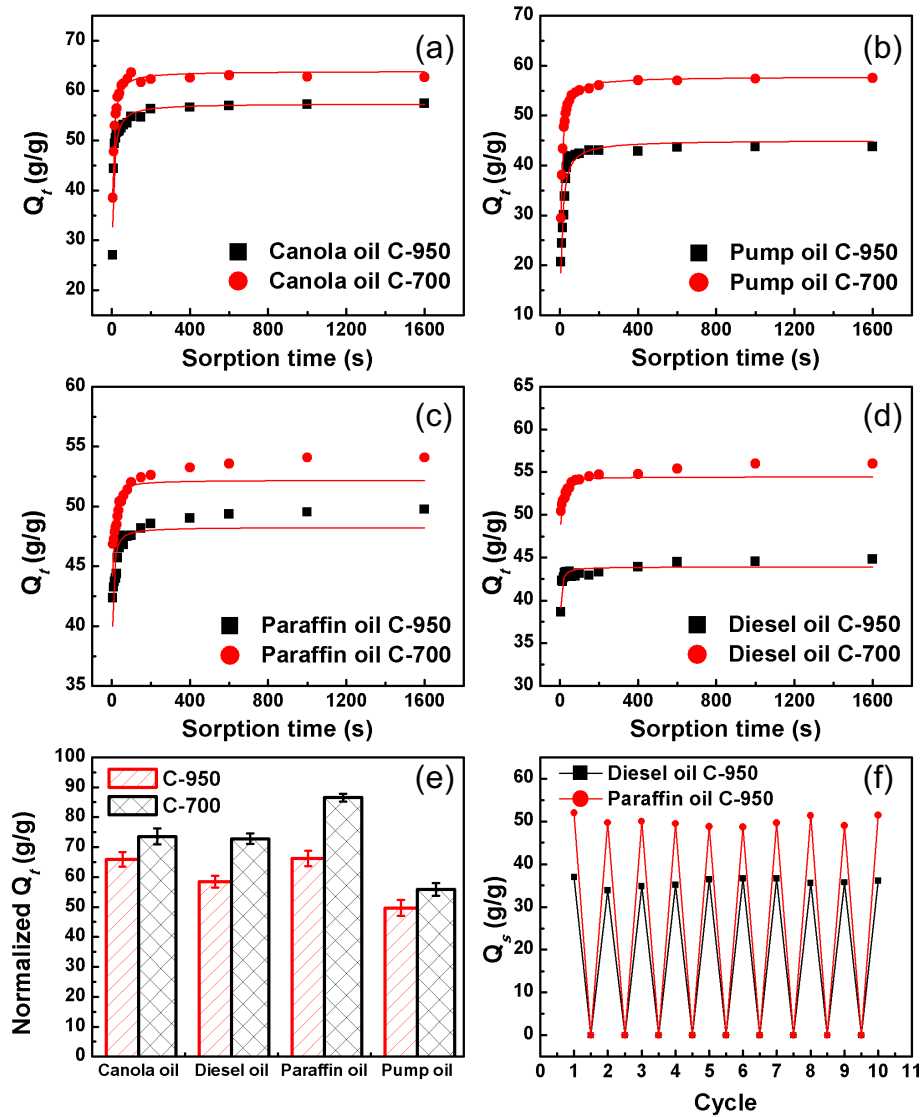


Figure II- 6 Carbon aerogel wetting characterization by static contact angle analysis.



**Figure II- 7** (a), (b) and (c) Removal of engine oil from the water surface using nanocellulose carbon aerogel (d) Ultralight carbon aerogel sitting on a flower.



**Figure II- 8** Sorption kinetics of different oils absorbed by carbonized MFC aerogel: (a) canola oil, (b) pump oil, (c) diesel oil, (d) paraffin oil, (e) normalized saturated sorption capacities of different oils by oil density, (f) absorption reusability of carbon aerogel.

**Table II- 1** Onset temperature, degradation temperature and weight loss of MFC aerogel under different heating rates

Heating rate (°C/min)	Onset temperature (°C)	Degradation temperature (°C)	Weight loss (%)
0.2	256.28	279.77	90.36
2	293.26	215.29	86.02
5	306.12	323.02	89.04
Without stabilization treatment	334.63	368.65	93.85

**Table II- 2** Carbon aerogel's properties and fitting parameters of the sorption kinetics

Sample ID	Porosity (%)	Sponge density (g/cm <sup>3</sup> )		BET surface area (m <sup>2</sup> /g)		
C-950	99	0.01		145		
	Pollutants	Pollutants density (g/cm <sup>3</sup> )	Viscosity (cST)	k (x10 <sup>-3</sup> s <sup>-1</sup> )	N-Q <sub>s</sub> (g/g)	t <sub>h</sub> (s)
	Canola oil	0.890	70	4.6	65.9	3.7
	Diesel oil	0.772	10	36.9	58.4	0.6
	Pump oil	0.888	250	3.08	50.0	7.2
Sample ID	Porosity (%)	Sponge density (g/cm <sup>3</sup> )		BET surface area (m <sup>2</sup> /g)		
C-700	99	0.01		521		
	Pollutants	Pollutants density (g/cm <sup>3</sup> )	Viscosity (cST)	k (x10 <sup>-3</sup> s <sup>-1</sup> )	N-Q <sub>s</sub> (g/g)	t <sub>h</sub> (s)
	Canola oil	0.890	70	4.9	73.6	3.2
	Diesel oil	0.772	10	32.4	72.8	0.6
	Pump oil	0.888	250	3.64	55.8	4.7

*Note: N-Q<sub>s</sub> is the normalized saturated sorption capacity in terms of oil density; t<sub>h</sub> is time when carbon aerogel reaches one-half of the saturated sorption capacity*



**Table II- 3** Elemental percentage of MFC aerogel as an average of 2 runs before and after carbonization

Sample	Weight (mg)	Average Weight (%)			
		C	N	H	O
MFC aerogel	2.1	43.55	2.15	6.26	48.04
C-700	2.1	81.59	3.30	1.62	13.49
C-950	2.3	84.78	3.39	0.88	10.95

## **CHAPTER III**

# **OPTIMIZATION OF CELLULOSE NANOFIBRILS CARBON AEROGEL FABRICATION USING RESPONSE SURFACE METHODOLOGY**

A version of this chapter was submitted to the *European Polymer Journal* on June 17<sup>th</sup>, 2015

Authors:

Y. Meng, S. Wang, T. M. Young

*Center for Renewable Carbon, Department of Forestry, Wildlife & Fisheries, University of Tennessee, Knoxville, TN, USA*

X. Wang

*Department of Materials Science & Engineering, Nanjing Forestry University, China*

Z. Wu

*Oak Ridge National Laboratory, Oak Ridge, TN, USA*

Y. Meng's primary contribution to this paper includes identifying the research objective, design and conduct of the experiments, process and interpretation of the data, drafting the paper.

Co-researchers' contributions are listed as follows:

X. Wang worked with Yujie to make aerogel and perform the oil absorption test.

Z. Wu worked with Yujie to conduct the experiment.

S. Wang provided research guideline, revised and reviewed the paper.

T. M. Young identified the research objective, worked with Yujie to analysis the data and revised the paper.

## **Abstract**

This research investigates the simultaneous effects of processing parameters for making carbon aerogel from cellulose nanofibrils (NFC). Variables such as peak temperature and heating rate at different levels are systematically investigated with the goal of parameter optimization using response surface methodology (RSM). A face-centered central composite design (CCF) was used to evaluate the feasible range of process conditions where the levels of peak temperature and heating rate were varied between 230 °C to 320 °C. Results indicate that the quadratic model developed for the response surface is feasible for the prediction of optimal parameters. Response surfaces were developed to explore the integrated and feasible operating space. Optimum conditions were: 250 °C of the peak temperature and 9.9 °C/min of the heating rate. The carbon aerogel achieved approximately 94 g/g of the normalized oil absorption capacity despite a weight reduction percentage of 75 %.

## 1. Introduction

Oil recovery from oil spills using absorbent materials has recently attracted extensive scientific and practical interest. Among numerous materials, absorbents from natural precursors are of the most interest. Despite the fact that conventional nature absorbent materials have been widely used for large-scale oil spill clean up, the hydrophilic nature will drastically hamper the oil absorption efficiency. As a result, new absorption materials with hydrophobic properties are of great interest. Examples include carbon foams, graphene aerogel, carbon nanotube aerogel, carbon fiber aerogel and carbon microbelts aerogel (Nagel et al., 2014, Gui et al., 2011, Hu et al., 2013, Li et al., 2010, Li et al., 2014, Upadhyayula et al., 2009, Wu et al., 2013c).

Nanocellulose is a promising new material not only because it is bio-based, sustainable, nontoxic, abundant, and renewable resource; but also given its unique intrinsic properties (Dong et al., 2013, Wu et al., 2013a, Wu et al., 2014). In particular, cellulose nanofibrils (NFC) consists of long, flexible fibers cleaved from the hierarchy of plant or wood cellulose by mechanical processes (Moon et al., 2011, Wang and Cheng, 2009, Cheng et al., 2007). Among their superior properties, their thermal stability is of great interest (Ansell, 2012). Since the development of the carbon structures from this potential green alternative, numerous promising applications have been exploited, ranging from electrochemical energy storage, hydrogen storage, to super capacitors etc. (Ding et al., 2013, He et al., 2014a, Wang et al., 2013). The mechanism and the structure-properties relationships of carbonaceous material have been systemically studied (Tang and Bacon, 1964a, Cagnon et al., 2009, Li et al., 2008). For cellulose material, the carbonization is mainly dominated by two reactions including degradation and depolymerization (Dumanli and Windle, 2012). In addition, heating temperature, and heating rate during carbonation have been demonstrated as key factors that influence the mechanical properties (Huang, 2009). However, the effect of these two parameters on the porous and adsorption properties is limited. Our previous study has successfully developed a super-light, hydrophobic carbon aerogel with highly oil absorption properties using microfibril cellulose as the raw material (Meng et al., 2014). We demonstrated a green synthesis approach involves freeze-drying and carbonization process to achieve 3D porous network structure and hydrophobic properties. We also noticed that low heating temperature helped improving the oil absorption capacity. On top of that, in order to

achieve maximum oil absorption capacity and increase the final carbon yield, research attention has been turned toward to two factors: namely ‘peak temperature’ and ‘heating rate’ during carbonization.

There are some disadvantages of studying the influence of the factor on the response one-factor at a time, e.g., it is time consuming involving many experiments and does not allow for the examination of interaction effects. Design of experiments (DOE) is a tool that allows for parameter optimization, especially in cases where many factors are involved and varied simultaneously. Response surface methodology (RSM) is an effective statistical tool used in studies including biochemical systems, biotechnology, and nanotechnology etc. (Montgomery, 2012). RSM allows for expanded inference; the study of interactions; and parameter optimization. Basically, RSM is a formal statistical technique that maximizes inference with the minimum number of experimental runs.

The research focus of this study was to estimate the effect of key factors on the response of oil absorption and weight reduction, and to determine the optimal values for processing carbon aerogel. This approach quantifies the relationship between NFC aerogel carbonization processing conditions and carbon aerogel’s physical properties. The RSM used two variables, ‘peak temperature’ and ‘heating rate’ on the oil absorption capacity and final weight reduction of carbon aerogel. In addition, the physical properties, internal morphology and thermal properties of carbon aerogel were investigated.

## **2. Material and methods**

### **2.1 Material**

Cellulose nanofibrils with a solid content of 5% were obtained from commercial sources (University of Maine, USA). Cross-linker Kymene™ resin was commercially available (Ashland Hercules Inc., USA).

## **2.2 Preparation of NFC aerogel and carbon aerogel**

A mixture of 1.5 wt % aqueous suspension of NFC and cross linker resin (5 wt % of dry NFC) was poured into open-ended copper pipes (1.5 inch in length and 0.81 inch in diameter) and sealed with aluminum foil. The samples were then placed into liquid nitrogen for one minute for rapidly freezing, following which the aluminum foil was removed and the samples were freeze-dried in a vacuum lyophilizer (Labconco, Inc., Kansas City, MO) at -51 °C for three days. Ultralight sponge-like aerogel was obtained. Samples were oven-heated at 120 °C for 3 hours to promote cross-linking in order to form a three-dimensional network. The aerogel samples were carbonized in nitrogen (20 ml/min) using a tube furnace (Thermo Scientific). The carbonization stage included: (1) heating the sample from room temperature to 180 °C at a rate of 10 °C/min in nitrogen; (2) increasing the temperature from 180 to 230 °C at a rate of 5 °C/min in nitrogen; and (3) increasing the temperature from 230 to 320 °C in nitrogen. Different heating rates ranging from 0.2 to 5 °C/min were applied in this step; and (4) increasing the temperature from 320 °C to peak temperatures of 400 °C, 700 °C and 1000 °C respectively at a rate of 5 °C/min in nitrogen and holding for 15 min. Samples were then cooled to room temperature.

## **2.3 Oil sorption experiments**

Oil absorption experiments were carried out using paraffin oil (BP PLC gas station). Carbon aerogel sponges were weighed first and immersed into oil. After the immersion, the sponge was taken out, drained for 30 seconds to wipe away the excess oil, and immediately transferred to a tarred pan. Sample was measured by weight and this process was repeated until carbon aerogels reached sorption saturation. The oil absorption capacity could be defined as the ratio between the weight of absorbed carbon aerogel and the weight of dried carbon aerogel.

## **2.4 Characterization of NFC aerogel and carbon aerogel**

The inner structures of NFC aerogel and carbon aerogel were imaged using scanning electron microscopy (SEM, Zeiss Auriga SEM/FIB crossbeam workstation). NFC aerogel was coated with a thin layer of gold to provide conductivity and to protect the sample from electron

beam damage. The ultrastructure of the carbon aerogel was characterized by transmission electron microscopy (TEM, Zeiss Libra 200 MC). Carbonized aerogel was ground into powder and dispersed into distilled water. TEM samples were prepared by depositing suspension drops (0.001 % w/v in water) on amorphous lacey carbon-coated electron microscope grids and were then allowed to dry. The TEM was operated at a 200 kV accelerating voltage. Thermal stability and carbonization yield were determined using thermogravimetric analyzers (TGA; Perkin–Elmer 7 series; Perkin–Elmer Cetus Instruments, Norwalk, CT). The heating program was set up exactly the same to mimic the carbonization process.

## 2.5 Experimental design

A face-centered central composite design (CCF), where the red stars are at the center of each face of the factorial space, was employed for the designed experiment of this research. Figure III-1 illustrates the diagram of CCF designs for two factors. The CCF provides predictions over the entire design space. Effects of two factors, namely ‘peak temperature’ and ‘heating rate’ on two responses of oil absorption and weight reduction respectively were evaluated. There were three levels for each factor as shown in Table III-1. The levels were determined based on previous knowledge and screening experiments.

The number of experiments required for the  $2^2$  full factorial CCF experiments were calculated according to the equation ( $N=2^k+2k+nc$ ), where  $k$  represents the number of factors,  $2^k$  is the number of factorial points,  $2k$  stands for the axial points (star points) on the face, while  $nc$  means the number of replicates at the center point, in this case  $n=2$ . The design had a total of 20 runs including 8 factorial points, 8 axial points (star points) and 4 replicates at the center points.

## 2.6 Statistical analysis

The relationship between the variables and each response  $Y$  could be described as a second-degree polynomial quadratic equation:

$$Y = b_0 + \sum_{i=1}^k b_i x_i + \sum_{i=1}^k b_{ii} x_i^2 + \sum_{i=1, j=i+1}^k b_{ij} x_i x_j + \varepsilon \quad (1)$$



where  $b_0$  is the constant value,  $b_i$  is the regression coefficients of the individual linear effect,  $b_{ii}$  is the quadratic effect and  $b_{ij}$  is the interaction between the variables;  $k$  is the number of factors studied ( $k=2$  in this case).

Statistical analysis including ANOVA and prediction of regression coefficients, response surface and contour plots were developed in JMP software (version10, SAS Institute; Cary, NC, USA). The coefficients with small  $p$ -value less than 0.05 were considered to be statistically significant effect.

### **3. Results and discussion**

#### **3.1 Observation of structure and physical properties**

The inner structure of both NFC aerogel and carbon aerogel heat-treated at 1000 °C was imaged using scanning electron microscopy (SEM), and the ultrastructure of carbon aerogel was investigated using TEM (Figure III-2). Both aerogel and carbon aerogel were composed of a three-dimensional network structure with interconnected microfibrils. It is the 3D porous network structure that makes the derived carbon aerogel possessing an ultralow density. Effects of heating temperature and heating rate on physical properties of NFC aerogel and carbon aerogel were evaluated and compared. From the bright-field TEM image in Figure III-2 (c) and line profile (d), it is clearly and easily observed that carbon aerogel heat-treated at 1000°C is mainly composed of stacks of ribbon-like graphitic layers with a calculated spacing of 0.368 nm. The graphite ribbons are orientated randomly and tangled in a complicated manner. In the contrast, barely and no graphite structure were observed in carbon aerogel heat-treated at 700 °C and 400 °C, respectively. Results also showed that the bulk density of NFC aerogel was 0.02 g/cm<sup>3</sup>, decreasing to 0.01 g/cm<sup>3</sup> after carbonization at various temperatures. Figure III-2 (e) presented an image of NFC aerogel sitting on the flower visually indicated the ultralight properties. Figure III-2 (f) showed the photograph of water droplet supported on the carbon aerogel, indicating its hydrophobicity. It was believed that hydrophilic functional groups such as C=O, C-O, -OH and C-O-C existed in NFC aerogel could be largely removed during carbonization, leading to the reverse of wetting properties(Meng et al., 2014).

### 3.2 Factor optimization by response surface methodology

The central composite design and the observed dependent variables data are summarized in Table III-2. The variable coded as ‘-’ and ‘+’ represents the ‘low’ and ‘high’ levels of the studied variables, ‘0’ represents the center point of the design, letters ‘a’ and ‘A’ represent the axial points of the design. The oil absorption capacity ranged from 71.94 to 94.18 g/g at design point of “11” and “2”, respectively. The Weight reduction ranged from 66.12 to 87.89%, at design points of “2” and “17”, respectively. Generally, cellulose carbonization is a complex process that usually involves dehydration and depolymerization (Dumanli and Windle, 2012). Ideally, the carbon yield of NFC is 44.4 % according to the molecular stoichiometry  $(C_6H_{10}O_5)_n$ . However, the depolymerization of the macromolecular chains during carbonization usually happens with the formation of carbon monoxide, and carbon dioxide, aldehydes, organic acid, and tars, which takes away more carbons, leading to a low carbon yield. It has been shown that heating rate plays an important role on the char yield during carbonization (Milosavljevic and Suuberg, 1995). A fast heating rate can create small volatile fragments in cellulose structure, leading to a major mass loss when increasing the temperature. Usually, a slow heating rate of a few °C /min is suggested in order to increase carbon yield. The cellulose structure will experience a series of changes when heating temperature is increased. The structure of the carbon residual has a tendency to become well-ordered during the heat treatment when temperatures range from 400 °C to 900 °C. Graphitization usually starts when the heat treatment exceeds 900 °C. Based on previous studies on cellulose carbonization, the heating temperature is believed to be an important factor that affects carbon yield and may also has influence on the oil absorption capacity (Dumanli and Windle, 2012).

### 3.3 The statistical analysis results of the optimization experimentation for two variables

The goodness of fit analysis was employed to estimate how well the statistical models describe the experimental data. The actual by predicted plot is shown in Figure III-3, where there was a strong correlation between predicted and actual oil absorption capacities ( $R^2 = 0.88$ ). Relatively low  $R^2 = 0.6$  was observed for response of carbon aerogel weight reduction. The

observed results demonstrated that both responses of oil absorption capacity and weight reduction were affected by experiment factors.

The response model for oil absorption capacity is:

$$Y = 71.38 - 0.023(A - 700) - 0.43(B - 5.1) + 10^{-3}(A - 700)(B - 5.1) + 10^{-4}(A - 700)^2 + 0.15(B - 5.1)^2 \quad (2)$$

where  $Y$  was the response variable of normalized oil absorption capacity,  $A$  and  $B$  were the 'peak temperature' and 'heating rate,' respectively.

The response model for weight reduction is:

$$W = 93.39 + 0.0058(A - 700) + 0.86(B - 5.1) + 10^{-4}(A - 700)(B - 5.1) - 10^{-5}(A - 700)^2 - 0.4(B - 5.1)^2 \quad (3)$$

where  $W$  was the response variable of carbon aerogel weight reduction,  $A$  and  $B$  were the 'peak temperature' and 'heating rate', respectively.

The analysis of variance for the second-order regression equation was summarized in Table III-3. Fischer variance values (F value), denoted as the model mean square divided by the error mean square, were 21.06 and 4.23 for two models respectively. F values calculated from ANOVA regression were compared with critical F value, which is  $F_{0.05, 5, 14} = 2.96$  for both models, where 0.05 is the false-rejection probability, 5 is the degree of freedom of regression and 14 is the degree of freedom of residual error. The F value for model of normalized oil absorption capacity is 10 times greater than the critical F value and suggesting a statistical significance. However, the F value for model of weight reduction is greater than critical F value but less than 3-5 times greater, indicating a fairly low significance of model (Silva et al., 1999). The significance of each coefficient was evaluated by individual p value. The lower the p value, more significant of the variable. In the model for normalized oil absorption capacity, regression analysis revealed that the liner model terms, which are peak temperature, heating rate, and the quadratic model terms peak tem<sup>2</sup> made important contribution to the whole model with p values smaller than 0.05. The order of the terms regarding to the significant were: peak temperature (p<0.0001), peak tem<sup>2</sup> (p=0.0005), heating rate (p=0.0245). Carbon aerogel's volume is associated with oil absorption capacity. The volume were estimated to be 3.7 mm<sup>3</sup>, 2.16 mm<sup>3</sup> and 2.51 mm<sup>3</sup> corresponding to carbon aerogel heat-treated at 400 °C, 700 °C and 1000 °C, respectively. It seems volume shrinkage is small at low heating temperature while large at high

temperature. Similar result was also reported by Tang et al, that a plot was drawn describing the shrinkage percentage as a function of heating temperature (Tang and Bacon, 1964a).

Similarly, in the model for weight reduction, regression analysis revealed that the liner model term, heating rate and the quadratic model terms, peak tem<sup>2</sup> and heating rate<sup>2</sup> were significant with p values smaller than 0.05. The order of the terms regarding to the significant were: heating rate (p=0.0052), heating rate<sup>2</sup> (p=0.0184), peak tem<sup>2</sup> (p=0.0489). There was no significant interaction parameter contribute to the model given high p values shown in Table III-3. Carbonization temperature exhibits a negative effect on the char yield, consistent with the tendency found by previous studies available in the literature (Cagnon et al., 2009). The carbon yield is apparently sensitive to the heating rate, provided by the fact that slowing heating rate dramatically increase the carbon yield in early research (Brunner and Roberts, 1980). The Estimated regression coefficients for normalized oil absorption capacity and weight reduction were summarized in Table III-4.

### **3.4 Optimization of normalized oil absorption capacity and weight reduction of carbon aerogel**

The response surfaces of the interaction effects by the combination of two test variables are plotted to define the optimal processing conditions (Figure III-4). The heating rate and peak temperature have a negative impact on the normalized oil absorption capacity. The low heating temperature tended to lead to an increase of normalized oil absorption capacity. The response surface revealed that maximum oil absorption capacity achieved to 91.57 (g/g) at peak temperature of 400 °C with heating rate of 0.2 °C/min. A possible explanation of the phenomenon is that low pyrolysis temperature and low heating rate could results to large sample volume. We compared the carbon aerogel volume processed under three temperatures and found out that 400 °C heat-treated sample exhibits larger volume. Research on cellulose carbonization has proved and claimed that dehydration was the dominant reaction under low heating temperature (Dumanli and Windle, 2012). The elimination of hydroxyl groups induced double bonds, conjugated double bonds, which helped to maintain the cellulose structure more stable and less accessible to thermal cleavage. Heating the aerogel up to 400 °C only made the sample experiencing the early stage of carbonization, where thermal cleavage and scission were taken

place. The volume of the sample was fairly maintained at such low temperature. With the increasing of the heating temperature, more well ordered stacking graphene sheets were formed through re-polymerization with the releasing the gases and loose of non-carbon element, resulting to a condensed and close packed aromatic structure, consequently the volume shrinkage (Dumanli and Windle, 2012). Our previous research has demonstrated that macropores and the open pore structure make the carbon aerogel to be efficient as oil absorbent (Meng et al., 2014). Larger volume would provide more open voids and drastically increase the oil absorption capacity.

The weight reduction of carbon aerogel affected by combination of peak temperature and heating rate was plotted. Contour plot was generated by the predictive model and showed in Figure III-4 (d). The interaction effect is obvious on the response. An increase of heating temperature with heating rate up to the optimum point increased the weight reduction to its maximum number, while further increase in heating temperature with heating rate reversed the trend. In fact, the decrease of weight reduction on the contour plot is achieved by decreases in heating temperature below 700 °C or increasing in heating temperature above 700 °C, and increases in heating rate above 6 °C /min or decreases in heating rate below 6 °C /min. Again, the explanation for this is that the formed intermediates oxidization components have the tendency to be taken away in the form of H<sub>2</sub>O, CO, and CO<sub>2</sub>, when increasing the temperature to 700°C or 1000°C. A lower weight reduction is expected. The contour plot is used to find the feasible region for optimized process. Each contour with number marked on stands for a particular height of the corresponding response surface. It can be seen in Figure III-4 that at a low heating temperature with heating rate less than 6 °C /min, decreasing heating rate reduced the weight reduction of carbon aerogel. On the other hand, when heating rate was over 6 °C /min, increasing heating rate reduced the weight reduction. A fast heating rate, for example over 10 °C /min, will cause “thermal inertia” effect, which results to less reaction time to trigger decomposition.

The optimization prediction plots showed in Figure III-5 (A) refers to a typical optimum conditions for carbon aerogel: the peak temperature was 300 °C and heating rate was 9.0 °C/min, with the predicted response: normalized oil absorption capacity=90.3 g/g and weight reduction=80.4 %. The overall desirability (D=0.63), defined as the geometric mean of the

desirability measures, was reported to indicate the most desirable conditions. However, heating rate as slow as 0.2 °C/min shown on prediction profiler is not preferred from the viewpoint of energy reduction, despite of fact that the carbon aerogel exhibits low weight reduction and high oil absorption capacity under the condition. The overlaid contour plot was shown in Figure III-5 (b) with red contours revealing the weight reduction and blue ones revealing oil absorption capacity. It is useful to visually identify the feasible variables for multiple responses. Area highlighted by green dash lines mapped out in overlaid contour plots instructed the operation levels for the feasible region for desired response in reality, in this case, a relatively high oil absorption capacity and low weight reduction. In reality, heating temperature in the range of 300°C to 400°C is acceptable according to the previous study on carbonization of cellulose. Heating temperature over 300°C is necessary to ensure thermal scission and removal of none carbon element in form of H<sub>2</sub>O, CO and CH. In addition, heating rate in the range of 2 °C/min to 10 °C/min is more acceptable in accordance with low energy input and high efficiency. In this particular case, the area on the left middle highlighted by green dash line is more preferred because working on this region will dramatically reduce the operation time.

### **3.5 Thermal stability analysis**

To explain the discrepancy of oil absorption capacity and weight reduction from carbon aerogel, carbonization process was further investigated by TGA analysis. Figure III-6 illustrated the relationship between temperature and weight / derivative weight percentage of carbon aerogel. The curve shape is consistent with the TGA analysis performed on cellulose (Milosavljevic and Suuberg, 1995). One should notice that a rapid weight loss step occurs in the range of 230 °C to 320 °C for NFC aerogel. The extrapolated onset temperatures, denoted as the temperature at which the weight loss begins, of carbon aerogel were estimated to be 259 °C, 303 °C and 309 °C respectively corresponding to the heating rate of 0.2 °C/min, 2 °C/min and 10 °C/min. When performing carbonization on aerogel sample at low temperature, such as below 400 °C, carbon yield of CNF carbonized with low heating rate is significantly increased compared to that of high heating rates. The effect of heating rate during rapid mass loss (230 to 320°C) process on the char yield at 1000 °C was compared. The trends highlighted in the insert of Figure III-6 (a) show that heating rate has a positive effect on the residual carbon yield. Char

yield of carbonized aerogel exhibit highest number of 12.6 % with heating rate of 10 °C/min, while this number decrease with the decrease of heating rate. The degradation temperatures of NFC aerogel are calculated to appear at 302.3 °C when samples were heat-treated at low heating rate and appear at 351 to 354 °C when samples were heat-treated at high heating rate. Apparently, for NFC sample with heating rate of 0.2 °C/min, maxima in the rate of mass change occurred at 302 °C and 360 °C, however, their peak intensities are the lowest among all other curves. Decomposition is triggered by temperature and started earlier with low heating rate. Thermal cleavage and thermal scission mainly occur in the temperature range of 240 to 400 °C, whereby heating rate was various. Low heating rate could provide sufficient reaction time to allow the heat dissipating into material, thus leading to more loss of carbon atom in forms of CO and CO<sub>2</sub>. In the contrast, high heating rate caused by temperature overshoot has a great potential to lead to “thermal inertia” effect, consequently shift the onset and degradation temperatures to the right side.

#### **4. Conclusion**

In summary, this research investigated the carbonization process of aerogel derived from cellulose nanofibrils. We demonstrated that there exist the linkage between carbonization operating process variables (peak temperature and heating temperature) and the carbon aerogel performance (normalized oil absorption capacity, weight reduction). The carbon aerogel making process was successfully optimized by adopting a statistical strategy of response surface methodology, in this case, faced centered central composite design (CCF). It was found that independent variables have significant liner and quadratic effect on dependent variables. The optimum operating conditions were referred as peak temperature= 300 °C and heating rate=9.0 °C/min considering low energy input and high efficiency. The desirability for all responses reached to 0.63 and it was acceptable. Compared to conventional single factor optimization methods, which are time consuming and expensive with vague and misleading information, Design of Experiment (DOE) method performed in this research and the resulted model provide integrated and accurate results to systematically and effectively predict the response through various independent variables.

## Appendix III



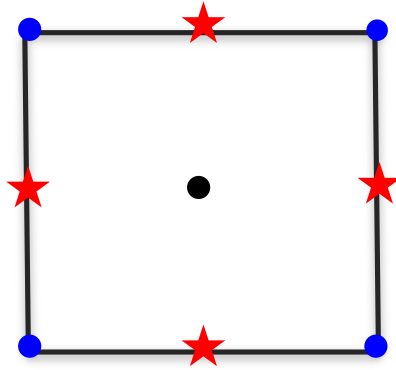


**Figure III- 1** Graphic representation of two-factor face-centered central composite designs

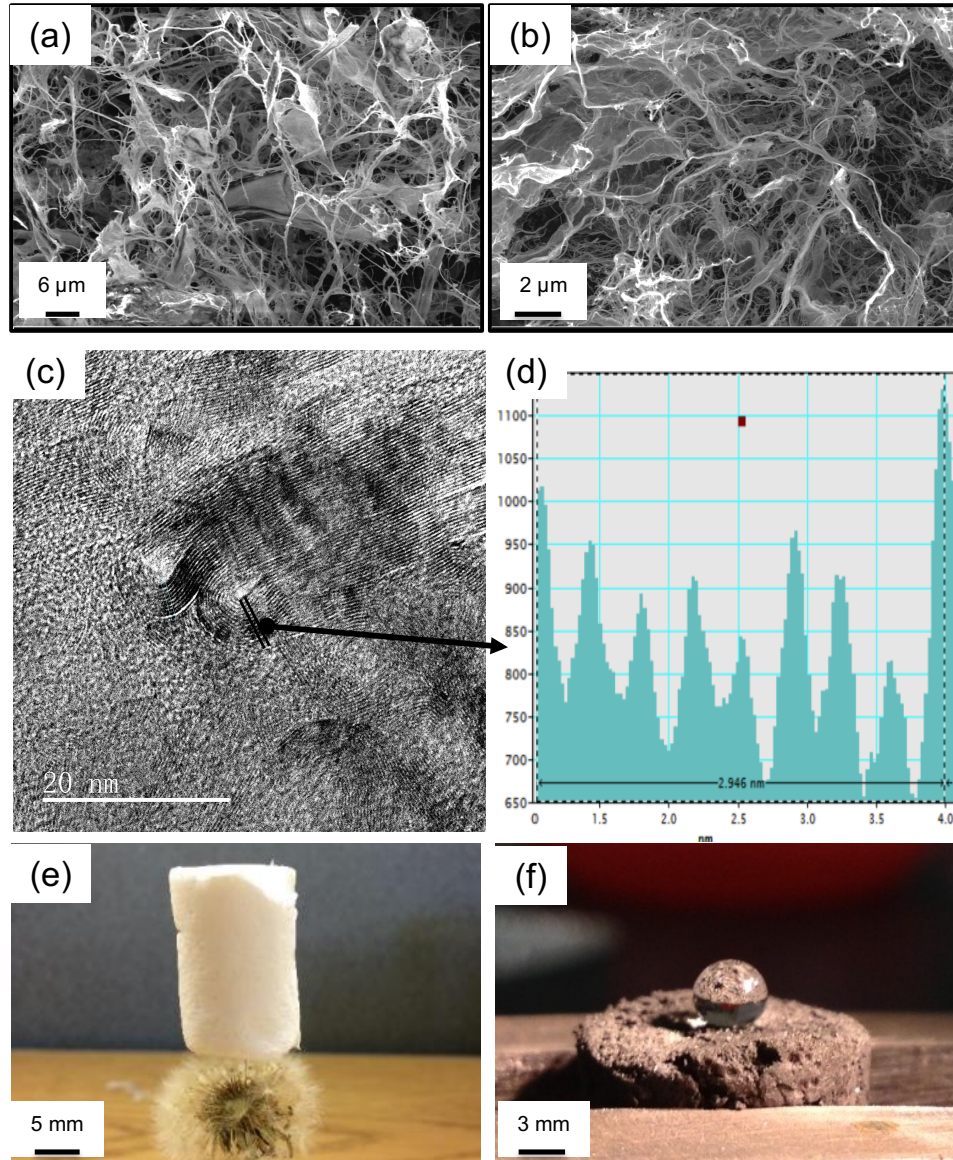


**Figure III- 2** SEM images of (a) NFC aerogel, (b) carbon aerogel heat treated at 1000 °C, (c) TEM images of graphite domain in the structure of carbon aerogel heat treated at 1000°C, (d) line profile of graphite domain from the same sample, (e) NFC aerogel sitting on the flower and (f) carbon aerogel holding a water droplet on the surface

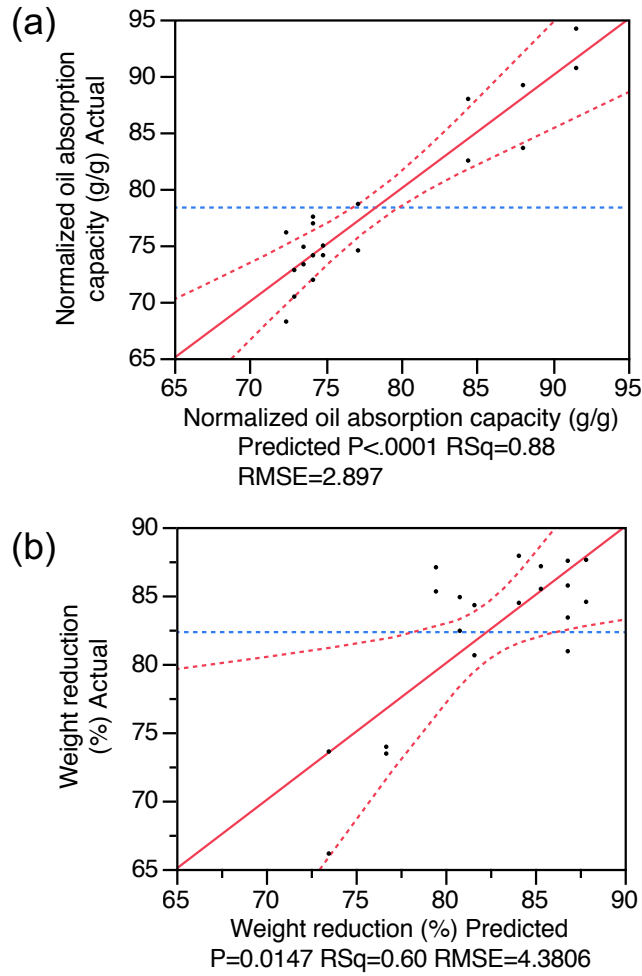


**Figure III- 3** (a) Goodness-of fit between predicted values obtained via partial least squares fitting and experimentally measured oil absorption capacity values and (b) between predicted values obtained and experimentally measured weight reduction

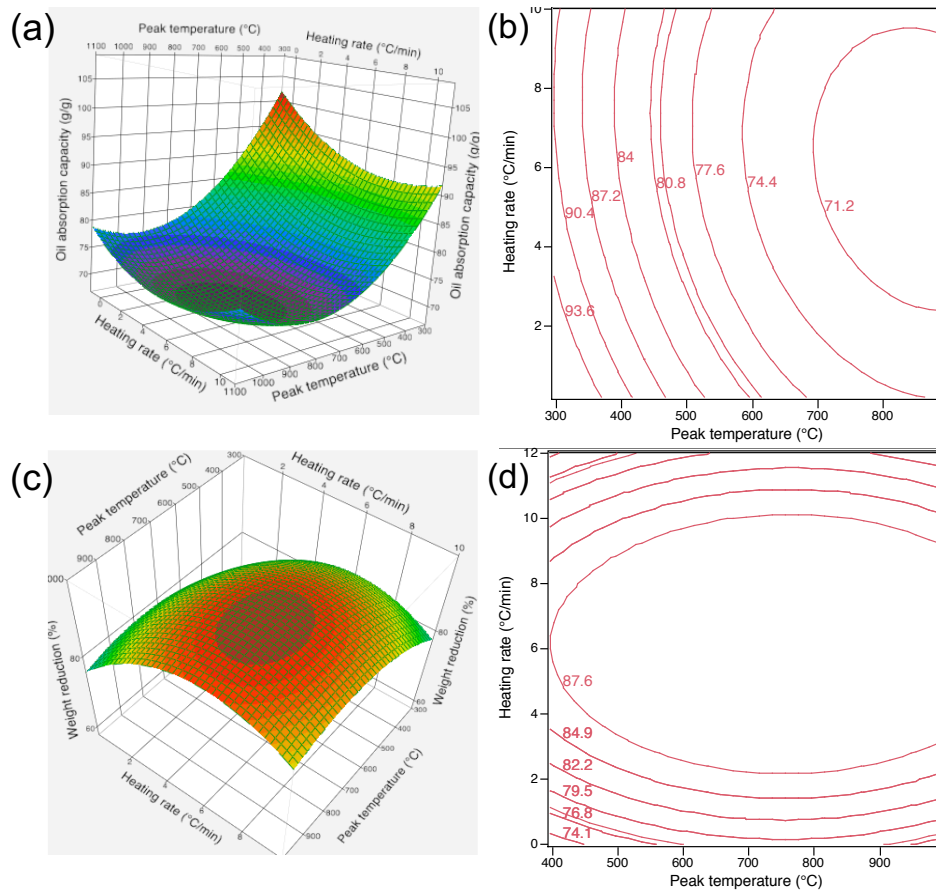


**Figure III- 4** (a) response surface plot and (b) contour profile representing the interaction between the variables affecting the normalized oil absorption capacity by oil density; (c) response surface plot and (d) contour profile representing the interaction between the variables affecting carbon yield after carbonization.

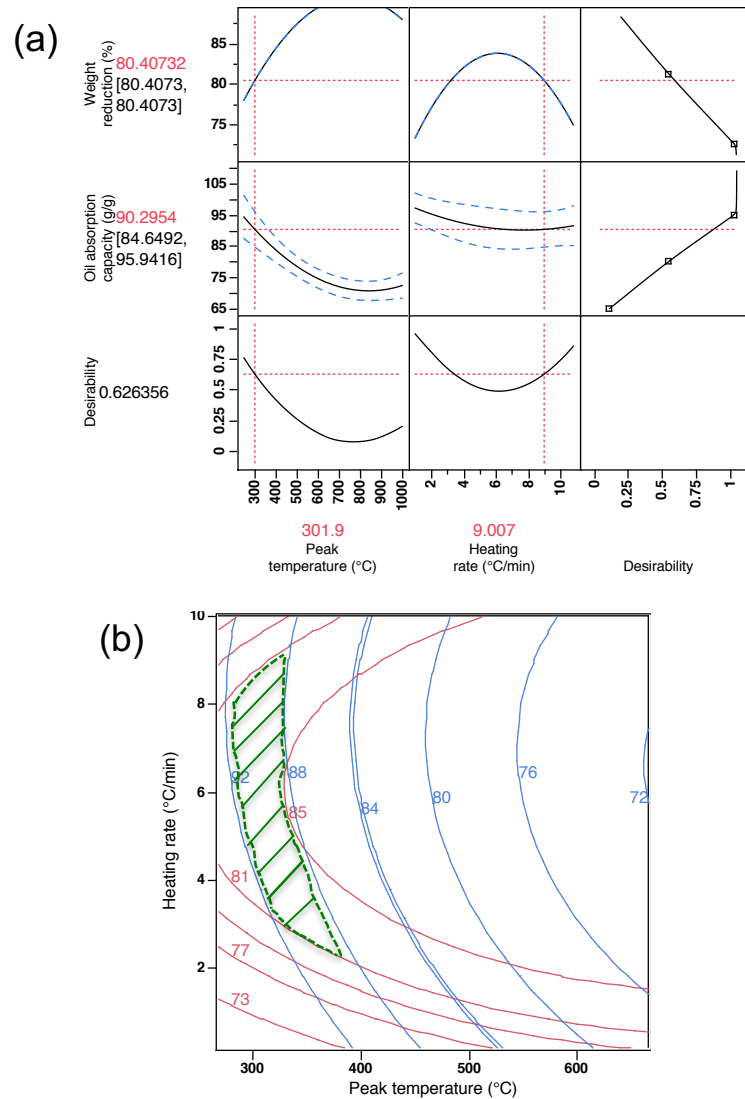


**Figure III- 5** (a) Prediction profiler shows optimization prediction plots and (b) overlaid contour plot for normalized oil absorption capacity (g/g) and weight reduction (%)

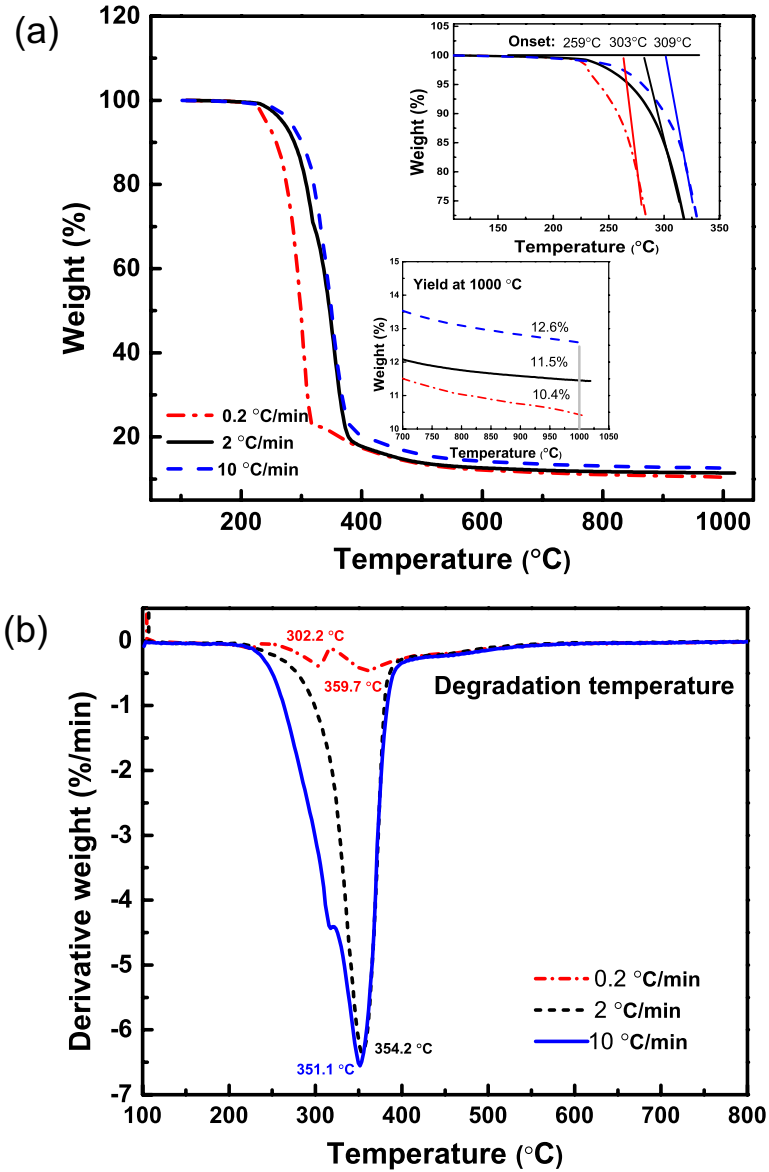


**Figure III- 6** Thermogravimetric analysis (TGA) showing the effect of heating rate during temperature rising from 230 to 320 °C on carbon residual yield at 1000 °C (a) TGA curve and (b) DTG curve

**Table III- 1** Independent variables and their values for oil absorption capacity

<b>Factor</b>	<b>Level</b>		
	<b>Low</b>	<b>Center</b>	<b>High</b>
Peak temperature (°C)	400	700	1000
Heating rate (°C/min)	0.2	2	10

**Table III- 2** Second-order central composite on face design, experimental data for three-level-two factors response surface analysis

Serial number	Pattern	Independent variable		Response variable	
		Peak Temperature (°C)	Heating rate (°C /min)	Oil absorption capacity Q <sub>s</sub> (g/g)	Weight reduction (%)
1	--	400	0.2	90.69	73.58
2	--	400	0.2	94.18	66.12
3	a0	400	2	89.18	84.87
4	a0	400	2	83.61	82.41
5	+-	400	10	82.49	84.29
6	+-	400	10	87.95	80.62
7	0a	700	0.2	78.65	87.05
8	0a	700	0.2	74.53	85.29
9	00	700	2	76.93	85.72
10	00	700	2	77.52	87.53
11	00	700	2	71.94	83.38
12	00	700	2	74.1	80.91
13	0A	700	10	72.8	87.60
14	0A	700	10	70.44	84.52
15	+-	1000	0.2	74.11	73.43
16	+-	1000	0.2	74.97	73.93
17	A0	1000	2	68.23	87.89
18	A0	1000	2	76.13	84.45
19	++	1000	10	73.31	85.47
20	++	1000	10	74.86	87.13



**Table III- 3** Analysis of Variance (ANOVA) for response surface quadratic model

Source	Degree of freedom (df)	Sum of squares	Mean squares	F Ratio	Prob>F
<b>Response: normalized oil absorption capacity (g/g)</b>					
Model	5	883.9243	176.79	21.06	<0.0001*
Peak temperature	1	539.58	539.58	64.29	<0.0001*
Heating rate	1	53.27	53.27	6.34	0.0245*
Peak tem* Heating rate	1	19.38	19.38	2.31	0.1509
Peak tem <sup>2</sup>	1	170.84	170.84	20.36	0.0005*
Heating rate <sup>2</sup>	1	19.56	19.56	2.33	0.1491
Residual	14	117.50	8.39	-	-
Lack of fit	3	16.80	5.60	0.61	0.6213
Pure error	1	100.70	9.15	-	-
Total	19	1001.42			
<b>Response: weight reduction (%)</b>					
Model	5	407.13	81.42	4.23	0.0147*
Peak temperature	1	33.81	33.81	1.76	0.2056
Heating rate	1	210.23	210.23	10.96	0.0052*
Peak tem* Heating rate	1	0.14	0.14	0.0075	0.9324
Peak tem <sup>2</sup>	1	89.28	89.28	4.65	0.0489*
Heating rate <sup>2</sup>	1	136.40	136.40	7.11	0.0184*
Residual	14	268.66	19.19	-	-
Lack of fit	3	192.70	64.23	9.30	0.0024*
Pure error	11	75.95	6.90	-	-
Total	19	675.76			

**Table III- 4** Estimated regression coefficients for normalized oil absorption capacity and weight reduction

<b>Term</b>	<b>Estimate</b>	<b>Std Error</b>	<b>t Ratio</b>	<b>Prob&gt; t </b>	<b>Lower 95%</b>	<b>Upper 95%</b>
<b>Normalized oil absorption (g/g)</b>						
Intercept	71.37	2.06	34.51	<0.0001	66.94	75.81
Peak tem	-6.9	0.86	-0.80	<0.0001	-8.75	-5.05
Peak tem <sup>2</sup>	6.05	1.34	4.51	0.0005	3.17	8.93
Heating rate	-2.1	0.84	-2.52	0.0245	-3.90	-0.31
<b>Weight reduction (%)</b>						
Intercept	93.36	3.13	29.85	<0.0001		
Heating rate	4.19	1.26	3.31	0.0052	1.47	6.90
Heating rate <sup>2</sup>	-9.69	3.63	-2.67	0.0184	-17.49	-1.89
Peak tem <sup>2</sup>	-4.37	2.02	-2.16	0.0489	-8.72	-0.02

## **CHAPTER IV**

# **LOCAL STRUCTURE INVESTIGATION OF DISORDERED CARBONS FROM CELLULOSE AND LIGNIN BY SCANNING TRANSMISSION ELECTRON MICROSCOPE (STEM)**

A version of this chapter was submitted to the *Biomacromolecules* on July 06<sup>th</sup>, 2015.

Authors:

Y. Meng, T.M. Young, S. Wang

*Department of Forestry, Wildlife and Fisheries, Center for Renewable Carbon, University of Tennessee, Knoxville, TN, USA*

C. Contescu, M. F. Chisholm

*Oak Ridge National Laboratory, Oak Ridge, TN 37831, USA*

P. Liu, J. Guo

*Key Laboratory of Interface Science and Engineering in Advanced Materials of Ministry of Education, Taiyuan University of Technology, Taiyuan 030024, China*

S. Lee

*College of Forest and Environmental Sciences, Kangwon National University, 200-701 Korea*

Y. Meng's primary contribution to this paper includes identifying the research objective, design and conduct of the experiments, process and interpretation of the data, drafting the paper.

Co-researchers' contributions are listed as follows:

C. I. Contescu revised the paper and performed the Nitrogen adsorption-desorption experiment.

P. Liu worked with Y. Meng on TEM sample preparation and performed HR-TEM observation.

T. M. Young revised and language polished the paper.

M. F. Chisholm provided research guidelines and experiment facilities

J. Guo performed STEM experiment and analyzed TEM experimental data.

S. Wang identified the research objective, provided research guideline and revised the paper.

S. Lee provided research guidelines.

**Abstract:**

An electron microscopy investigation was performed to link the microstructure and properties of carbonized cellulose and lignin with the structure of original biomass components. Structure details at micro and molecular levels have been investigated by scanning transmission electron microscopy (STEM). Atomic resolution images revealed the presence of random, fractured graphene fragments in carbonized cellulose (C-CNC) and of large domains of parallel stacked graphene in carbonized lignin (C-Lignin). These structural differences explain why C-CNC exhibits higher surface area and porosity than C-Lignin. The results of this research contribute to better understanding of the carbonization mechanism of the most important components of biomass materials: cellulose and lignin.

## 1. Introduction:

By converting biomass into fuels, power, materials and chemicals, biorefining is gradually making contributions to sustainable industrial development. (Ragauskas et al., 2006) Biomass is a combination of three major biopolymers: (1) Cellulose is an aggregate of linear chains of glucopyranose units linked by  $\beta$ -(1,4) glycosidic bonds to varying degrees of polymerization. The chains held together in parallel stacks by intra- and inter- molecular hydrogen bonds form short-range nanocrystalline regions. The cellulose nanocrystals (CNC) alternate with amorphous regions and form microfibrils held by weak van der Waals forces. (Moon et al., 2011) (2) Hemicellulose consists of wide groups of highly branched heteroglycans. (3) Lignin is a complex polymer of aromatic alcohols (monolignols) composed mainly of three phenylpropane monomers: *p*-coumaryl alcohol, coniferyl alcohol, and synapyl alcohol.

Bioresources are abundant, renewable, sustainable, biocompatible and biodegradable; they carry the most abundant natural aromatic polymers in the world. (Langan et al., 2014) Converting biomass into carbon materials is of extreme interest for the development of high-value added products used for energy storage and conversion in batteries and supercapacitor, environment remediation, gas separation and storage, drug delivery, etc. (Meng et al., 2014, He et al., 2014b, Dobele et al., 2012, Wang et al., 2013, Zhao et al., 2012) The increased interest in biomass conversion into usable products is exemplified by a series of recent studies on synthesizing graphene from rice husk and hemp, (Wang et al., 2013, Muramatsu et al., 2014) investigating onion-like graphitic and diamond structures in wood charcoal, (Hata et al., 2000, Ishimaru et al., 2001) and obtaining carbon nanotubes from carbonization of grass and wood hierarchically structured fibers. (Goodell et al., 2008) In essence, synthesis of all these carbonaceous materials occurs through a complex process involving oxidation, pyrolysis and carbonization.

The promise of manufacturing low-cost carbon fibers from lignin and cellulose precursors, a main driver of the biorefining concept, still faces great challenges and is not ready for industrial scale production and application. One problem to be tackled is the poor mechanical properties of resulting products, which is caused by the porous, disordered structures of carbonized products. In fact, there exists a certain link between the carbon precursor chemistry

and the final morphology of carbonized material. Attempts have been made to study and compare the oxidative stabilization and carbonization kinetics of cellulose and lignin using only spectroscopic analysis. They showed that lignin and cellulose exhibit different carbon to oxygen ratios, which drastically affects the conversion mechanism and influences the microstructure of the resulting carbon. (Cao et al., 2013, Xie et al., 2009, Ishimaru et al., 2007) Nevertheless, understanding the structure — property relationship of biomass-derived carbonaceous materials at local length scales remains a significant research challenge.

Recently, the local structure of porous carbon became accessible to investigation thanks to the development of atomic-resolution electron microscopy. Using this technique it was recently demonstrated that the nanoscale structure of wood-based carbons contains randomly stacked, wrinkled graphene sheets. (Guo et al., 2012, He et al., 2014b) Their variable architectural arrangement at the microscale creates a network of interconnected nanopores with large internal surfaces, which determine the main functional property of porous carbons. At the atomic scale, the curvature of individual graphene is determined by topological defects, such as 5- and 7-atoms carbon rings, randomly interspersed between regular 6-atoms carbon rings. With this complex architecture, porous carbons exhibit short-range atomic order at sub-nanometer scale, but appear as an isotropic, amorphous material at the microscale. The complicated structure and varying chemical composition of wood components is a great challenge for better understanding of the carbonization mechanism of each component. The origin of locally ordered graphene fragments and the formation mechanism of biomass based porous carbon are still elusive at the atomic level. Our research hypothesis is that the variability of biomass precursor's components gives rise to a large structural diversity of the resulting carbon materials.

Direct imaging of CNC by HRTEM is of great importance to probe and manipulate size-dependent physical and chemical properties of CNC at the nanoscale (Aina et al., 2013). Because of the difficulty in preparing and observing CNC due to the bio-nature of the material, very few researchers to date captured the lattice structure of CNC. A negative-staining technique was used to facilitate the CNC observation and enhance the contrast by surrounding or embedding CNC in heavy melt material. (Xu et al., 2013, Liu et al., 2011) However, these radioactive salts impede accurate observations. In our research we successfully resolved the lattice structure of CNC without using negative staining. This is important for fundamental understanding of structural



transformations during cellulose conversion to carbon. The loss of crystallinity of CNC structure caused by beam irradiation was also observed in this research.

In this work we compare two types of carbons obtained through identical carbonization conditions from cellulose nanocrystals and lignin. We report that under identical condition, nanocrystals extracted from cellulose convert into disordered graphene-based nanoporous structures typical for porous carbons, while carbonized lignin forms non-porous mixtures containing parallel-stacked graphene and globular onion-like inclusions dispersed through an amorphous matrix. The local atomic structure of original CNC and of carbon derived from CNC and lignin was probed for the first time. The local structure differences between carbonized cellulose (C-CNC) and carbonized lignin (C-Lignin) explain the difference of porosity and surface area measured by nitrogen adsorption. This research contributes to better understanding of the carbonization mechanism of various biomass components.

## **2. Experimental procedure**

### **2.1 Materials**

The CNC material studied here was derived from high-purity CF11 cellulose powder (Waterman, USA). Sulfuric acid ( $\text{H}_2\text{SO}_4$ , 95-98%, Sigma Aldrich) was used for acid hydrolysis. Indulin AT softwood kraft lignin sample was commercially available from MeadWestvaco (Charleston, SC.).

### **2.2 Preparation of cellulose nanocrystal and lignin**

CF11 cellulose was hydrolyzed by adding ten grams powder to 100 mL sulfuric acid (60 wt%) at 45 °C for 45 min under constant stirring. Cold distilled water was added to end the acid hydrolysis reaction. The hydrolyzed cellulose was washed and nanocrystals were separated from the solution by centrifugation (4,000 rpm, 20 min). The precipitate was then dialyzed against water for 4 days using membrane with a molecular weight cutoff of 12,000–14,000 (Fisher brand, Pittsburgh, PA) until a constant neutral pH was achieved. The commercial lignin powder was washed with DI water to remove salt impurities, dried in vacuum at 80 °C, and stored in the desiccant cabinet ready for use.

### **2.3 Carbonization of cellulose nanocrystal and lignin**

CNC suspension (0.7 wt %) was frozen using liquid nitrogen and freeze-dried in a vacuum lyophilizer (Labconco, Inc., Kansas City, MO) at temperature of -51 °C for three days. The dried CNC and lignin powder were stabilized in air (20 mL/min) and then carbonized in nitrogen (20 mL/min) using a Lindberg/blue M Mini-Mite tube furnace (Thermo Scientific). The process includes (1) heating the sample from room temperature to 180 °C at a rate of 10 °C/min in air; (2) increasing the temperature from 180 °C to 230 °C at a rate of 5 °C/min in air; and (3) increasing the temperature from 230 °C to 320 °C at a rate of 2 °C/min in air; (4) increasing the temperature from 320 °C to 950 °C at a rate of 5 °C/min in nitrogen and holding for 15 min. The resulting samples were grinded and dispersed into DI water. The mixture was sonicated continuously for 20 min with an ultrasonic probe.

### **2.4 Nitrogen adsorption**

Nitrogen adsorption/desorption isotherms at -196 °C were measured on a Quantachrome Autosorb 1C instrument with ASIQ Win 2.0 data processing software. Prior to measurements, samples were degassed for 1.5 hours at 300 °C in vacuum of (0.1 Pa) to remove moisture and other volatile species. The pore surface area, pore volume and pore size distribution were determined by the quenched surface density functional theory (QSDFT) model for slit / cylindrical pore geometry. In this case, open pores in the range of supermicropores (0.7-2 nm) and mesopores (2-50 nm) were investigated. Specific surface areas (m<sup>2</sup>/g) evaluated by Brunauer-Emmett-Teller method using nitrogen adsorption data at -196 °C in the relative pressure ( $p/p_0$ ) range from 0.05 to 0.35 were reported as well.

### **2.5 Electron microscopy**

Suspension drops (0.001 wt %) of CF11 cellulose nanocrystals were deposited on Holey silicon nitride support film (Ted Pella, Inc., USA) for TEM observation. The carbonized CNC and lignin samples were dispersed into deionized distilled water and treated with high-intensity ultrasonic processor (HIUS, 1500 Watt Model, SONICS Newtown, CT) to obtain the small fragments. Spin coating technique was used during the deposition to avoid aggregation of CNC.

The grids were placed into a high-resolution transmission electron microscope (Libra 200 MC, Zeiss), which was operated at a 200 kV accelerating voltage. The atomic structure of CNC was studied using a 5<sup>th</sup> order spherical aberration corrected scanning transmission electron microscope (Nion-UltraSTEM100), which is operated at a low accelerating voltage of 60 kV to avoid the irradiation damage to samples.

## 2.6 Thermal gravimetric analysis

The thermal stability and carbonization yield were characterized using thermal gravimetric analyzers (TGA; Perkin–Elmer 7 series; Perkin–Elmer Cetus Instruments, Norwalk, CT). The heating program was set up to mimic the carbonization process.

## 2.7 Wide-angle X-ray diffraction

X-ray diffraction measurements were carried out on a Scintag DMC 008 X-ray diffractometer with Cu-target radiation at 40 kV and 40 mA and a measuring angle from 5° to 40° (step size=0.02°, scanning rate 2 s/step). Powder samples were pressed into flat disks and attached to the glass plate. The crystallinity index (CrI) was calculated from diffraction patterns by using the following equation (Segal et al., 1959):

$$\text{CrI} = \left( \frac{I_{200} - I_{\text{am}}}{I_{200}} \right) \times 100 \quad (1)$$

$I_{200}$  where  $I_{200}$  is the intensity of (200) peak ( $2\theta=22.4^\circ$ ) and  $I_{\text{am}}$  is the minimum intensity at the valley between peaks (200) and (110) ( $2\theta=18^\circ$ ).

The lateral crystal dimension of the crystal with  $hkl$  Miller indices,  $D_{hkl}$ , was calculated by Scherrer's expression:

$$D_{hkl} = K\lambda / (\beta_{1/2} \times \cos\theta) \quad (2)$$

where  $K=0.94$ ,  $\theta$  is the diffraction angle,  $\lambda=0.154$  is the X-ray wavelength and  $\beta_{1/2}$  is the peak width at half maximum intensity of the (hkl) peak.

## 2.8 Fourier transform infrared spectroscopy (FTIR)

FTIR was performed using a Perkin Elmer FTIR-ATR spectrometer (Spectrum One, Perkin Elmer, USA). Samples were placed on a diamond crystal of an attenuated total reflectance (ATR) accessory. All spectra were collected over a range of 4000 to 600  $\text{cm}^{-1}$  at 4  $\text{cm}^{-1}$  resolutions with 16 scans. Samples were recorded before and after carbonization.

## 3. Results and discussion

### 3.1 Porosity information from nitrogen gas adsorption

The results of porosity studies are plotted in Figure IV-1. The  $\text{N}_2$  adsorption-desorption isotherms of C-CNC and C-Lignin feature typical type-II curves combined with  $\text{H}_4$ - type hysteresis loop (Sing et al., 1985). This type of isotherms and the narrow hysteresis loops are attributed to inter-particle capillary condensation.

For C-CNC, the adsorption amount undergoes a steep increase at relative pressure ( $p/p_0$ ) of  $\sim 0.1$ , indicating the completion of the first monolayer and transition to multilayer adsorption. In addition, the presence of hysteresis loop with lower closure point at  $p/p_0 \sim 0.4$  and higher closure point at  $p/p_0 \sim 0.9$  is related to the filling and emptying of mesopores by capillary condensation. The porous structure characteristics of C-CNC and C-Lignin are listed in Table IV-1. There are significant differences between these carbonized samples. The surface area of C-CNC sample calculated from QSDFT and BET methods ranges between 556 and 562  $\text{m}^2/\text{g}$ . In contrast, C-Lignin has much lower surface area, in the range of 32 to 47  $\text{m}^2/\text{g}$ . Furthermore, C-CNC has a larger specific pore volume than C-Lignin does. The pore size distribution of C-CNC shows a small fraction of micropores ( $< 2$  nm) and a large proportion of mesopores (2-50 nm) centered at about 4.7 nm. On the contrary, C-Lignin exhibits a broad pore size distribution, with a smaller volume of mesopores centered at about 2.8 nm. The ratio of total pore volume to BET area is larger for C-Lignin than for C-CNC. This might be the result of the loose packing of C-Lignin particles, associated with interparticle voids rather than intraparticle pores. As such, it can be speculated that the reason for the difference in adsorption properties may be related to the variance of morphological structure between C-CNC and C-Lignin.

### **3.2 Observation of cellulose nanocrystal and lattice structure**

Gentle STEM was used to study the structure of original CNCs. The high resolution transmission electron microscopy (HRTEM) image in Figure IV-2 (a) shows typical spindle-like whiskers with length in the range of 100-300 nm and width in approximately 3~5 nm. Aggregated bundles of CNC were also observed due to the lateral adhesion among elementary crystallites. The annular dark-field (ADF) higher magnification image in Figure IV-2 (b) clearly shows that CNCs are composed of highly ordered structures. Large domains of cellulose chains were packed tightly together with a high degree of alignment. The formation of cellulose crystalline region can be ascribed to the intra and intermolecular hydrogen bonds that holds closely packed glucose chains. (Nishiyama et al., 2002) The gentle STEM experiment confirms the CNCs' crystalline structure by direct observation. The appearance spacing of observed lattice fringes is measured to be about 0.4 nm. The value is consistent with the d-spacing value of 0.39 nm, which corresponding to the (200) lattice plane of cellulose I.

Observing cellulose nanocrystal without negative staining by STEM is quite challenging due to the material nature and inconvenient sample contamination. Figure IV-3 illustrates the beam irradiation effect on the CNCs. It is of interest to note that these lattice properties are not sustained under electron beam, even though the accelerating voltage of microscope is only 60 kV. The diffraction pattern inserted in Figure IV-2 (a) indicates the good crystallinity of the original CNCs. Shortly after the observation, the crystal structure started to disappear and tended to become amorphous, as seen in Figure IV-2 (b). This is to be expected, since, the beam energy (67.54 kJ/mol) is larger than the bonding energy of hydrogen bonds (5 to 30 kJ/mol), but smaller than the activation energy for depolymerization of cellulose (242.8 kJ/mol). (Shen et al., 2013) Accordingly, it is the high energy of TEM beam that broke the intermolecular hydrogen bonds, which hold together the linear chains of  $\beta$  (1,4) glucose molecules.

### **3.3 Observation of graphene in carbonized cellulose nanocrystal and carbonized lignin**

The top row in Figure IV-4 shows high-resolution STEM images of C-CNC and C-Lignin. The fringes visible in these images represent edge-on view of graphene layers. An

obvious difference between the microstructures of C-CNC and C-Lignin is seen by comparing Figures IV-4 (a) and (b). The image of C-CNC sample consists of short, randomly orientated graphene fringe fragments. The random arrangement of these small fragments creates numerous voids that form the network of interconnected micropores and mesopores. In contrast, such turbostratic carbon structure was not observed in C-Lignin sample. This sample exhibits two types of fullerene-like structures. Figure IV-4 (b) shows ribbon-like structures composed of 3-4 layers of parallel stacked carbon layers forming continuous loops, about 15 to 30 nm long. Similar structures were reported by other researchers (Johnson et al., 1975). Such large regions of closed packed layers were never observed in the C-CNC sample. The second component appears with high incidence in numerous images, such as the one shown in Figure IV-4 (c). These faceted onion-like particles are pentagonal or hexagonal in shape. The black circular spot marked by red arrow in Figure IV-4 (c) is about 20 nm in *diameter*; the interplanar distance measured for the dense core is 0.34 nm. The diffraction pattern inserted in Figure IV-4 (d) confirms the existence of periodic crystal structures in C-Lignin sample.

The microstructural features evidenced by electron microscopy observations explain the differences in BET surface area and pore size distribution between C-CNC and C-Lignin. These observations indicate that, under identical carbonization conditions, the transformation of lignin structure into well-ordered, stacked graphene sheets is more facile compared to that of CNC. That is to say that the structure and chemical nature of precursor materials (cellulose, lignin) has a pronounced effect on the conversion process and the structure of the carbonized product.

Atomic resolution ADF images were obtained from the very thin regions at the edge of carbonized CNCs particles. Figure IV-5 (a) shows C-CNC atomic structure at high magnification. Clearly, the stacking configuration of graphene layers can be described as a pack of numerous, randomly curved atom-thick layers. Careful examination at very high magnification reveal details of carbonized CNC structure. A small single-layer graphene fragment was found suspended on one particle edge and oriented parallel to the image plane; its in-plane carbon atoms are clearly resolved (Figure IV-5 (b)). To better analyze the atomic arrangement, each bright spot representing a carbon atom was marked with a white dot on the image. The one-layer graphene is composed of a hexagonal lattice of carbon atoms which also contains nonhexagonal defects (atoms are bonded in pentagonal or heptagonal rings). Studies on nanoporous carbon

derived from wood-based material revealed domains of imperfectly stacked graphene layers with rippled shapes. The topological defects represented by nonhexagonal carbon atom rings generate highly porous structure high surface area carbons. (Guo et al., 2012) Our observation on C-CNC sample is consistent with the previous report, indicating that as-prepared C-CNC is composed by randomly curved graphene layers. Their presence explains the higher BET surface area and porosity of C-CNC.

### **3.3 Thermogravimetric analysis**

Thermogravimetric analysis was used for better understanding of carbonization mechanism differences between cellulose and lignin. The temperature profile mimicked the tube furnace carbonization process. Figure IV-6 shows the weight loss (TG) and derivative of weight loss (DTG) during carbonization. It is generally agreed that the process of cellulose pyrolysis consists of four stages: (1) physical desorption of water (25-150 °C), (2) dehydration of the cellulose unit (150-240 °C), (3) thermal cleavage and scission (240-400 °C), and (4) aromatization and carbonization (400 °C and above) (Tang and Bacon, 1964b, Meng et al., 2014). These four stages can be recognized in Figure IV-6. A major slope change of the TG curve was observed between 180 and 400 °C, consistent with the TGA analysis (Cao et al., 2009) for CNC extracted from cotton by sulfuric acid hydrolysis. Two sharp peaks in the DTG plots at 180.9 °C and 228.9 °C, accompanied by weight loss of 4.4 % and 21.8 %, were attributed to water evaporation and dehydration respectively (Dumanli and Windle, 2012). The DTG peak at 320.9 °C and the broad peak between 350 and 400 °C can be traced to complicated reactions of depolymerization and aromatization through the whole carbonization process. In contrast, lignin shows a stepwise decrease of the TG curve a broad temperature range from about 250 to 700 °C. Unlike CNC material, the DTG curve for lignin shows a single broad peak centered at about 390 °C, corresponding to 20% weight loss. A similar trend was reported by others (Yang et al., 2007). The onset temperatures, decomposition temperatures and the total weight loss at 950 °C are summarized in Table 2. Compared to lignin, CNC sample started to decompose at lower temperature.

The FTIR spectra of the CNC and lignin sample and of their corresponding carbonized materials (Figure IV-7) show that the oxygen-containing functional groups were thoroughly removed by thermal treatment at 950°C.

### 3.4 X-ray Diffraction (XRD) analysis

The XRD pattern of CNC shows typical cellulose peaks marked at  $2\theta=22.5^\circ$ ,  $14.6^\circ$  and  $16.5^\circ$ , corresponding to its crystal lattice assignment of (200), (1-10) and (110) crystalline planes (Figure IV-8). Crystallinity was calculated to be of 81% using equation 1. Carbonization treatment at 950° of CNC sample leads to the disappearance of (200), (1-10) and (110) diffraction peaks. A weak, broad peak centered at  $2\theta=17^\circ$  was observed, indicating the formation of very disordered, turbostratic-like carbon after carbonization.

Lignin sample's XRD pattern barely exhibits a weak and broad peak centered at  $16^\circ$ , indicating the amorphous nature of lignin. The weak peak shifted to higher 2-theta of  $21.2^\circ$  upon carbonization treatment, but did not reach  $26^\circ$  which is the approximate position of (002) peak in graphite. This peak shift accompanied with the decrease in peak width indicate the trend of carbon layers stacking along the *c*-axis(Fujimoto, 2003). Similar peak profile was observed in other research(Tenhaeff et al., 2014). Using the Scherrer equation for the (002) peak, an average crystallite length  $L_c$  along *c*-axis of 1.1 nm was calculated. The interlayer spacing ( $d_{200}$ ) value for C-Lignin was calculated to be 0.37 nm, close to the value (0.34 nm) measured from the TEM image and the diffraction pattern. The average number of layers calculated as the ratio of  $L_c$  and  $d_{200}$  is 3, which is consistent with the observation from TEM image in Figure IV-4 (b). However the incidence of well-ordered graphene stacks remains low, despite the fact that they were captured by TEM images.

## 4. Discussion

Despite of lignin's structural and chemical variability, its branched and crosslinked structure consists of only three basic units, derived from coumaryl alcohol, coniferyl alcohol and sinapyl alcohol. (Thielemans et al., 2002) The high level of lignin's aromaticity contributes to its resistance to thermal degradation, as supported by low weight loss on TGA analysis. The high-



resolution TEM image of C-Lignin (Figure IV-4) suggests lignin's ability for formation of close packed graphene-stacked structures by carbonization. It can be argued that such preferential formation is related to the presence of aromatic monolignols in lignin. A possible path for lignin carbonization is presented in Figure IV-9. The large amount of aromatic ring structures with non-carbon atoms on edges favors aromatic condensation and sequential three-dimensional ordering during carbonization and heat treatment up to 950 °C.

The structure of high crystallinity cellulose (CNC), by contrast, is composed of repeating glucose units. A scheme of structural changes during cellulose carbonization is presented in Figure IV-10. During heat treatment from room temperature to 950 °C, cellulose experiences desorption of physisorbed water, intermolecular dehydration through  $-H$  and  $-OH$  condensation, thermal cleavage of glycosidic linkages, thermal scission of ether bonds and C-C bonds etc. Losty and Blakeock argued that oxygen existing in pyranose rings and glycoside links is eliminated during the decomposition process, making the main contribution to the total weight loss. (Davidson and Losty, 1963) Large amounts of carbonaceous intermediates consisting of aromatic platelets terminated by hydrogen would go through further thermal cleavage above 300 °C. Based on the TEM image (Figure IV-4) it can be speculated that cellulose intermediates polymerize to successfully form graphene units, yet fail to yield long-range stacking order. The oxygen elimination process requires high reactive energy to break the rings. In addition, the presence of covalently bonded hydrogen may hamper the aromatic condensation.

## **5. Conclusion:**

We have investigated the atomic structure of carbonized cellulose and carbonized lignin by aberration-corrected STEM. Lattice structure of CNC was directly observed, with no negative staining. Beam irradiation of crystalline CNC led to facile loss of crystallinity caused by breaking of hydrogen bonds. We have shown that carbon derived from highly crystallized cellulose yields disordered porous structure, while kraft lignin derived carbon has the tendency to yield larger graphene-stacked and onion-like structures. The randomly arranged small graphene fragments in carbonized CNC create a network of interconnected micropores and mesopores and contribute to the increased BET surface area. In C-Lignin, the development of parallel stacks of graphene structures and of onion-like inclusions is favored by the pre-existence of aromatic

components in lignin. High magnification STEM observations indicate that cellulose intermediates polymerize and successfully form graphene units, yet fail to yield long-range stacking order after treatment to 950 °C.

## Appendix IV

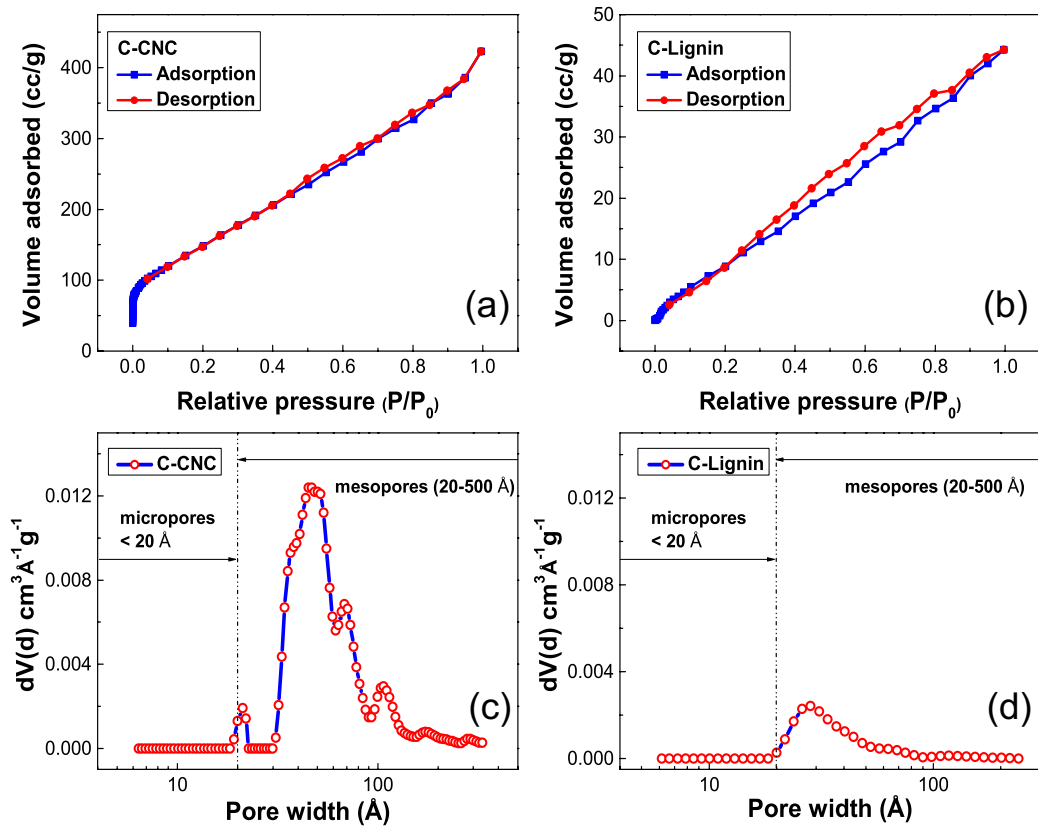


**Figure IV- 1** Adsorption-desorption isotherms of nitrogen on (a) C-CNC and (b) C-Lignin: blue and red lines are adsorption and desorption data, respectively. Pore size distributions determined by QSDFT method for (c) C-CNC and (d) C-Lignin.

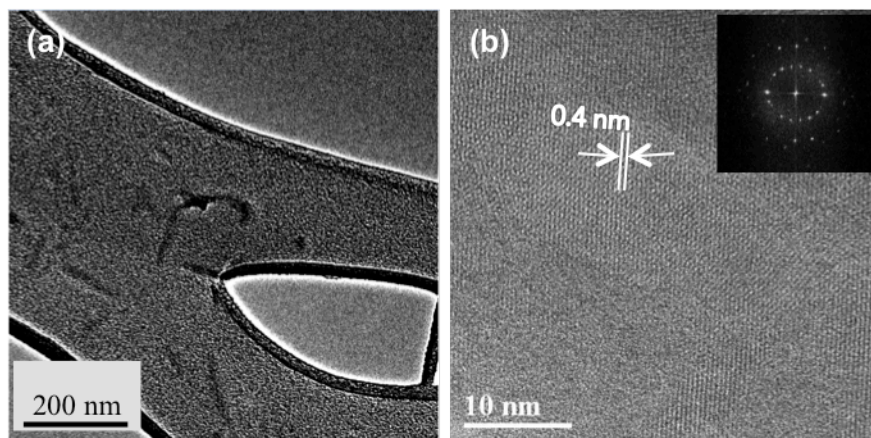


**Figure IV- 2** HRTEM image of individual CNCs (a) and annular dark-field (ADF) image of its lattice structure (b). The inset in the right upper corner is a Fast Fourier Transform (FFT) pattern.

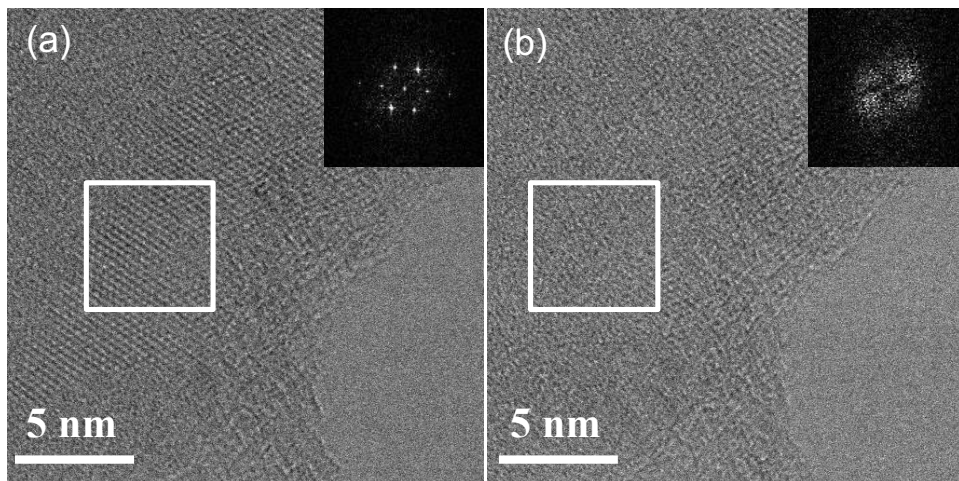


**Figure IV- 3** Annular dark-field (ADF) image of CNCs before (a) and after (b) beam irradiation. The inset in the right upper corner is a Fast Fourier Transform (FFT) pattern

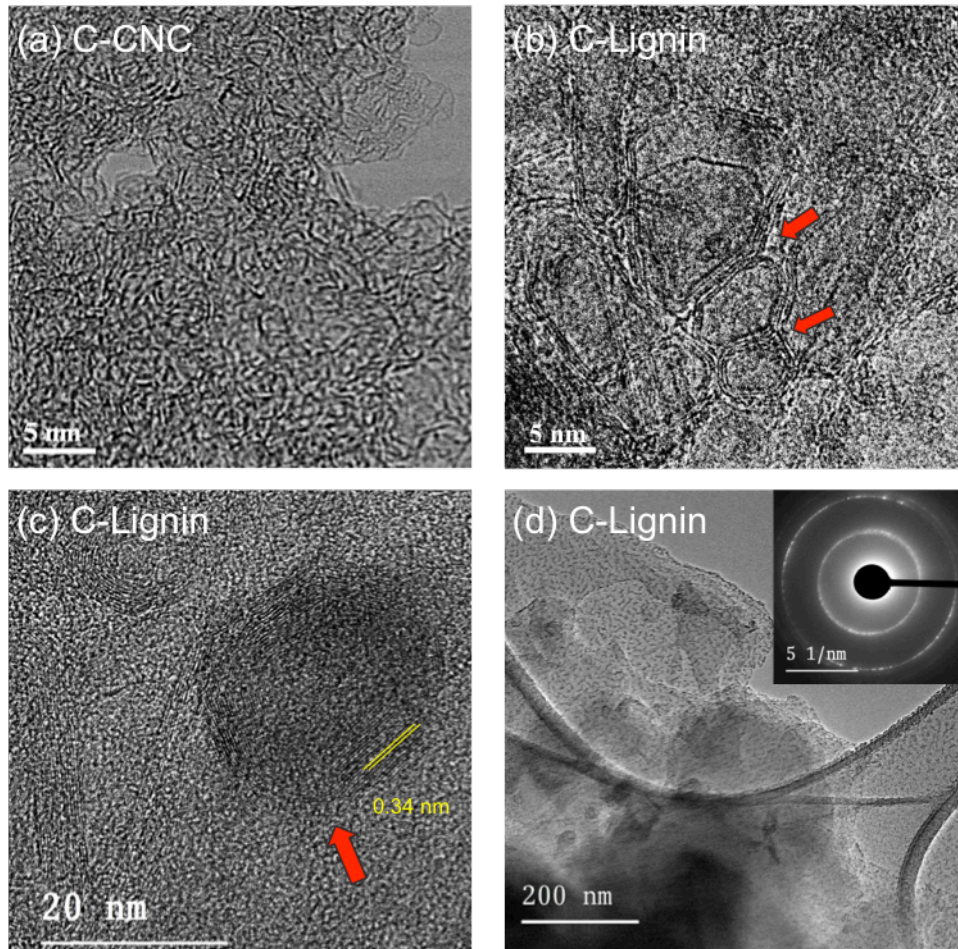


**Figure IV- 4** Micrographs of CNC carbon and lignin carbon following heat treatment at 950°C: Bright field STEM images of (a) C-CNC, (b) C-Lignin,(c) and (d) C-Lignin under low magnification, The Inset in the right upper corner of (d) is the diffraction pattern.

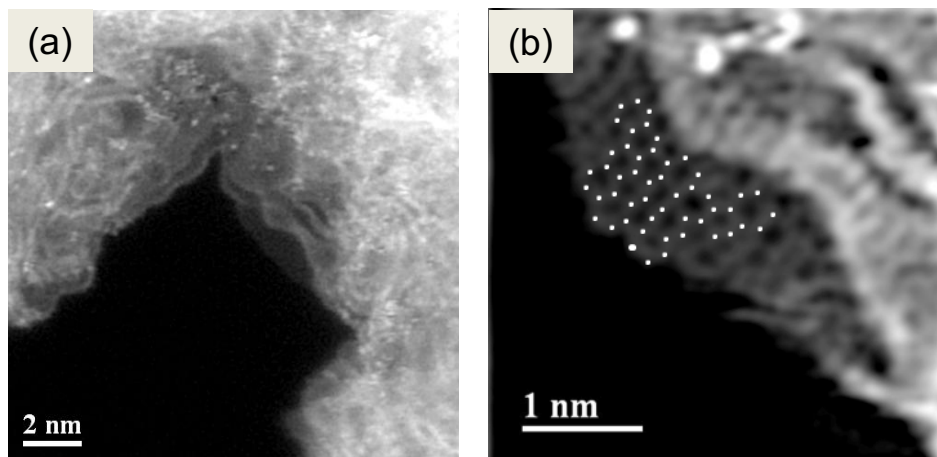


**Figure IV- 5** ADF images obtained from thin edge area of carbonized cellulose nanocrystals (a) low magnification (b) high magnification.



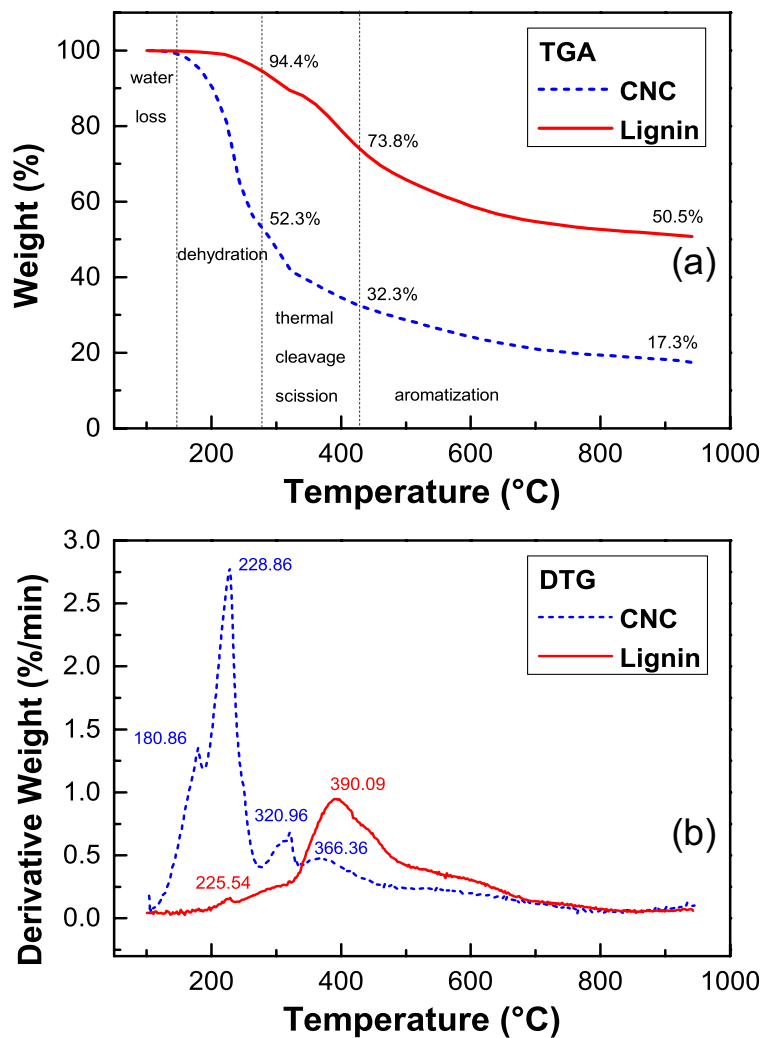


**Figure IV- 6** Typical TG-DTG curves in N<sub>2</sub> for cellulose nanocrystals and lignin (a) Percentage weight loss as a function of temperature and (b) Weight loss rate as a function of temperature.

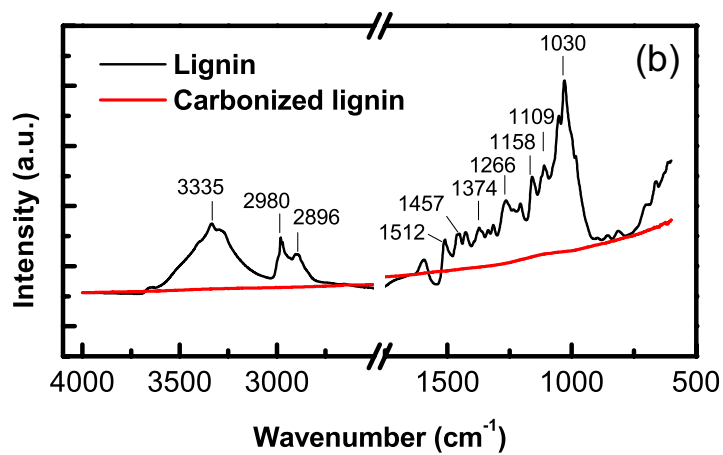
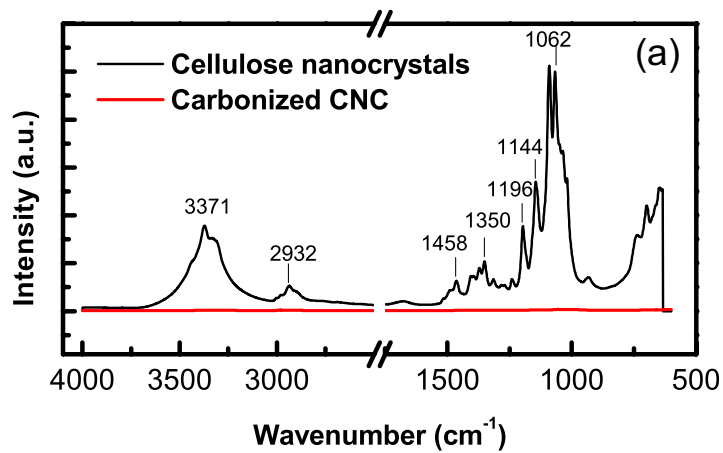


**Figure IV- 7** FTIR spectra of (a) cellulose nanocrystals and C-CNC (b), Lignin and C-lignin.

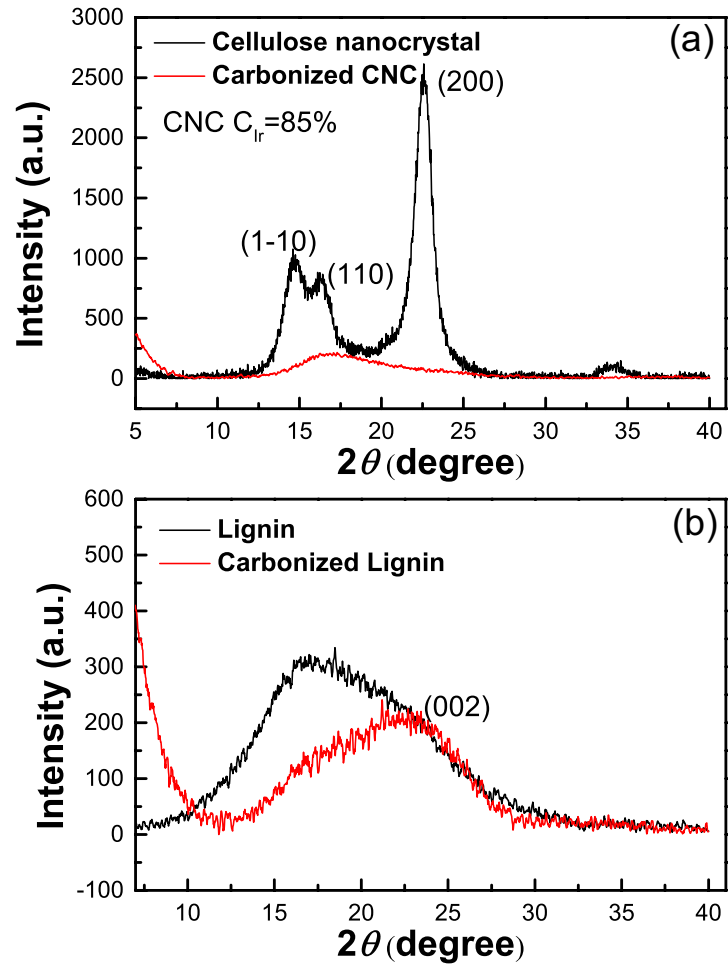


**Figure IV- 8** Wide-angle X-ray diffraction curves of CNC, C-CNC, Lignin and C-Lignin.

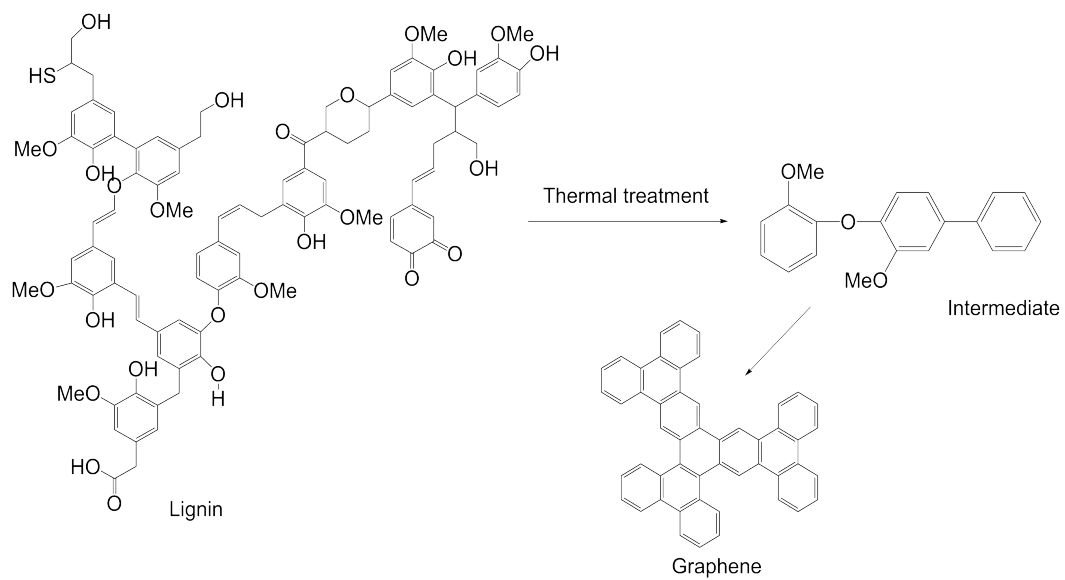


**Figure IV- 9** Schematic of lignin structure (adopted from Ball(Ball, 1992) ) evolution during carbonization.

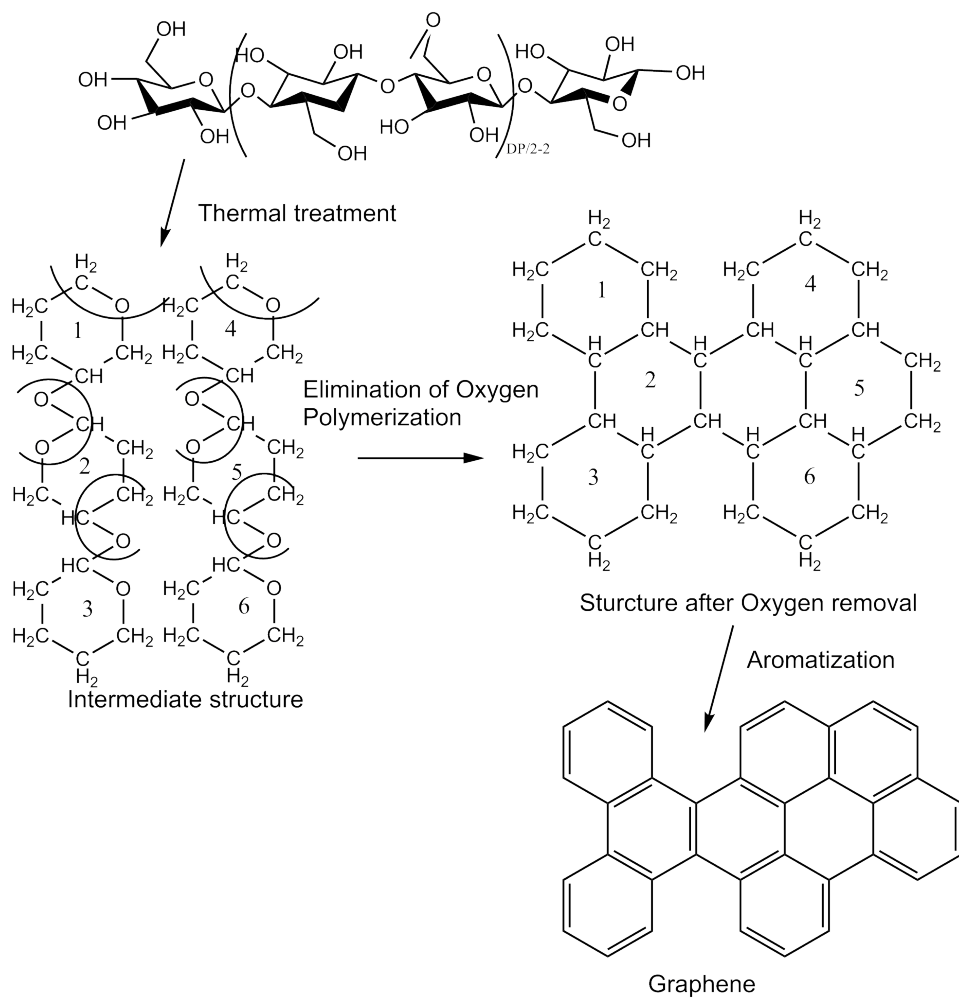


**Figure IV- 10** Scheme of cellulose structure and cellulose carbonization (adopt from Losty (Davidson and Losty, 1963)).

**Table IV- 1** Pore surface area and pore volumes of as-prepared C-CNC and C-Lignin

BET		Results from QSDFT analysis			
surface area (m <sup>2</sup> /g)		Pore surface area (m <sup>2</sup> /g)	Pore volume (cc/g)	Average pore diameter (Å)	Volume to area ratio (Å)
C-CNC	556	562	0.60	43.7	10.6
C-Lignin	47.7	32.2	0.06	28.4	18.6

**Table IV- 2** Onset temperature, degradation temperature, maximum weight-loss rates and weight loss of CNC and lignin

Carbon precursor	Onset temperature (°C)	Degradation temperature (°C)	Maximum weight loss rate (%/min)	Weight loss at 950 °C (%)
CNC	186.0	228.9	-2.82	82.6
Lignin	247.7	390.0	-0.98	49.3

## CONCLUSION

Nanoscale cellulose and its carbonaceous material were studied in this dissertation in terms of application and local structure investigation. The three-dimensional morphology of individual cellulose nanocrystals (CNC) was quantitatively and statistically measured by utilizing multi-characterization techniques such as atomic force microscope (AFM), Transmission Electron Microscope (TEM) and X-ray diffraction etc. The individual CNC was found to give the greatest value of thickness and width at the midpoint along the fibril axis through both AFM and TEM observation, and to have a step-wise decrease proceeding to the two sharp end. Particle size distributions on five target locations along individual CNC fibril axis were statistically reported and found to fit the lognormal distribution.

Towards nanocellulose application, a sponge-like nanocellulose-based carbon aerogel was synthesized and reported with highest normalized oil sorption capacity reached to 86 g/g for paraffin oil. The physical properties, internal morphology, thermal properties, and chemical properties of carbon aerogels heat-treated at 700 and 900 °C (Samples C-700 and C-900) were examined. The resulted carbon aerogel has high porosity (99%), ultra-low density (0.01 g/cm<sup>3</sup>), hydrophobic properties (149° static contact angle) and reusability. High BET surface area (521 m<sup>2</sup>/g) was observed in sample C-700, while it was only 149 m<sup>2</sup>/g for sample C-900. To further study the simultaneous effects of carbonization temperature and heating rate on oil absorption capacity, response surface methodology was adopted to determine the optimal values for processing carbon aerogel. With the concept of design of experiments (DOE), this approach quantifies the relationship between NFC aerogel carbonization processing conditions and carbon aerogel's physical properties. It was found that independent variables have significant linear and quadratic effect on dependent variables. The optimum operating conditions were referred as peak temperature= 250 °C and heating rate=9.9 °C/min considering low energy input and high efficiency. Compared to conventional single factor optimization methods, which are time consuming and expensive with vague and misleading information, Design of Experiment (DOE) method performed in this research and the resulted model provide integrated and accurate results to systematically and effectively predict the response through various independent variables.



The adsorption properties of carbon cellulose and carbon lignin were compared. Under identical thermal treatment, carbon cellulose is superior to carbon lignin. The atomic structure investigation through aberration-corrected STEM technique of carbon material from both precursors was performed. The one-layer graphene derived from carbon cellulose was observed and it was mainly composed of hexagonal lattice of carbons accompanied by nonhexagonal defects (five or seven atomic rings). Carbon derived from highly crystallized cellulose yields disordered porous structure; while kraft lignin derived carbon material has the tendency to yield well-ordered graphite structure. It was proved that carbon cellulose contains randomly orientated small pieces of fringe fragments and carbon lignin exhibit well-ordered stacking graphene sheets. Lattice structure of CNC without negative staining was observed. Beam irradiation effect on crystalline CNC caused the broken of hydrogen bonds, leading to the loss of crystallinity. Also noteworthy, is the fact that the resultant carbon structure is strongly affected by the precursor materials' structure.

## **FUTURE WORK**

The work performed in this dissertation covers nanocellulose synthesis, structure characterization, application as oil absorbent, and atomic scale investigation of cellulose nanoporous carbon. It targets to link the properties-structure relationships of biomass derived nanocellulose and carbonaceous material. However, based on current study, more research effort needs to be focused on the following areas:

- (1) Investigating the nanocrystal morphology, surface chemistry, and performing surface functionalization for reinforced nanocomposite application
- (2) Improving the carbon aerogel mechanical properties to achieve desirable application
- (3) Increasing specific surface area and making micro/mesopores for gas filters application

## REFERENCE

- AINA, V., ALBERTO, G., DEIANA, C., SAKHNO, Y., DAMIN, A. & MARTRA, G. 2013. Surface sites of nanomaterials: investigation of local structures by In situ IR spectroscopy. *In: FESENKO, O., YATSENKO, L. & BRODIN, M. (eds.) Nanomaterials Imaging Techniques, Surface Studies, and Applications*. Berlin: Springer-Verlag Berlin.
- ALLEN, M. J., HUD, N. V., BALOOCH, M., TENCH, R. J., SIEKHAUS, W. J. & BALHORN, R. 1992. Tip-radius-induced artifacts in AFM images of protamine-complexed DNA fibers. *Ultramicroscopy*, 42, 1095-1100.
- ANSELL, M. 2012. Wood: A 45th anniversary review of JMS papers. *Journal of Materials Science*, 47, 583-598.
- BAKER, A. A., HELBERT, W., SUGIYAMA, J. & MILES, M. J. 1997. High-resolution atomic force microscopy of native Valonia cellulose I microcrystals. *Journal of Structural Biology*, 119, 129-138.
- BALL, F. J. 1992. Chemistry of Lignin and Its Applications, Technical Literature. *Westvaco Chemical Division: Charleston Heights, SC*.
- BASTANI, D., SAFEKORDI, A. A., ALIHOSSEINI, A. & TAGHIKHANI, V. 2006. Study of oil sorption by expanded perlite at 298.15 K. *Separation and Purification Technology*, 52, 295-300.
- BONDESON, D., KVIEN, I. & OKSMAN, K. 2006. Strategies for preparation of cellulose whiskers from microcrystalline cellulose as reinforcement in nanocomposites. *Cellulose Nanocomposites: Processing, Characterization, and Properties*, 938, 10-25.
- BRITO, B. S. L., PEREIRA, F. V., PUTAUX, J. L. & JEAN, B. 2012. Preparation, morphology and structure of cellulose nanocrystals from bamboo fibers. *Cellulose*, 19, 1527-1536.
- BRUNAUER, S., EMMETT, P. H. & TELLER, E. 1938. Adsorption of gases in multimolecular layers. *Journal of the American Chemical Society*, 60, 309-319.
- BRUNNER, P. & ROBERTS, P. 1980. The significance of heating rate on char yield and char properties in the pyrolysis of cellulose. *Carbon*, 18, 217-224.
- CAGNON, B., PY, X., GUILLOT, A., STOECKLI, F. & CHAMBAT, G. 2009. Contributions of hemicellulose, cellulose and lignin to the mass and the porous properties of chars and steam activated carbons from various lignocellulosic precursors. *Bioresource Technology*, 100, 292-298.
- CAO, J., XIAO, G., XU, X., SHEN, D. & JIN, B. 2013. Study on carbonization of lignin by TG-FTIR and high-temperature carbonization reactor. *Fuel Processing Technology*, 106, 41-47.
- CAO, X., HABIBI, Y. & LUCIA, L. A. 2009. One-pot polymerization, surface grafting, and processing of waterborne polyurethane-cellulose nanocrystal nanocomposites. *Journal of Materials Chemistry*, 19, 7137-7145.
- CERVIN, N. T., AULIN, C., LARSSON, P. T. & WAGBERG, L. 2012. Ultra porous nanocellulose aerogels as separation medium for mixtures of oil/water liquids. *Cellulose*, 19, 401-410.
- CHAWLA, N., HOLMES, J. W. & MANSFIELD, J. F. 1995. Surface roughness characterization of Nicalon™ and HI-Nicalon™ ceramic fibers by atomic force microscopy. *Materials Characterization*, 35, 199-206.

- CHEN, W., YU, H., LI, Q., LIU, Y. & LI, J. 2011. Ultralight and highly flexible aerogels with long cellulose I nanofibers. *Soft Matter*, 7, 10360-10368.
- CHENG, Q., WANG, S., RIALS, T. & LEE, S. 2007. Physical and mechanical properties of polyvinyl alcohol and polypropylene composite materials reinforced with fibril aggregates isolated from regenerated cellulose fibers. *Cellulose*, 14, 593-602.
- CHERIAN, B. M., POTHAN, L. A., NGUYEN-CHUNG, T., MENNIG, G., KOTTAISAMY, M. & THOMAS, S. 2008. A novel method for the synthesis of cellulose nanofibril whiskers from banana fibers and characterization. *Journal of Agricultural and Food Chemistry*, 56, 5617-5627.
- CHOI, S.-J., KWON, T.-H., IM, H., MOON, D.-I., BAEK, D. J., SEOL, M.-L., DUARTE, J. P. & CHOI, Y.-K. 2011. A polydimethylsiloxane (PDMS) sponge for the selective absorption of oil from water. *Acs Applied Materials & Interfaces*, 3, 4552-4556.
- DAVIDSON, H. & LOSTY, H. 1963. The initial pyrolyses of cellulose. *GEC J*, 30, 22-28.
- DING, J., WANG, H., LI, Z., KOHANDEHGHAN, A., CUI, K., XU, Z., ZAHIRI, B., TAN, X., LOTFABAD, E. M., OLSEN, B. C. & MITLIN, D. 2013. Carbon nanosheet frameworks derived from peat moss as high performance sodium ion battery anodes. *Acs Nano*, 7, 11004-11015.
- DING, S. Y. & HIMMEL, M. E. 2006. The maize primary cell wall microfibril: A new model derived from direct visualization. *Journal of Agricultural and Food Chemistry*, 54, 597-606.
- DOBELE, G., DIZHBITE, T., GIL, M. V., VOLPERTS, A. & CENTENO, T. A. 2012. Production of nanoporous carbons from wood processing wastes and their use in supercapacitors and CO<sub>2</sub> capture. *Biomass & Bioenergy*, 46, 145-154.
- DONG, C., ZHANG, H., PANG, Z., LIU, Y. & ZHANG, F. 2013. Sulfonated modification of cotton linter and its application as adsorbent for high-efficiency removal of lead(II) in effluent. *Bioresource Technology*, 146, 512-518.
- DUMANLI, A. G. & WINDLE, A. H. 2012. Carbon fibres from cellulosic precursors: a review. *Journal of Materials Science*, 47, 4236-4250.
- EICHHORN, S. J., DUFRESNE, A., ARANGUREN, M., MARCOVICH, N. E., CAPADONA, J. R., ROWAN, S. J., WEDER, C., THIELEMANS, W., ROMAN, M., RENNECKAR, S., GINDL, W., VEIGEL, S., KECKES, J., YANO, H., ABE, K., NOGI, M., NAKAGAITO, A. N., MANGALAM, A., SIMONSEN, J., BENIGHT, A. S., BISMARCK, A., BERGLUND, L. A. & PEIJS, T. 2010. Review: current international research into cellulose nanofibres and nanocomposites. *Journal of Materials Science*, 45, 1-33.
- ELAZZOUI-HAFRAOUI, S., NISHIYAMA, Y., PUTAUX, J. L., HEUX, L., DUBREUIL, F. & ROCHAS, C. 2008. The shape and size distribution of crystalline nanoparticles prepared by acid hydrolysis of native cellulose. *Biomacromolecules*, 9, 57-65.
- EPSTEIN, B. 1947. The mathematical description of certain breakage mechanisms leading to the logarithmico-normal distribution. *Journal of the Franklin Institute*, 244, 471-477.
- FAVIER, V., DENDIEVEL, R., CANOVA, G., CAVAILLE, J. Y. & GILORMINI, P. 1997. Simulation and modeling of three-dimensional percolating structures: Case of a latex matrix reinforced by a network of cellulose fibers. *Acta Materialia*, 45, 1557-1565.
- FERNANDES, A. N., THOMAS, L. H., ALTANER, C. M., CALLOW, P., FORSYTH, V. T., APPERLEY, D. C., KENNEDY, C. J. & JARVIS, M. C. 2011. Nanostructure of

- cellulose microfibrils in spruce wood. *Proceedings of the National Academy of Sciences of the United States of America*, 108, E1195-E1203.
- FLAUZINO NETO, W. P., SILVÉRIO, H. A., DANTAS, N. O. & PASQUINI, D. 2013. Extraction and characterization of cellulose nanocrystals from agro-industrial residue – Soy hulls. *Industrial Crops and Products*, 42, 480-488.
- FUJIMOTO, H. 2003. Theoretical X-ray scattering intensity of carbons with turbostratic stacking and AB stacking structures. *Carbon*, 41, 1585-1592.
- GASPAR, D., FERNANDES, S. N., DE OLIVEIRA, A. G., FERNANDES, J. G., GREY, P., PONTES, R. V., PEREIRA, L., MARTINS, R., GODINHO, M. H. & FORTUNATO, E. 2014. Nanocrystalline cellulose applied simultaneously as the gate dielectric and the substrate in flexible field effect transistors. *Nanotechnology*, 25 (094008).
- GOODELL, B., XIE, X. F., QIAN, Y. H., DANIEL, G., PETERSON, M. & JELLISON, J. 2008. Carbon nanotubes produced from natural cellulosic materials. *Journal of Nanoscience and Nanotechnology*, 8, 2472-2474.
- GU, J., CATCHMARK, J. M., KAISER, E. Q. & ARCHIBALD, D. D. 2013. Quantification of cellulose nanowhiskers sulfate esterification levels. *Carbohydrate Polymers*, 92, 1809-1816.
- GUI, X., LI, H., WANG, K., WEI, J., JIA, Y., LI, Z., FAN, L., CAO, A., ZHU, H. & WU, D. 2011. Recyclable carbon nanotube sponges for oil absorption. *Acta Materialia*, 59, 4798-4804.
- GUO, J. & CATCHMARK, J. M. 2012. Surface area and porosity of acid hydrolyzed cellulose nanowhiskers and cellulose produced by *Gluconacetobacter xylinus*. *Carbohydrate Polymers*, 87, 1026-1037.
- GUO, J., MORRIS, J. R., IHM, Y., CONTESCU, C. I., GALLEGO, N. C., DUSCHER, G., PENNYCOOK, S. J. & CHISHOLM, M. F. 2012. Topological defects: origin of nanopores and enhanced adsorption performance in nanoporous carbon. *Small*, 8, 3283-3288.
- HABIBI, Y., LUCIA, L. A. & ROJAS, O. J. 2010. Cellulose nanocrystals: chemistry, self-assembly, and applications. *Chemical Reviews*, 110, 3479-3500.
- HAJJI, P., CAVAILLE, J. Y., FAVIER, V., GAUTHIER, C. & VIGIER, G. 1996. Tensile behavior of nanocomposites from latex and cellulose whiskers. *Polymer Composites*, 17, 612-619.
- HAN, J. P., ZHU, Y., HU, J. L., LUO, H. S., YEUNG, L. Y., LI, W. G., MENG, Q. H., YE, G. D., ZHANG, S. & FAN, Y. 2012. Morphology, Reversible Phase Crystallization, and Thermal Sensitive Shape Memory Effect of Cellulose Whisker/SMPU Nano-Composites. *Journal of Applied Polymer Science*, 123, 749-762.
- HARKINS, W. D. & BROWN, F. E. 1919. The determination of surface tension (free surface energy), and the weight of falling drops - The surface tension of water and benzene by the capillary height method. *Journal of the American Chemical Society*, 41, 499-524.
- HASSANABADI, H. M. & RODRIGUE, D. 2014. Effect of particle size and shape on the reinforcing efficiency of nanoparticles in polymer nanocomposites. *Macromolecular Materials and Engineering*, 299, 1220-1231.
- HATA, T., IMAMURA, Y., KOBAYASHI, E., YAMANE, K. & KIKUCHI, K. 2000. Onion-like graphitic particles observed in wood charcoal. *Journal of Wood Science*, 46, 89-92.

- HE, L., MELNICHENKO, Y., GALLEGRO, N., CONTESCU, C., GUO, J. & BAHADUR, J. 2014a. Investigation of morphology and hydrogen adsorption capacity of disordered carbons. *Carbon*, 80, 82-90.
- HE, L., MELNICHENKO, Y. B., GALLEGRO, N. C., CONTESCU, C. I., GUO, J. & BAHADUR, J. 2014b. Investigation of morphology and hydrogen adsorption capacity of disordered carbons. *Carbon*, 80, 82-90.
- HERRERA, M. A., MATHEW, A. P. & OKSMAN, K. 2012. Comparison of cellulose nanowhiskers extracted from industrial bio-residue and commercial microcrystalline cellulose. *Materials Letters*, 71, 28-31.
- HOEPFNER, S., RATKE, L. & MILOW, B. 2008. Synthesis and characterisation of nanofibrillar cellulose aerogels. *Cellulose*, 15, 121-129.
- HU, H., ZHAO, Z., WAN, W., GOGOTSI, Y. & QIU, J. 2013. Ultralight and highly compressible graphene aerogels. *Advanced Materials*, 25, 2219-2223.
- HUANG, X. 2009. Fabrication and properties of carbon fibers. *Materials*, 2, 2369-2403.
- HUBBE, M. A., AYOUB, A., DAYSTAR, J. S., VENDITTI, R. A. & PAWLAK, J. J. 2013. Enhanced absorbent products incorporating cellulose and its derivatives: A review. *BioResources*, 8, 6556-6629.
- ISHIMARU, K., HATA, T., BRONSVELD, P., MEIER, D. & IMAMURA, Y. 2007. Spectroscopic analysis of carbonization behavior of wood, cellulose and lignin. *Journal of Materials Science*, 42, 122-129.
- ISHIMARU, K., VYSTAVEL, T., BRONSVELD, P., HATA, T., IMAMURA, Y. & HOSSON, J. 2001. Diamond and pore structure observed in wood charcoal. *Journal of Wood Science*, 47, 414-416.
- JIN, H., KETTUNEN, M., LAIHO, A., PYNNONEN, H., PALTAKARI, J., MARMUR, A., IKKALA, O. & RAS, R. H. A. 2011. Superhydrophobic and superoleophobic nanocellulose aerogel membranes as bioinspired cargo carriers on water and oil. *Langmuir*, 27, 1930-1934.
- JOHNSON, D. J., TOMIZUKA, I. & WATANABE, O. 1975. The fine structure of lignin-based carbon fibres. *Carbon*, 13, 321-325.
- JONOBI, M., AITOMÄKI, Y., MATHEW, A. P. & OKSMAN, K. 2014. Thermoplastic polymer impregnation of cellulose nanofibre networks: Morphology, mechanical and optical properties. *Composites Part A: Applied Science and Manufacturing*, 58, 30-35.
- KARGARZADEH, H., AHMAD, I., ABDULLAH, I., DUFRESNE, A., ZAINUDIN, S. Y. & SHELAMI, R. M. 2012. Effects of hydrolysis conditions on the morphology, crystallinity, and thermal stability of cellulose nanocrystals extracted from kenaf bast fibers. *Cellulose*, 19, 855-866.
- KELSEY, R. G. & SHAFIZADEH, F. 1980. Enhancement of cellulose accessibility and enzymatic-hydrolysis by simultaneous wet milling. *Biotechnology and Bioengineering*, 22, 1025-1036.
- KHOSHKAVA, V. & KAMAL, M. R. 2014. Effect of cellulose nanocrystals (CNC) particle morphology on dispersion and rheological and mechanical properties of polypropylene/CNC Nanocomposites. *Acs Applied Materials & Interfaces*, 6, 8146-8157.
- KIPLING, J. J., SHERWOOD, J. N., SHOOTER, P. V. & THOMPSON, N. R. 1964. The pore structure and surface area of high-temperature polymer carbons. *Carbon*, 1, 321-328.

- KNAUERT, S. T., DOUGLAS, J. F. & STARR, F. W. 2007. The effect of nanoparticle shape on polymer-nanocomposite rheology and tensile strength. *Journal of Polymer Science Part B: Polymer Physics*, 45, 1882-1897.
- KORHONEN, J. T., KETTUNEN, M., RAS, R. H. A. & IKKALA, O. 2011. Hydrophobic nanocellulose aerogels as floating, sustainable, reusable, and recyclable oil absorbents. *Acs Applied Materials & Interfaces*, 3, 1813-1816.
- KVIEN, I., TANEM, B. S. & OKSMAN, K. 2005. Characterization of cellulose whiskers and their nanocomposites by atomic force and electron microscopy. *Biomacromolecules*, 6, 3160-3165.
- LANGAN, P., PETRIDIS, L., O'NEILL, H. M., PINGALI, S. V., FOSTON, M., NISHIYAMA, Y., SCHULZ, R., LINDNER, B., HANSON, B. L., HARTON, S., HELLER, W. T., URBAN, V., EVANS, B. R., GNANAKARAN, S., RAGAUSKAS, A. J., SMITH, J. C. & DAVISON, B. H. 2014. Common processes drive the thermochemical pretreatment of lignocellulosic biomass. *Green Chemistry*, 16, 63-68.
- LI, H., GUI, X., ZHANG, L., WANG, S., JI, C., WEI, J., WANG, K., ZHU, H., WU, D. & CAO, A. 2010. Carbon nanotube sponge filters for trapping nanoparticles and dye molecules from water. *Chemical Communications*, 46, 7966-7968.
- LI, J., LU, Y., YANG, D., SUN, Q., LIU, Y. & ZHAO, H. 2011. Lignocellulose aerogel from wood-ionic liquid solution (1-allyl-3-methylimidazolium chloride) under freezing and thawing conditions. *Biomacromolecules*, 12, 1860-1867.
- LI, W., YANG, K., PENG, J., ZHANG, L., GUO, S. & XIA, H. 2008. Effects of carbonization temperatures on characteristics of porosity in coconut shell chars and activated carbons derived from carbonized coconut shell chars. *Industrial Crops and Products*, 28, 190-198.
- LI, Y., KRÖGER, M. & LIU, W. K. 2012. Nanoparticle geometrical effect on structure, dynamics and anisotropic viscosity of polyethylene nanocomposites. *Macromolecules*, 45, 2099-2112.
- LI, Y., SAMAD, Y. A., POLYCHRONOPOULOU, K., ALHASSAN, S. M. & LIAO, K. 2014. Carbon aerogel from winter melon for highly efficient and recyclable oils and organic solvents absorption. *ACS Sustainable Chemistry & Engineering*, 2, 1492-1497.
- LIN, N. & DUFRESNE, A. 2014. Surface chemistry, morphological analysis and properties of cellulose nanocrystals with gradiented sulfation degrees. *Nanoscale*, 6, 5384-5393.
- LIU, D., CHEN, X., YUE, Y., CHEN, M. & WU, Q. 2011. Structure and rheology of nanocrystalline cellulose. *Carbohydrate Polymers*, 84, 316-322.
- LIU, H. & BRINSON, L. C. 2008. Reinforcing efficiency of nanoparticles: A simple comparison for polymer nanocomposites. *Composites Science and Technology*, 68, 1502-1512.
- LIU, Y., MA, J., WU, T., WANG, X., HUANG, G., LIU, Y., QIU, H., LI, Y., WANG, W. & GAO, J. 2013. Cost-effective reduced graphene oxide-coated polyurethane sponge as a highly efficient and reusable oil-absorbent. *Acs Applied Materials & Interfaces*, 5, 10018-10026.
- LU, P. & HSIEH, Y. L. 2012. Preparation and characterization of cellulose nanocrystals from rice straw. *Carbohydrate Polymers*, 87, 564-573.
- LU, Q., TANG, L., WANG, S., HUANG, B., CHEN, Y. & CHEN, X. 2014. An investigation on the characteristics of cellulose nanocrystals from Pennisetum sinense. *Biomass & Bioenergy*, 70, 267-272.



- MAJOINEN, J., HAATAJA, J. S., APPELHANS, D., LEDERER, A., OLSZEWSKA, A., SEITSONEN, J., ASEYEV, V., KONTTURI, E., ROSILO, H., ÖSTERBERG, M., HOUBENOV, N. & IKKALA, O. 2013. Supracolloidal multivalent interactions and wrapping of dendronized glycopolymers on native cellulose nanocrystals. *Journal of the American Chemical Society*, 136, 866-869.
- MARIANO, M., EL KISSI, N. & DUFRESNE, A. 2014. Cellulose nanocrystals and related nanocomposites: review of some properties and challenges. *Journal of Polymer Science Part B-Polymer Physics*, 52, 791-806.
- MATTHEWS, J. F., SKOPEC, C. E., MASON, P. E., ZUCCATO, P., TORGET, R. W., SUGIYAMA, J., HIMMEL, M. E. & BRADY, J. W. 2006. Computer simulation studies of microcrystalline cellulose I $\beta$ . *Carbohydrate Research*, 341, 138-152.
- MENG, Y., YOUNG, T., LIU, P., CONTESCU, C., HUANG, B. & WANG, S. 2014. Ultralight carbon aerogel from nanocellulose as a highly selective oil absorption material. *Cellulose*, 1-13.
- MILOSAVLJEVIC, I. & SUUBERG, E. M. 1995. Cellulose thermal decomposition kinetics: global mass loss kinetics. *Industrial & Engineering Chemistry Research*, 34, 1081-1091.
- MISHNAEVSKY JR, L. 2012. Micromechanical analysis of nanocomposites using 3D voxel based material model. *Composites Science and Technology*, 72, 1167-1177.
- MOIGNE, N. L., OEVER, M. V. D. & BUDTOVA, T. 2011. A statistical analysis of fibre size and shape distribution after compounding in composites reinforced by natural fibres. *Composites Part A: Applied Science and Manufacturing*, 42, 1542-1550.
- MONTGOMERY, D. C. 2012. *Design and Analysis of Experiments, 8th Edition*, John Wiley & Sons, Incorporated.
- MOON, R., MARTINI, A., NAIRN, J., SIMONSEN, J. & YOUNGBLOOD, J. 2011. Cellulose nanomaterials review: structure, properties and nanocomposites. *Chemical Society Reviews*, 40, 3941-3994.
- MURAMATSU, H., KIM, Y. A., YANG, K.-S., CRUZ-SILVA, R., TODA, I., YAMADA, T., TERRONES, M., ENDO, M., HAYASHI, T. & SAITOH, H. 2014. Rice husk-derived graphene with nano-sized domains and clean edges. *Small*, 10, 2766-2770.
- NAGEL, B., PUSZ, S. & TRZEBICKA, B. 2014. Review: tailoring the properties of macroporous carbon foams. *Journal of Materials Science*, 49, 1-17.
- NISHIYAMA, Y., LANGAN, P. & CHANZY, H. 2002. Crystal structure and hydrogen-bonding system in cellulose I $\beta$  from synchrotron X-ray and neutron fiber diffraction. *Journal of the American Chemical Society*, 124, 9074-9082.
- PENG, D., LAN, Z., GUO, C., YANG, C. & DANG, Z. 2013. Application of cellulase for the modification of corn stalk: Leading to oil sorption. *Bioresource Technology*, 137, 414-418.
- PENG, Y., HAN, Y. & GARDNER, D. J. 2012. Spray-drying cellulose nanofibrils: effect of drying process parameters on particle morphology and size distribution. *Wood and Fiber Science*, 44, 448-461.
- RAFIEIAN, F. & SIMONSEN, J. 2014. Fabrication and characterization of carboxylated cellulose nanocrystals reinforced glutenin nanocomposite. *Cellulose*, 21, 4167-4180.
- RAGAUSKAS, A. J., WILLIAMS, C. K., DAVISON, B. H., BRITOVSEK, G., CAIRNEY, J., ECKERT, C. A., FREDERICK, W. J., HALLETT, J. P., LEAK, D. J., LIOTTA, C. L.,

- MIELLENZ, J. R., MURPHY, R., TEMPLER, R. & TSCHAPLINSKI, T. 2006. The path forward for biofuels and biomaterials. *Science*, 311, 484-489.
- ROSA, M. F., MEDEIROS, E. S., MALMONGE, J. A., GREGORSKI, K. S., WOOD, D. F., MATTOSO, L. H. C., GLENN, G., ORTS, W. J. & IMAM, S. H. 2010. Cellulose nanowhiskers from coconut husk fibers: Effect of preparation conditions on their thermal and morphological behavior. *Carbohydrate Polymers*, 81, 83-92.
- RYU, Z., ZHENG, J., WANG, M. & ZHANG, B. 1999. Characterization of pore size distributions on carbonaceous adsorbents by DFT. *Carbon*, 37, 1257-1264.
- SANTOS, R. M. D., FLAUZINO NETO, W. P., SILVÉRIO, H. A., MARTINS, D. F., DANTAS, N. O. & PASQUINI, D. 2013. Cellulose nanocrystals from pineapple leaf, a new approach for the reuse of this agro-waste. *Industrial Crops and Products*, 50, 707-714.
- SEGAL, L., CREELY, J. J., MARTIN, A. E. & CONRAD, C. M. 1959. An empirical method for estimating the degree of crystallinity of native cellulose using the X-Ray diffractometer *Textile Research Journal*, 29, 786-794.
- SHEN, D., XIAO, R., ZHANG, H. & GU, S. 2013. *The overview of thermal decomposition of cellulose in lignocellulosic biomass*.
- SILVA, F., RODRIGUES, M. & MAUGERI, F. 1999. Dynamic modelling, simulation and optimization of an extractive continuous alcoholic fermentation process. *J. Chem. Technol. Biotechnol.*, 74, 176-182.
- SING, K. S. W., EVERETT, D. H., HAUL, R. A. W., MOSCOU, L., PIEROTTI, R. A., ROUQUEROL, J. & SIEMIENIEWSKA, T. 1985. Reporting physisorption data for gas solid systems with special reference to the determination of surface-area and porosity (recommendations 1984). *Pure and Applied Chemistry*, 57, 603-619.
- SIQUEIRA, G., BRAS, J. & DUFRESNE, A. 2009. Cellulose whiskers versus microfibrils: Influence of the nature of the nanoparticle and its surface functionalization on the thermal and mechanical properties of nanocomposites. *Biomacromolecules*, 10, 425-432.
- SIQUEIRA, G., BRAS, J. & DUFRESNE, A. 2010. Cellulosic Bionanocomposites: A Review of Preparation, Properties and Applications. *Polymers*, 2, 728-765.
- SLADDEN, S. E., BRANSBY, D. I. & AIKEN, G. E. 1991. Biomass yield, composition and production costs for eight switchgrass varieties in Alabama. *Biomass & Bioenergy*, 1, 119-122.
- SUGIYAMA, J., VUONG, R. & CHANZY, H. 1991. Electron diffraction study on the two crystalline phases occurring in native cellulose from an algal cell wall. *Macromolecules*, 24, 4168-4175.
- TANDON, G. P. & WENG, G. J. 1984. The effect of aspect ratio of inclusions on the elastic properties of unidirectionally aligned composites. *Polymer Composites*, 5, 327-333.
- TANG, M. & BACON, R. 1964a. Carbonization of cellulose fibers .1. low temperature pyrolysis. *Carbon*, 1, 390-390.
- TANG, M. M. & BACON, R. 1964b. Carbonization of cellulose fibers -1. low temperature pyrolysis. *Carbon*, 2, 211-214.
- TEIXEIRA, E. D., CORREA, A. C., MANZOLI, A., LEITE, F. L., DE OLIVEIRA, C. R. & MATTOSO, L. H. C. 2010. Cellulose nanofibers from white and naturally colored cotton fibers. *Cellulose*, 17, 595-606.
- TEN, E., BAHR, D. F., LI, B., JIANG, L. & WOLCOTT, M. P. 2012. Effects of cellulose nanowhiskers on mechanical, dielectric, and rheological properties of poly(3-

- hydroxybutyrate-co-3-hydroxyvalerate)/cellulose nanowhisker composites. *Industrial & Engineering Chemistry Research*, 51, 2941-2951.
- TENHAEFF, W. E., RIOS, O., MORE, K. & MCGUIRE, M. A. 2014. Highly Robust Lithium Ion Battery Anodes from Lignin: An Abundant, Renewable, and Low-Cost Material. *Advanced Functional Materials*, 24, 86-94.
- THIELEMANS, W., CAN, E., MORYE, S. S. & WOOL, R. P. 2002. Novel applications of lignin in composite materials. *Journal of Applied Polymer Science*, 83, 323-331.
- THYGESEN, A., ODDERSHEDE, J., LILHOLT, H., THOMSEN, A. B. & STAHL, K. 2005. On the determination of crystallinity and cellulose content in plant fibres. *Cellulose*, 12, 563-576.
- UDDIN, A. J., ARAKI, J. & GOTOH, Y. 2011. Characterization of the poly(vinyl alcohol)/cellulose whisker gel spun fibers. *Composites Part A: Applied Science and Manufacturing*, 42, 741-747.
- UPADHYAYULA, V. K. K., DENG, S., MITCHELL, M. C. & SMITH, G. B. 2009. Application of carbon nanotube technology for removal of contaminants in drinking water: A review. *Science of the Total Environment*, 408, 1-13.
- VAN DEN OEVER, M. J. A., ELBERSEN, H. W., KEIJERS, E. R. P., GOSSELINK, R. J. A. & DE KLERK-ENGELS, B. 2003. Switchgrass (*Panicum virgatum*L.) as a reinforcing fibre in polypropylene composites. *Journal of Materials Science*, 38, 3697-3707.
- VISAKH, P. M., THOMAS, S., OKSMAN, K. & MATHEW, A. P. 2012. Crosslinked natural rubber nanocomposites reinforced with cellulose whiskers isolated from bamboo waste: Processing and mechanical/thermal properties. *Composites Part A: Applied Science and Manufacturing*, 43, 735-741.
- WANG, H., XU, Z., KOHANDEHGHAN, A., LI, Z., CUI, K., TAN, X., STEPHENSON, T., KING'ONDU, C., HOLT, C., OLSEN, B., TAK, J., HARFIELD, D., ANYIA, A. & MITLIN, D. 2013. Interconnected Carbon Nanosheets Derived from Hemp for Ultrafast Supercapacitors with High Energy. *ACS Nano*, 7, 5131-5141.
- WANG, H., ZHOU, H., PENG, R. & MISHNAEVSKY JR, L. 2011. Nanoreinforced polymer composites: 3D FEM modeling with effective interface concept. *Composites Science and Technology*, 71, 980-988.
- WANG, S. & CHENG, Q. 2009. A novel process to isolate fibrils from cellulose fibers by high-intensity ultrasonication, part 1: process optimization. *Journal of Applied Polymer Science*, 113, 1270-1275.
- WISELOGEL, A. E., AGBLEVOR, F. A., JOHNSON, D. K., DEUTCH, S., FENNELL, J. A. & SANDERSON, M. A. 1996. Compositional changes during storage of large round switchgrass bales. *Bioresource Technology*, 56, 103-109.
- WU, Q., MENG, Y., CONCHA, K., WANG, S., LI, Y., MA, L. & FU, S. 2013a. Influence of temperature and humidity on nano-mechanical properties of cellulose nanocrystal films made from switchgrass and cotton. *Industrial Crops and Products*, 48, 28-35.
- WU, Q., MENG, Y., WANG, S., LI, Y., FU, S., MA, L. & HARPER, D. 2014. Rheological behavior of cellulose nanocrystal suspension: Influence of concentration and aspect ratio. *Journal of Applied Polymer Science*, 131, 40525-40533.
- WU, Q., MENG, Y. J., CONCHA, K., WANG, S. Q., LI, Y. J., MA, L. F. & FU, S. Y. 2013b. Influence of temperature and humidity on nano-mechanical properties of cellulose

- nanocrystal films made from switchgrass and cotton. *Industrial Crops and Products*, 48, 28-35.
- WU, Q., PAN, N., DENG, K. & PAN, D. 2008. Thermogravimetry-mass spectrometry on the pyrolysis process of Lyocell fibers with and without catalyst. *Carbohydrate Polymers*, 72, 222-228.
- WU, Z., LI, C., LIANG, H., CHEN, J. & YU, S. 2013c. Ultralight, flexible, and fire-resistant carbon nanofiber aerogels from bacterial cellulose. *Angewandte Chemie-International Edition*, 52, 2925-2929.
- XIE, X., GOODELL, B., ZHANG, D., NAGLE, D. C., QIAN, Y., PETERSON, M. L. & JELLISON, J. 2009. Characterization of carbons derived from cellulose and lignin and their oxidative behavior. *Bioresource Technology*, 100, 1797-1802.
- XU, X., LIU, F., JIANG, L., ZHU, J. Y., HAAGENSON, D. & WIESENORN, D. P. 2013. Cellulose nanocrystals vs. cellulose nanofibrils: a comparative study on their microstructures and effects as polymer reinforcing agents. *ACS Applied Materials & Interfaces*, 5, 2999-3009.
- YANG, H., YAN, R., CHEN, H., LEE, D. H. & ZHENG, C. 2007. Characteristics of hemicellulose, cellulose and lignin pyrolysis. *Fuel*, 86, 1781-1788.
- ZENG, Y. 2011. *A study of missing data imputation and predictive modeling of strength properties of wood composites*. Master Thesis, University of Tennessee.
- ZHANG, A., CHEN, M., DU, C., GUO, H., BAI, H. & LI, L. 2013. Poly(dimethylsiloxane) oil absorbent with a three-dimensionally interconnected porous structure and swellable skeleton. *Acs Applied Materials & Interfaces*, 5, 10201-10206.
- ZHANG, W., ZHANG, Y., LU, C. & DENG, Y. 2012. Aerogels from crosslinked cellulose nano/micro-fibrils and their fast shape recovery property in water. *Journal of Materials Chemistry*, 22, 11642-11650.
- ZHAO, P., WANG, L., SUN, C., JIANG, T., ZHANG, J., ZHANG, Q., SUN, J., DENG, Y. & WANG, S. 2012. Uniform mesoporous carbon as a carrier for poorly water soluble drug and its cytotoxicity study. *European Journal of Pharmaceutics and Biopharmaceutics*, 80, 535-543.

## VITA

Yujie Meng was born in Yuncheng, Shanxi province, China. After graduation from Taiyuan Yuying High School, Taiyuan, China in 2003, she enrolled in the College of Materials Sciences and Technology at Nanjing Forestry University, Nanjing, Jiangsu, China, where she obtained her Bachelor's degree in packaging engineering in 2007. She moved to United States and joined Center for Renewable Carbon at University of Tennessee in 2008 to pursue her Master's degree in Forestry and completed it in 2010. She continued to pursue a PhD degree in Natural Resources with a concentration in Bio-based Products and Wood Science & Technology and a dual Master's degree in Statistics under the co-advisement of Dr. Siqun Wang and Dr. Timothy M. Young at University of Tennessee. She received her Ph.D. and the Statistic Master degree in 2015.